Université catholique de Louvain
École Polytechnique de Louvain
ICTEAM Electrical Engineering

Multi-Link Channel Modeling and Interference Characterization for Beyond 4G Networks

par

Nizabat KHAN

THÈSE PRÉSENTÉE EN VUE DE L'OBTENSION DU GRADE DE DOCTEUR EN SCIENCES DE L'INGÉNIEUR

Composition du Jury

1. Prof. Claude Oestges (Supervisor)	UCL, Belgium
2. Prof. Luc Vandendorpe (President)	UCL, Belgium
3. Prof. Jérôme Louveaux (Secretary)	UCL, Belgium
4. Prof. Philippe De Doncker	ULB, Belgium
5. Prof. Alister Burr	UoY, United Kingdom

June 2014

To my parents,
to my wife,
and to my daughter

Acknowledgements

In the Name of ALLAH, the Most Gracious, the Most Merciful

All praise and thanks are due to ALLAH, the almighty, for giving me the health and strength to complete this work.

It has been a long journey but the company and generous support of some amazing people have made this journey exciting, to whom I owe my gratitude. In the following, I will attempt to thank for their kindness.

First and foremost, I would like to express my heartfelt gratitude to my supervisor, Prof. Claude Oestges, for providing me the opportunity to pursue my PhD studies under his supervision. My sincere thanks for his guidance, useful advice, constant encouragement, and always having the time for discussions. His profound knowledge in the vast field of wireless communication in particular channel modeling has been very helpful to complete this work. It has been a pleasure to work with him in a motivating environment through all these years. I would also like to thank him for his efforts to find financial support that made this thesis possible.

I would like to sincerely thank the thesis jury, Prof. Luc Vandendorpe, Prof. Alister Burr, Prof. Philippe De Doncker, and Prof. Jérôme Louveaux for accepting to be member of this jury. I also thank them for their time, valuable advices, comments and corrections that they proposed during my private defense. Their precious remarks and advices were greatly useful to improve the quality of this thesis. I would also like to thank all of my co-authors for their fruitful collaborations.

I am grateful to all of my research and measurements colleagues Francesco Mani, Lingfeng Liu, Olivier Renaudin and Evgenii Vinogradov for their help during the measurement campaigns and interesting discussions. The time consuming and complex task of measurement campaigns involving logistics would not be possible without their help and collaboration. A long list of my colleagues at ICTEAM deserves my gratitude for the interesting discussions: Khaled, Khairuddin, Mouloud, Mostafa, Azeem, Ashraf, Shambhu, Carlos, Tadilo, Hammad, Nicolas, Prasad, Alberto, and Babak. Thanks to all the people I have worked with in the ELEN department.

Many thanks go to the technical and administrative staff at the ICTEAM institute, especially Brigitte Dupont and Francois Hubin for helping me out with computer matters, Pascal Simon for his logistical assistance, David Spôte for his excellent mechanical solutions, Isabelle Dargent and Marie-Christine for their administrative help and prompt responses.

I would like to express my gratitude to all my friends and their families in Belgium, whose presence made my stay in Belgium more fun. List is way too long, but particular thanks to Azeem, Hafeez, Zohaib, Ramzan, Salman, Asim, Shahid, Shahab, Sughis, Noman, Amir, Aftab, Rashid, Naeem, Zubair, Obaid, Khurram and Nayyab for their kindness and support. I would also like to thank all my friends for their help and support, in particular "the dinning philosophers": Naveed, Nadeem, Taimoor, Ali, Raza, Adeel, Farrukh, Tahir, and respected seniors Shurjeel and Farhan bhai. Special thanks are also due to Marja, Rameez, Usman, Ejaz, Adnan, and Shahid. Thank you all.

Finally, none of this would have been possible with out the love, countless prayers, continuous encouragement, and unwavering support of my parents. I will be eternally grateful, for everything you have done for me since my childhood. Special thanks to my sisters (Bilqees, Asima, Humera) for their love and care. I would also like to thank my mother and father in law for their prayers and advices. I would not have finished this thesis without support, encouragement and help of my wife, Sana. Thank you for always being there, for your unconditional love, care, support, and for being the mother of our beloved daughter Izzah, the joy of our life.

Nizabat Khan

Contents

List of Figures

List of Tables

List of Acronyms

1G	First Generation
2G	Second Generation
3G	Third Generation
4G	Fourth Generation
3GPP	Third Generation Partnership Project
AoA	Azimuth-of-Arrival
AoD	Azimuth-of-Departure
AWGN	Additive White Gaussian Noise
BER	Bit Error Rate
BS	Base Station
CBSM	Correlation-Based Stochastic Model
CCI	Co-Channel Interference
CDF	Cumulative Distribution Function
CDMA	Code Division Multiple Access
CIR	Channel Impulse Response
CKA	Clock Keep Alive
CMC	Channel Matrix Colinearity
CMD	Correlation Matrix Distance
CoMP	Coordinated Multi-Point
CPR	Co-Polar Ratio
CSI	Channel State Information
EDGE	Enhanced Data-rates for Global Evolution
GO	Geometrical Optics

GoS	Grade of Service
GPRS	General Packet Radio Services
GPS	Global Positioning System
GRF	Gain Reduction Factor
GSCM	Geometry-based Stochastic Channel Model
GSM	Global Systems for Mobile Communication
HSPA	High-Speed Packet Access
ICI	Inter-Cell Interference
IR	Impulse Response
LOS	Line Of Sight
LTE	Long Term Evolution
MIMO	Multiple-Input Multiple-Output
MPC	MultiPath Component
MS	Mobile Station
MU	Multi-User
NLOS	Non Line Of Sight
OFDM	Orthogonal Frequency-Division Multiplexing
OLOS	Obstructed Line Of Sight
PDF	Probability Density Function
PFD	Power Flux Density
PN	Pseudo-Noise
RF	Radio Frequency
RMS	Root Mean Square
RS	Relay Station

RT	Ray-Tracing
RTCS	Real Time Control Software
Rx	Receiver
SCM	Spatial Channel Model
SF	Shadow Fading
SFC	Shadow Fading Correlation
SINR	Signal to Interference and Noise Ratio
SIR	Signal to Interference Ratio
SISO	Single-Input Single-Output
SU	Single-User
SUI	Stanford University Interim
TDD	Time Division Duplex
TDL	Tapped Delay Line
Tx	Transmitter
UMTS	Universal Mobile Telecommunication System
VR	Visibility Regions
WCDMA	Wideband Code Division Multiple Access
WiMAX	Worldwide Interoperability for Microwave Access
WSD	Wideband Spectral Divergence
WSSUS	Wide-Sense Stationary Uncorrelated Scattering
XPD	Cross Polarization Discrimination

List of Symbols

λ	Wavelength
δ	Dirac function
β	Beamwidth
ρ	Correlation
ρ_S	Shadow fading correlation
μ	Mean
θ	Azimuth
ϕ	Elevation
σ	Standard deviation
τ	Delay
ϵ_r	Relative permittivity
κ	Electric conductivity
ν	Doppler frequency
ζ	Wideband spectral divergence
χ	Condition number ratio
Ω	Correlation matrix distance
Δd	Distance difference
$\Delta\theta$	Angle difference
ΔPL	Pathloss increase
c	Channel matrix collinearity
d	Distance
f	Frequency
h	Height
t	Time
v	Speed

G	Gain
$\mathbf{H}$	Channel matrix
K	K-factor
$\mathbf{R}$	Correlation matrix

Abstract

Beyond 4G wireless networks are envisioned to provide ubiquitous connectivity with ultra high capacity density in dense urban environments. For this purpose, an innovative architecture of the multi-beam Base Station (BS) providing high capacity backhaul links to distributed Relay Stations (RSs) which make access links to multiple users in a hierarchical wireless network is introduced recently. However, performance of any wireless network heavily depends on the underlying wireless propagation channel. This is even more important for the network which relies on aggressive frequency reuse (and thus heavy temporal and spectral interference), and unprecedented deployment scenarios (thus unseen spatial signal and interference propagation characteristics).

With that perspective, three main components of such hierarchical wireless network are investigated in a top to bottom manner. Two modeling approaches, deterministic and empirical, are used in this thesis to characterize and model the underlying wireless propagation channels. An enhanced Ray-Tracing (RT) tool is used to characterize peculiarities of the multi-beam BS antenna and crucial parameters of relay designs, while two realistic measurement campaigns are conducted at 3.8 GHz in a typical urban microcellular environment to characterize various aspects of multi-user channels.

Based on the novel BS architecture, a pathloss model is derived taking into account specificities of the narrow beamwidth antenna, and compared with existing channel models. Impact of the BS antenna on polarized Multiple-Input Multiple-Output (MIMO) aspects is investigated. Moreover, the potential of the array optimization technique in multi-beam antennas is explored to reduce the amount of Co-Channel Interference (CCI) due to excessive frequency reuse in narrow beams as well as Inter-Cell Interference (ICI) due to same frequency beams of the neighbouring cell. The system level simulations are included to show improvements in throughput densities and grade of service (delay and probability of retry).

In order to ensure efficiency of relay architecture designs in wireless networks, two critical parameters are investigated: (*i*) the orientation and (*ii*) the height of the RS. A significant pathloss reduction of 10 to 15 dB is shown by orienting the relay antenna in the largest power ray direction through RT simulations. Further, the favourable RS height in terms of pathloss is investigated to provide high quality backhaul link. A trade-off between achievable pathloss and interference from the adjacent cell is suggested such that the RS is enabled with high Signal-to-Interference Ratio (SINR).

Multi-user MIMO (MU-MIMO) techniques consider multiple users in a single cell network to maximize the sum-throughput rather than the link throughput and to manage the resulting multi-user interference. However, the promised leverage of MU-MIMO largely depends upon the decorrelation (i.e. separation) between multi-user links. In this context, first the validity of the Wide-Sense Stationarity (WSS) assumption is experimentally assessed for non-stationary (users) MIMO propagation channels through the Channel Matrix Collinearity (CMC) metric. Using an appropriate threshold value, typical averaged statioarity distances are found in a range of 5 to 23 m depending upon the scenario under investigation. It is followed with characterization of multi-user separation through three metrics, (*i*) the Shadow Fading Correlation (SFC), (*ii*) the CMC and (*iii*) the Wideband Spectral Divergence (WSD). The empirical evidence illustrates that multiple users can be considered separated in the sense of MU-MIMO when they are physically separated by a distance of 8 to 12 m or an angle of $2°$ to $6°$. Furthermore, multi-user separation results are shown roughly irrespective of the investigated metric (or, equivalently, the related signal processing aspect). For each evaluated metric, empirical multi-user separation models are also proposed.

CHAPTER 1

Introduction to Beyond 4G Networks and Channels

This chapter describes the evolution and salient features of wireless communication networks. It presents the architecture and key features of the latest Fourth Generation (4G) networks, Long Term Evolution (LTE) and LTE-Advanced. Moreover, an introductory overview of beyond 4G networks and posed propagation challenges are highlighted, while focusing on multi-link channels as well as related interference issues.

1.1 Evolution of Wireless Networks

In the last decades, wireless communication has evolved from being an expensive technology for a few individuals to ubiquitous networks used by a majority of the world's population. The wireless communication networks have been continuously evolving since the 1st-Generation (1G) in the 1980s. Several systems such as Nordic Mobile Telephone (NMT) in Nordic countries, Total Access Communication System (TACS) in Europe, Advanced Mobile Phone Service (AMPS) in USA and J-TACS in Japan were started in 1G [1]. These networks were based on the analogue technology and designed only for the voice services [2].

The widely deployed Second Generation (2G) wireless networks are the Global System for Mobile communications (GSM). The digital technology brought an opportunity to increase the capacity of the networks, to give a more consistent quality of the service, and to develop much more attractive and truly mobile devices. GSM networks are still designed for the narrow-band voice and limited data services at a modest peak data rate of 9.6 Kbps [2]. The primary data services in 2G are Short Message Services (SMS) and circuit-switched data services enabling e-mail and other data applications. Higher data rates are introduced later in evolved 2G networks by assigning multiple time slots to a user and through modified coding schemes. Packet data became a reality with General Packet Radio Services (GPRS) introduction in GSM. With this technology, theoretical data rates reached to 115 Kbps. The next improvement to GSM is Enhanced Data Rates for Global Evolution (EDGE). The key enhancement of EDGE is a new modulation scheme called 8-Phase Shift Keying (8PSK). It increased the data rate of standard GSM up to 384 Kbps [1].

The International Telecommunication Union (ITU) initiative on International Mobile Telecommunications 2000 (IMT-2000) paved the way for evolution to Third Generation (3G). The Wideband Code Division Multiple Access (WCDMA) based concept was proposed by European and Japan research groups separately and standardization activities for 3G started in 1996 [2]. Finally, WCDMA proposals from Europe and Japan were merged in early 1998 and came out as part of the winning concept in the European work on Universal Mobile Telecommunication Services (UMTS), the European name for 3G. Standardization of WCDMA continued in parallel in several groups until the end of 1998, when the Third Generation Partnership Project (3GPP) was formed by standards-developing organizations from across the world [2]. This solved the problem of trying to maintain parallel development of aligned specifications in different regions. The present organizational partners of 3GPP are ARIB (Japan), CCSA (China), ETSI (Europe), ATIS (USA), TTA (South Korea), and TTC (Japan) [2].

3G is referred to as WCDMA in 3GPP because it uses a larger 5 MHz bandwidth relative to 1.25 MHz bandwidth used in CDMA2000 systems (3GPP2). UMTS employing WCDMA radio access technology is developed to offer greater spectral efficiency to mobile network operators. UMTS supports a peak data rate of up to 2 Mbps over a new wideband air interface. The 3GPP introduced High-Speed Packet Access (HSPA) in order to improve the UMTS performance [1]. The improvements are achieved through a new modulation Quadrature Amplitude Modulation (16QAM), reduced radio frame lengths and new functionalities within radio networks. In HSPA, both voice and data can be carried on the same 5 MHz carrier. The peak data rates of 14 Mbps in the downlink and 5.8 Mbps in the uplink can be achieved with High-Speed Downlink Packet Access (HSDPA) and High-Speed Uplink Packet Access (HSUPA) provided by 3GPP in release 5 and 6 respectively [1]. HSPA+, an evolution of HSPA given in release 7, adds MIMO antenna technology and 16QAM (for uplink)/ 64QAM (for downlink) modulations. These new features allow rate rate up to 11 Mbps for the uplink and up to 42 Mbps for the downlink [1]. Fig. 1.1 illustrates the time-line of evolution of wireless mobile networks.

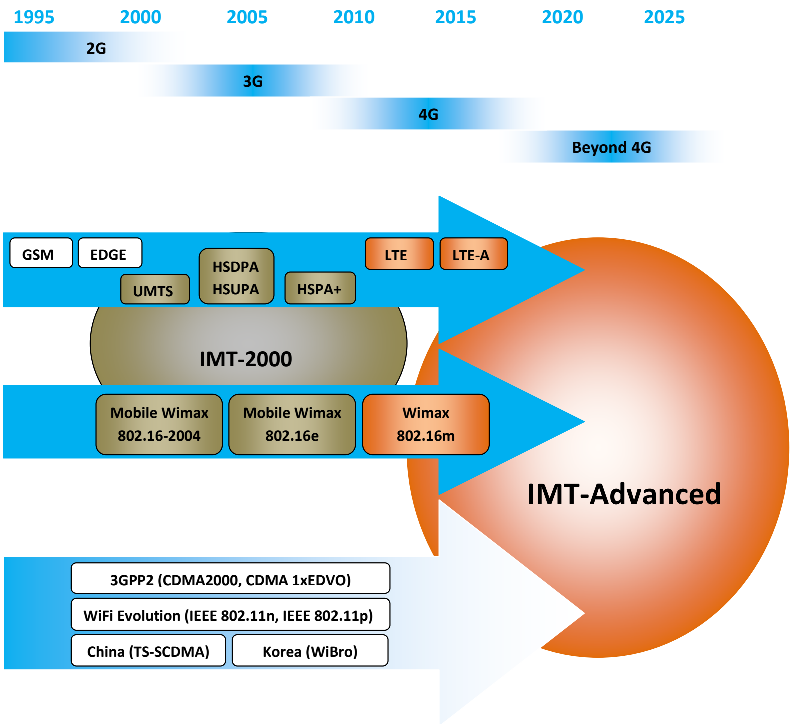

Figure 1.1: Evolution of wireless mobile networks

Parameters	GSM	UMTS	HSPA	LTE	LTE-A
Frequency bands	850 MHz 900 MHz 1800 MHz 1900 MHz	2 GHz	2 GHz	Multiple operating bands	LTE and new bands
Channel bandwidth	200 KHz	5 MHz	5 MHz	up to 20 MHz	100 MHz
Access scheme	FDMA/ TDMA	WCDMA	WCDMA	OFDMA (DL) SC-FDMA (UL)	Multi-carrier, Relay
Modulation	GMSK	4QAM	16QAM	QPSK, 16QAM, 64QAM	Evolution of LTE
Switching technology	Circuit	Circuit	Packet	Packet	Packet
Peak data rate	9.6 Kbps	2 Mbps	14 Mbps (DL) 5.8 Mbps (UL)	300 Mbps (DL) 75 Mbps (UL)	1 Gbps
MIMO	SISO	SISO	SISO	4×4 (DL) 1×2 (UL)	8×8 (DL) 4×4 (UL)

Table 1.1: Summary of key parameters of wireless mobile networks

1.2 LTE and LTE-Advanced (4G)

Long Term Evolution (LTE) is often referred to as the 4th-generation (4G) by marketing people, but others (mostly technical people) claim that LTE-Advanced (release 10) is the true 4G evolution step. Nevertheless, LTE can be included in IMT-Advanced family as a first wireless network initiated by 3GPP. LTE targets to provide a high data-rate, low-latency as well as a packet-optimized radio-access technology supporting flexible bandwidth deployments [3]. LTE supports downlink peak data rates of 326 Mbps with the support of 4×4 Multiple Input Multiple Output (MIMO) technology within 20 MHz bandwidth. Since the uplink MIMO is not employed in the first release of the LTE system, the uplink peak data rates are limited to 86 Mbps. Orthogonal Frequency Division Multiplex (OFDM) is selected for the downlink and Single Carrier-Frequency Division Multiple Access (SC-FDMA) for the uplink. In addition to peak data rate improvements, LTE provides two to four times higher spectral efficiency relative to HSPA. In terms of latency, LTE radio-interface and network provide capabilities for less than 10 ms for the transmission of a packet from the network to the user [3,4]. Table 1.1 summarizes the key features of wireless mobile networks from GSM to LTE-Advanced [2–4].

To allow ubiquitous connectivity with sufficient bandwidth, robustness and latency, ITU envisioned a new wireless access supporting even higher data rates with high mobility. Therefore, ITU introduced a new platform in 2008, called IMT-Advanced, to define the wireless networks with enhanced capabilities compared to that of IMT-2000. New capabilities of IMT-Advanced systems are envisaged to handle a wide range of supported data in multi-user environments with target peak data rates of up to 100 Mbps for high mobility and up to 1 Gbps for low mobility users. In this perspective, LTE work by 3GPP in release 10, named as LTE-Advanced, is of particular interest as it is the major technology approved by ITU for IMT-Advanced radio interface technologies [2, 4]. LTE-Advanced (release 10) is therefore seen as the next major evolutionary step in the continuing development of LTE. With LTE-Advanced, the 3GPP aims to fulfil and even go beyond IMT-Advanced targets [3,4]. Release 12 and 13 are under discussion within the 3GPP framework. Fig. 1.2 summarizes the key LTE-Advanced features that can be deployed flexibly on top of LTE networks. The details of key technical features are briefly described in the following sections.

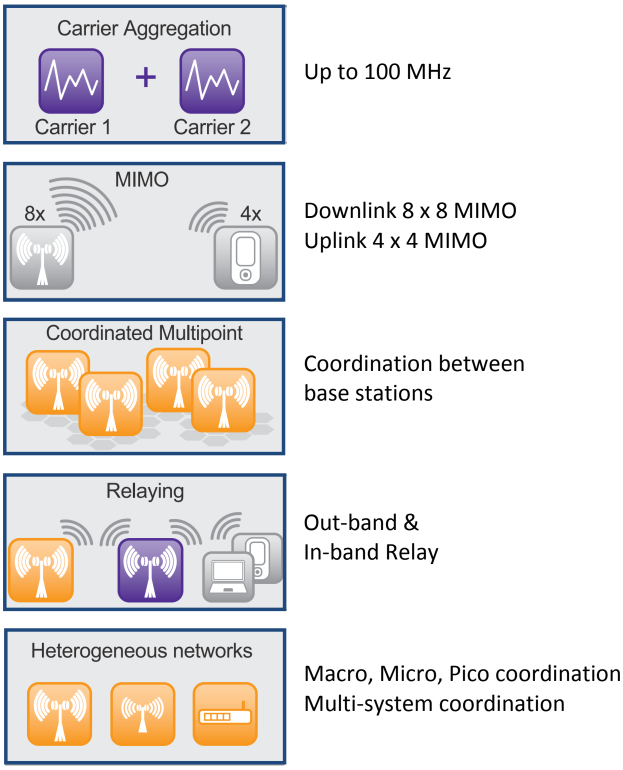

Figure 1.2: Key features of LTE-Advanced networks

1.2.1 Carrier Aggregation

LTE-Advanced networks offers peak rates of 1 Gbps by using carrier aggregation. Since it is crucial to preserve backward compatibility with LTE, the necessary bandwidth extension is provided by aggregation of multiple LTE carriers in LTE-Advanced [2]. It means that LTE-Advanced will be deployed in LTE occupied spectrum, with no impact on existing LTE terminals. Each LTE carrier, also called component carrier, can have a bandwidth up to 20 MHz and a maximum of five component carriers can be aggregated for bandwidth extension. Hence, a maximum bandwidth of 100 MHz is proposed for LTE-Advanced. The number of aggregated carriers can be different in the downlink and the uplink, but uplink component carriers cannot be larger than those in the downlink. The individual component carriers can also be of different bandwidths.

The easiest approach to organize aggregation is to use contiguous component carriers within the same frequency band (for LTE), called intra-band contiguous. Fig. 1.3 presents an example of the contiguous component carriers. However, accessing a large amount of contiguous spectrum in order to obtain the total bandwidth of 100 MHz is not always possible. Therefore, LTE-Advanced also allows for aggregation of non-contiguous component carriers in separate spectrum to handle situations where large amounts of contiguous spectrum are not available. However, the aggregation of non-contiguous spectrum is challenging from an implementation perspective, especially concerning the terminal support.

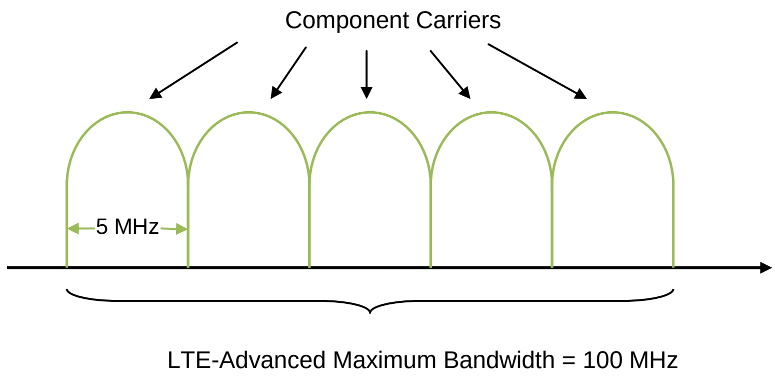

Figure 1.3: An example of contiguous carrier aggregation

1.2.2 Enhanced MIMO

LTE-Advanced employs enhanced multi-antenna schemes to achieve the peak rates of 1 Gbps. Multi-antenna technologies including beam-forming and spatial multiplexing are key features which are already in use for LTE. These technologies continue to play an even more important role in LTE-Advanced. 3GPP have proposed, as a major change, MIMO configurations up to 8×8 for the downlink and up to 4×4 for the uplink in release 10. Note that in LTE, the downlink supports 4×4 MIMO (four spatial layers assuming four users) and the uplink supports 1×2 (assuming a diversity receiver) per user. Spatial multiplexing allows several independent data streams (named spatial layers in 3GPP) to be transmitted over the same time and frequency resources. Such spatial layers can be used in two different ways,

- when all the spatial layers are allocated to a single user, the scheme is called Single-User MIMO (SU-MIMO).

- when the spatial layers are split among several users provided that they can be spatially separated, the scheme is called Multi-User MIMO (MU-MIMO).

Fig. 2.4 illustrates the principle of SU- and MU-MIMO for only two spatial layers. Nevertheless, spatial multiplexing is only applicable in good wireless channel conditions and under specific channel properties [1]. Note that data streams can be affected by channel fading of various types, which can also be seen as some type of code caused by the wireless propagation channel [4].

1.2.3 Coordinated Multi-point

LTE-Advanced aims to raise spectral efficiency through Coordinated Multi-Point (CoMP) transmission, which refers to multi-antenna transmission simultaneously from multiple Base Stations (BSs) or cells. It is an advanced variant of MIMO to improve cell-edge throughput and system throughput in dense scenarios. In CoMP, if a user in the cell-edge region is able to receive signals from multiple cell-sites, the overall performance can significantly improve provided that the system coordinates this multiple reception. CoMP is suggested for both downlink and uplink in LTE-Advanced [4]. Two types of CoMP techniques proposed by 3GPP are,

- Coordinated scheduling and beam-forming: In the downlink, CoMP enables coordinated scheduling and beam-forming from two or more BSs. However, only one BS transmits the data while others coordinate to reduce interference.

- Joint-processing: the transmission to a single user is simultaneously carried out from multiple BSs. The geographically separated multi-antenna BSs will coordinate to act as a single transmitter. This technique has potential to provide better performance compared with coordinated scheduling and beam-forming but has stringent requirements on backhaul communication.

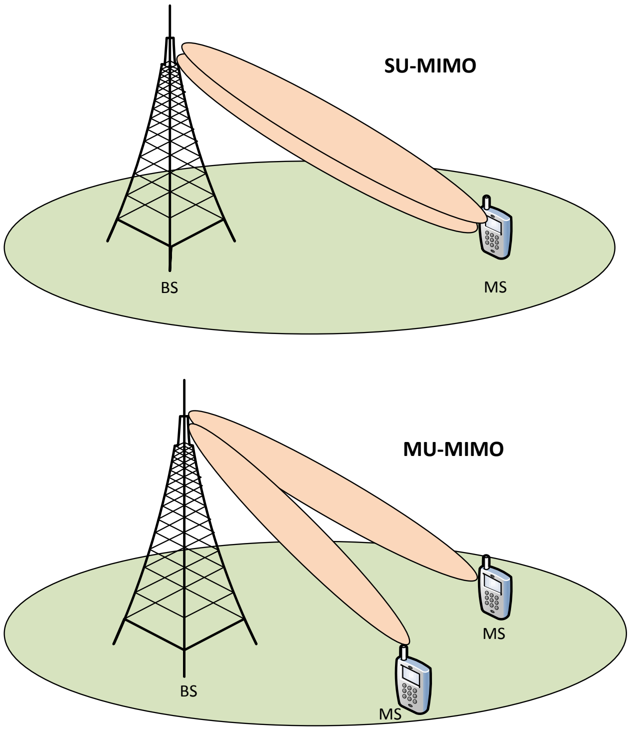

Figure 1.4: Examples of SU-MIMO and MU-MIMO systems

An example of CoMP is given in Fig. 1.5, where three BSs coordinate to serve a single user. Although CoMP is considered as a potential feature to improve cell-edge throughput and spectral efficiency, the implementation part must overcome some serious challenges such as,

- the network needs to be time-synchronized with the same accuracy as for Time Division Duplexing (TDD),

- the network requires a good knowledge of wireless channel between all coordinated BSs and users for the downlink communication, thus increasing the measurement load at the user as well as the feedback overhead,

- CoMP transmission requires a significant increase on the backhaul

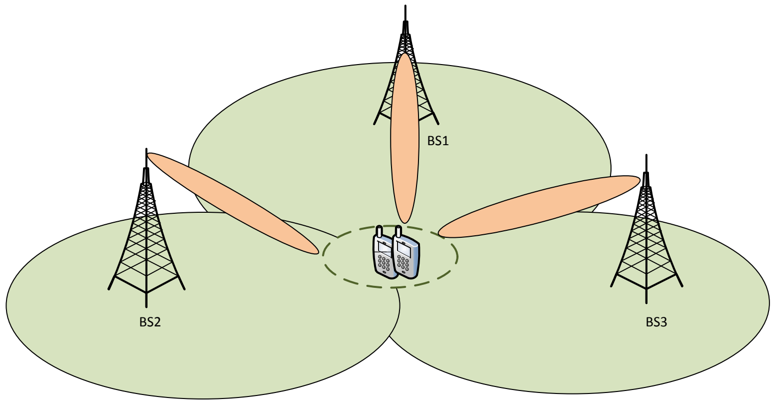

Figure 1.5: An example of CoMP with three collaborating BSs (cells)

network in order to exchange information between coordinated entities.

1.2.4 Relaying

In LTE-Advanced networks, the use of relaying is another feature to improve coverage in coverage-limited conditions, e.g., indoor or dead zones in dense urban environments, or coverage extension in rural areas. The concept of relaying is not new but the level of sophistication continues to grow. The basic and legacy relay concept is the use of a radio repeater which receives, amplifies and then forwards the downlink and uplink signals to cover so-called coverage-limited conditions. The relay can be positioned at the cell edge or in other areas of poor coverage. Typically they receive and retransmit an entire frequency band, so they must be positioned carefully. In general, repeaters can improve coverage but do not substantially increase the capacity. Fig. 1.6 shows a typical relay-assisted network, where a Relay Station (RS) serves multiple Mobile Stations (MSs) on one side, whereas it is connected to the BS on the other side. In LTE-Advanced, the RS will connect to the BS in one of two ways,

- in-band, also referred to as in-channel, in which the BS-to-RS link shares the same carrier frequency with the RS-to-MS link,

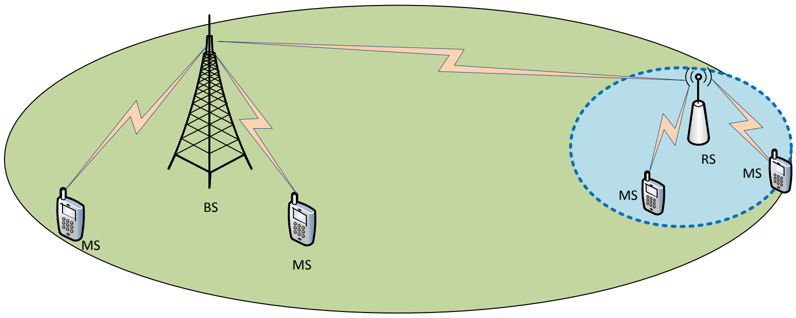

Figure 1.6: An example of the relay-assisted wireless network

- out-band, in which the BS-to-RS link does not operate in the same carrier frequency as the RS-to-MS link.

In the former approach, there is a risk of self-interference in the RS. This can be avoided through time sharing between two different links. The users at the edge of cell are connected to the RS, while users closer to the BS are directly connected to the BS. For both in-band and out-band relaying, it will be possible to operate the BS-to-RS link on the same carrier frequency as BS-to-MS links [4]. In addition, use of the in-band backhaul can be optimized using narrow, point-to-point connections to avoid creating unnecessary interference in rest of the network.

1.2.5 Heterogeneous Networks

LTE-Advanced supports heterogeneous networks where co-existing large macro cells are combined with small micro-cells, pico-cells, and/or Wireless Fidelity (Wi-Fi) access points. Since traffic volumes are increasing quite rapidly, more cells will therefore be required to offer the necessary capacity. The importance of radio resource management is growing, because the network complexity is continuously increasing. The on-going work to develop more advanced methods of radio resource management includes self-optimization in LTE-Advanced as well.

1.3 Beyond 4G Networks

Currently LTE and LTE-Advanced networks are being rolled out to provide more capacity and enable new features in the networking world. It is expected that 4G technologies will continue to expand and evolve over the next years. However, evolution of wireless networks will not stop with LTE-Advanced and the underlying networks will keep improving beyond 4G. The ultimate goal is to offer consistently higher data rates within a limited bandwidth to a large number of users. It is foreseen that current networks will have difficulties in order to fulfil expected demands in certain application areas. Therefore, research initiatives have already been taken to advance the wireless network solutions in order to support up to 1000 times higher traffic volumes compared to 2010 traffic levels [5]. Beyond 4G networks are not being anticipated as completely new, rather as integration of both novel and existing access technologies such as LTE-A and Wi-Fi. Some initial thoughts are presented briefly how beyond 4G wireless networks will develop further over the period of next 10 years [5].

- The link level capacity is bound by the Shannon limit, however single-link Shannon limit is different than multi-link networks where several cells interact with each other. Efficiency of such networks can be enhanced by optimizing inter-cell interference. Today's spectral efficiency is typically between 0.5 and 1.0 bps/Hz/cell (for example HSPA), taking into account legacy terminal and backhaul limitations. It can be improved in the range of 5 to 10 bps/Hz/cell by using multi-antenna and multi-cell transmission and cooperation [5].

- The BS density is expected to increase by a factor of 10 in densely populated areas with a large density of active users. A large number of femto-cells are expected to be deployed in order to improve home and small office coverage. In addition, large base of Wi-Fi access points ($>$ 500 millions) can be utilized to carry traffic, mainly indoors. The combined impact of three enhancement factors, additional spectrum, improvements in spectral efficiency and large number of small cells are envisioned to enable 1000 times more capacity than today's networks [5].

1.4 Propagation Challenges of Beyond 4G Networks

The propagation characteristics of wireless channels are always vital in order to investigate the optimum network performance. The properties of wireless channels critically affect the spectral efficiency, capacity and throughput of the entire wireless network. Due to economic constraints and site availability, the architecture of beyond 4G networks will become significantly more heterogeneous in terms of antennas (number, height and patterns), supported frequency bands and bandwidths. Moreover, beyond 4G networks are foreseen to be deployed more densely than today's networks by using relays. Hence, such architecture will result in significantly increased propagation challenges compared with classical wireless networks. Therefore, understanding and characterizing the relevant propagation aspects is becoming ever important than before and need to be considered carefully. In the context of this thesis, we focus on multi-link channels and related interference issues for beyond 4G networks in the following sections.

1.4.1 Multi-Link Channels

The wireless channels involving more than two nodes that are spatially distributed over large areas are said to be multi-link channels [6]. In other words, multiple BSs, RSs and MSs coexisting in a certain environment create multi-link channels. It can be seen as an extension of the MIMO concept, where each node is comprised of a compact antenna array. The emergence of multi-user MIMO, distributed MIMO, and cooperative techniques for the development of beyond 4G wireless networks call for more advanced channel modeling across multiple links. The multi-link communication concept is further illustrated in Fig. 1.7, where a single BS is connected to several RSs which are serving multiple users (i.e., MSs). Although single-link MIMO channel models might be extended to multi-link channels by using the same models for multiple BSs and MSs, such practices are not validated yet [6]. Hence, adequate channel models are required to account for antenna specificities, multi-link channels correlation and potential interference aspects in an accurate and realistic manner.

It is generally accepted that small-scale fading of different links is uncorrelated, but large-scale parameters including shadow fading can be correlated. For multi-link MIMO channels, inter-link correlation is an

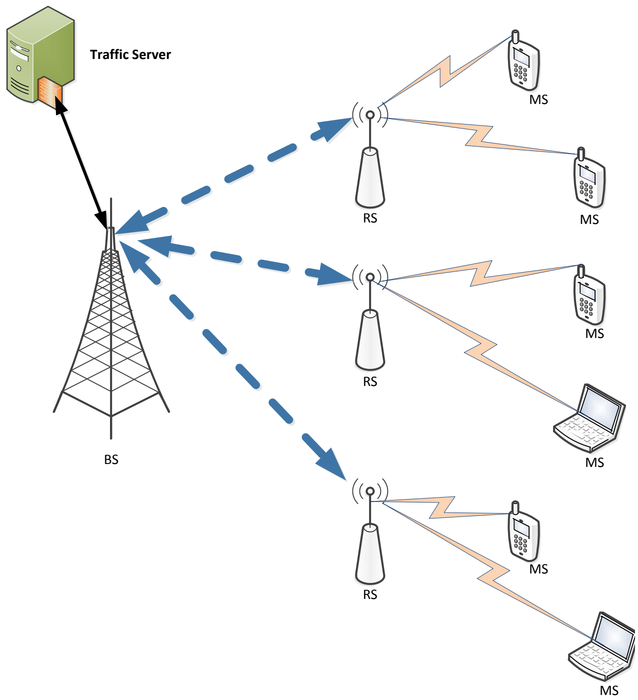

Figure 1.7: An example multi-link architecture

important quantity to be determined as it influences the overall system performance. It demands modeling of the physical propagation phenomena causing inter-link correlation. For example, a shadowing object (i.e., a common cluster) can affect multiple links, thus introducing inter-link correlation. Note that performance of MIMO systems exploiting spatial properties can seriously deteriorate, given the higher inter-link correlation due to common clusters. Therefore, multi-link channels experiencing strong correlation must be modeled in order to analyze the capacity of multi-link MIMO wireless networks.

1.4.2 Interference

The link performance of wireless networks is often limited by interference from other links of the network, its importance will considerably increase for beyond 4G wireless networks relying on multiple antennas in ultra-dense urban environments. For example, some possible interference scenarios in different conditions are described here:

- To address constantly increasing demands of high capacity density, multi-beam antennas are considered quite useful in the BuNGee project [7] as they allow the spatial reuse of spectrum and thus the spectral efficiency tends to increase as cell sizes are reduced. In addition, narrow antenna beams are utilized to suppress Co-Channel Interference (CCI) to an acceptable level. However, reducing the beamwidth lower than a certain level significantly increases the effective pathloss. Hence a trade-off between acceptable interference level and effective pathloss needs to be investigated. This implies that practical narrow beams have the potential to interfere with each other, thus not fully removing the CCI. The farther the co-channel beams are separated from each other, the lower the expected CCI level as the antenna pattern gradually tapers off with increasing angles from the boresight. In this context, it is imperative to characterize and possibly suppress such interference generated through multi-beam antennas as well as from neighbouring cell.

- Despite boosting peak data rates and spectral efficiency through MIMO technology, performance in the cell-edge area only improves a little because of interference from the neighbouring cell, known as Inter-Cell Interference (ICI). Indeed, the peak data rate can only be obtained in the most favourable propagation conditions, typically when users are relatively close to the serving BS. However, when users move away (towards cell-edge) the achievable data rates decrease. The cell edge issue will be even serious in beyond 4G wireless networks due to higher frequency bands and large number of antennas.

- Interference is particularly relevant in all MIMO systems and significantly harms spatial multiplexing. In the context of multi-link MIMO channels, if users have to share the network resources, interference may appear between various links. In particular, when multi-users MIMO channels are not sufficiently separated, they result in multi-user interference which in turn seriously deteriorates the sum capacity or overall network performance. Therefore, the multi-user separation must be characterized in order to achieve high throughput and capacity densities in wireless networks.

In this context, some techniques to characterize and suppress interference have already been introduced in state-of-the-art wireless channel models. However, increasing levels of interference demand more advanced work to characterize the interference.

1.5 Outline and Contributions

The thesis is organized into chapters each covering a specific component related to architecture of wireless networks and presented with a top to down system level approach. The overview and background for each topic is provided when necessary in the beginning of each chapter. Fig. 1.8 shows the structure of the thesis.

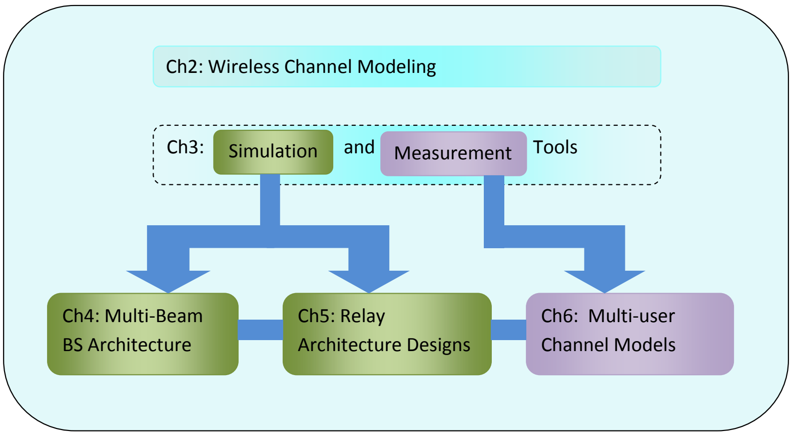

Figure 1.8: The structure of the thesis covering three main components of the wireless network architecture

Wireless Channel Modeling

This chapter introduces basics of wireless propagation channels including the multipath phenomena, propagation mechanisms and attenuation factors. The principles of channel modeling aspects are detailed including the MIMO channels. In addition, an overview of state of the art channel models is provided, while focusing on multi-link channel models and shadow fading correlation models. This investigation points out strong and weaker aspects of existing models in order to allow their use in relevant conditions and environments.

Simulation and Measurement Tools

The simulation and measurement tools used in this thesis to characterize and model wireless propagation channels are described in Chapter 3. It includes the basic physics involved in deterministic channel modeling approach, i.e., ray-tracing and types of ray interactions with the environment. In addition, a short description of the diffuse scattering model is provided which is recently implemented in the UCL ray-tracing tool [8] to capture components of the diffuse power along with its validation. A brief overview of state of the art ray-tracing models with extractable channel parameters and their application areas is also included.

In the second section of this chapter, an introduction of channel sounding techniques is provided. Since channel sounders require some modifications to measure multi-link channels, several techniques of multi-link measurements are discussed. Finally, features and technical details of the UCL-ULB MIMO channel sounder are described.

Multi-beam Base Station Architecture: Channel Models and Array Optimization

In order to provide increasing demands of ultra high throughput density in dense urban environments, an innovative architecture employing multi-beam antenna at the BS in hierarchical wireless networks is considered in the BuNGee project [7]. Based on the novel BS architecture, a pathloss model is evaluated taking into account specificities of the narrow beamwidth antenna. Subsequently, a comparison with existing channel models is drawn (see [9]). Impact of the multi-beam antenna on polarized MIMO aspects is characterized to reflect peculiarities of the novel architecture. The analysis includes important channel parameters such as the spatial fading, polarization-based covariance matrix and cross polarization discrimination (see [10]). The wideband aspects of fixed relay links are also characterized including a tapped delay line model for the considered architecture [10].

While the potential of multi-beam antennas combined with aggressive frequency reuse is exploited in the BuNGee project to increase the throughput density, a large number of narrow beams can cause CCI. In addition, beams of the neighbouring cell at the same frequency channel can contribute ICI. Since CCI is a direct consequence of antenna side-lobes, the potential of the array optimization technique (i.e., amplitude tapering in multi-beam antennas to reduce side-lobes) is investigated to reduce the amount of CCI (see [11]). Finally, system level simulations are carried out within the BuNGee project to demonstrate improvement in throughput densities and grade of service (delay and probability of retry) with optimized arrays of the multi-beam BS antenna [12].

Relay Architecture Designs

The relay architecture is considered as a network element designed to increase the network capacity and coverage in the context of BuNGee project [7]. The relay-associated parameters are required to be chosen carefully to ensure efficiency of relay architecture designs in wireless networks. With that perspective, two critical parameters are characterized in this chapter: orientation and height of the relay antenna. The optimal orientation of the relay antenna (i.e., the direction in which the main-lobe has to be steered) is investigated through RT simulations for four scenarios to maximize the potential relay contributions. Similarly, the favourable relay antenna height is characterized in terms of pathloss in order to provide high quality transmission for the BS-to-RS backhaul link. Both parameters are characterized for a square-cell topology in dense urban environments.

Multi-User Channel Models

The chapter presents characterization and modeling of multi-link and multi-user channels in a typical urban microcellular environment. First, the description of two measurement campaigns along with measurement scenarios, sounding equipment and utilized antennas is presented. It is followed with a brief description of the data post-processing and parameter extraction procedure. The behaviour of the underlying wireless channel can change due to movement of the transmitter and/or receiver as well as the scatterers in the surrounding environment. Consequently, the Wide-Sense Stationary (WSS) assumption can not be fulfilled infinitely but only for short intervals. Therefore, characterization of non-stationary MIMO propagation channels is critical, e.g., for the design optimization of adaptive wireless networks.

MU-MIMO techniques consider multiple users in a single cell network to maximize the sum-throughput rather than the link throughput and to manage the resulting multi-user interference. However, the promised leverage of MU-MIMO largely depends upon the decorrelation between multi-user links, also known as multi-user separation. With that perspective, the multi-user separation metrics are experimentally characterized in an urban microcellular environment. Three different metrics are evaluated, namely: the Shadow Fading Correlation (SFC), the Channel Matrix Collinearity (CMC) and the wideband Wideband Spectral Divergence (WSD). Experimental results in terms of multi-user distances and angles are analysed and quantified based on the measurement data (see [13]). Finally, an analysis explaining cross-correlation between investigated metrics is presented [13].

The last chapter concludes this thesis with a summary of overall contributions as well as a discussion about the possible future work.

CHAPTER 2
Wireless Channel Modeling

In wireless communication networks, the propagation channel is the medium between the transmitter (Tx) and the receiver (Rx). Its properties influence the performance of wireless networks. The knowledge of wireless channel is vital in the design (i.e., algorithms development) of next generation wireless networks. Especially in the context of beyond 4G networks, the behaviour of the channel can significantly change with choice of the BS architecture (multi-beam antennas), RS specificities (antenna orientations and heights) and multi-user/multi-link characteristics (density and separation). Hence, radio channel characterization and modeling in such innovative architectures becomes crucial to evaluate the achievable network performance. This chapter provides an overview of basic propagation phenomena, different approaches to model the wireless channel and existing channel models relevant to a single wireless link as well as multi-link MIMO channels.

2.1 Wireless Propagation Channels

This section describes the basic wireless propagation channel and multipath propagation phenomena.

2.1.1 Aspects of Multipath Propagation

The Tx transmits a signal in the form of electromagnetic waves in several directions, which interact with the surrounding environment through various propagation phenomena, before it reaches the Rx. The propagation phenomena possibly consist of specular reflections, diffraction, scattering, wave-guiding, penetration or any combination of these, as illustrated in Fig. 2.1 [6]. Therefore, multiple realizations of the transmitted signal, often termed as MultiPath Components (MPCs), are observed at the Rx with different amplitudes, delays and directions. The instantaneous Impulse Response (IR) of a wireless propagation channel can be written as,

$$h(t,\tau) = \sum_{i=1}^{N} \alpha_i(t)\delta(t-\tau_i), \tag{2.1}$$

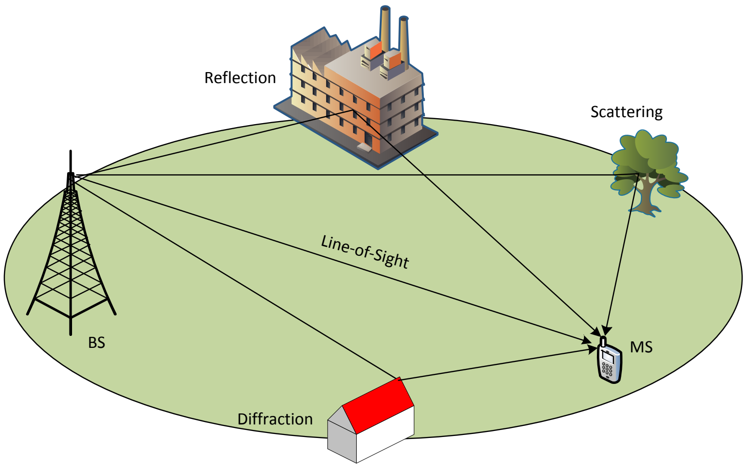

Figure 2.1: An illustration of multipath propagation

where δ is the Dirac delta function, N is the number of MPCs, and $\alpha_i(t)$ are complex amplitudes at respective delays τ_i. Since IR is the linear coherent superposition of all MPCs, which can be constructive or destructive depending upon their respective random phases, it can cause fading which may also deteriorate considerably the quality of the received signal. If all the frequencies of the transmitted signal are affected by different MPCs, fading is said to be frequency selective. Furthermore, the propagation channel varies over time due to movements of the Tx and/or the Rx and scatterers present in the vicinity. Each MPC experiences a unique frequency shift, therefore the propagation channel is said to be the time selective.

For a given link between the Tx and the Rx, the propagation channel is usually described by its IR, $h(t, \tau)$ [14, 15]. It links the input signal at the Tx with the output signal at the Rx through the following well-known relation,

$$y(t) = h(t, \tau) * x(t) + n(t), \tag{2.2}$$

where $x(t)$ and $y(t)$ are the transmitted and the received signal respectively, $n(t)$ denotes the additive noise at the Rx, and the operator $*$ represents the convolution operator. Fig. 2.2 shows an example of measured channel IRs where several propagation paths to generate IRs can be noticed. Note that each propagation path is influenced by the fol-

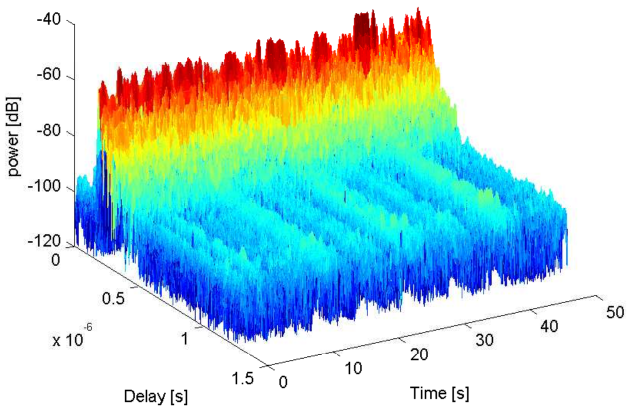

Figure 2.2: An example of measured channel IR

lowing:

- the Tx antenna in the direction of transmission of the propagation path
- the propagation channel on the propagation path
- the Rx antenna in the direction of arrival of the propagation path.

A block diagram of the measurement system depicting the wireless propagation channel with the Tx and Rx antennas and associated Radio Frequency (RF) cables is shown in Fig. 2.3. Thus derived channel models will be very specific to antennas utilized during measurements.

Similarly, the frequency-dependent transfer function can be described by applying a Fourier transform on (2.2),

$$Y(f) = H(t, f)X(f) + N(f), \tag{2.3}$$

where Y, H, X and N are the Fourier transforms of y, h, x and n respectively.

2.1.2 Narrowband and Wideband channels

Wireless channels are generally categorized into narrowband and wideband channels based on the relationship between the transmission bandwidth and the coherence bandwidth [15]. Narrowband channels have a

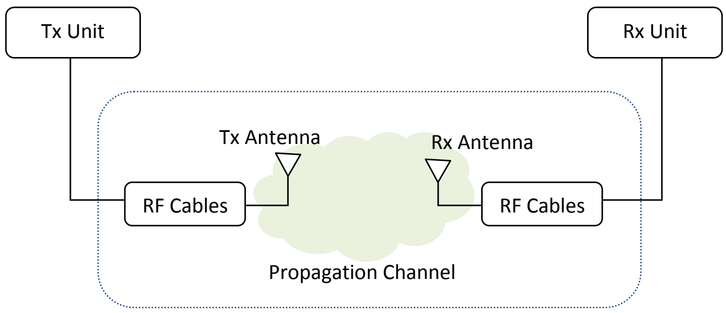

Figure 2.3: Block diagram of the measurement system

small bandwidth (transmission bandwidth is less than the coherence bandwidth) such that the Rx is not able to resolve multiple MPCs. The frequency response of such channels is invariant over the transmission bandwidth, therefore named as frequency flat fading channels. The IR of narrowband channels can be described by a single tap, i.e., a delta function with a time-varying attenuation.

$$h(t, \tau) = \alpha(t)\delta(\tau). \tag{2.4}$$

In contrast, wideband channels have large enough bandwidth (transmission bandwidth larger than the coherence bandwidth) to distinguish a frequency-dependent channel behavior. The frequency response of such channels varies over the transmission bandwidth, therefore also said to be frequency-selective fading channels. Moreover, such channels have more precise temporal resolution and the Rx has the ability to resolve the MPCs based on their respective delay. The directional properties (for both types of channels) at the Tx and at the Rx define the autocorrelation function of the IR when a mobile receiver moves in space. If multiple antennas are used at both sides, the correlation is defined by directional characteristics of the channel.

2.2 Wireless Channel Modeling

Since the channel modifies the Tx signal, mathematical models are required to capture channel characteristics relevant to performance of wireless networks. One of the major influences the wireless channel has on the Rx signal is attenuation relative to the Tx signal. The received power is influenced by a deterministic attenuation factor and random fluctuations. In fact, the received power is influenced by a product of three propagation phenomena; the pathloss, the shadow fading and the small-scale fading [16]. These are briefly described here.

2.2.1 Pathloss

Pathloss is the attenuation of the average received power as the distance between the Tx and the Rx increases. It is generally expressed in dB. The reduction in magnitude of the received signal depends on the type of the propagation environment, and denoted by the pathloss exponent n. Conventionally, pathloss is modeled as [17],

$$PL(dB) = PL(d_0) + 10n\log 10\left(\frac{d}{d_0}\right), \tag{2.5}$$

where d_0 is a reference distance. It is typically 1 km for urban macro-cell environments, 100 m for micro-cell environments and 1 m for indoor environments. The Pathloss exponent n denotes the relationship between the distance and the received power. It can have different values, e.g., 2 in free space, 3 in urban environments, 4 in indoor environments and 3 to 5 in bad urban environments [17]. Several pathloss models have been developed that take into account not only the distance between the Tx and the Rx, but also type of the environment, height of the Tx and Rx etc [16, 18].

2.2.2 Shadow Fading

Shadow fading, also known as shadowing, is defined as the random variations of locally averaged received power over large distances, typically on the order of a few hundred wavelengths, due to large obstacles such as buildings and terrain. The obstacles shadowing the propagation of MPCs can be very different from each other, resulting in large-scale variations at different locations, while having approximately the same Tx-Rx distance. At any distance d, shadow fading (S) measured in dB is usually modeled as a lognormal random variable, which takes into account random variations of the received power around the pathloss curve, with the Probability Density Function (PDF) as,

$$f(x) = \frac{1}{\sqrt{2\pi}\sigma_S x}\exp^{-\frac{(\ln x-\mu_S)^2}{2\sigma_S^2}}, \tag{2.6}$$

where μ_S and σ_S^2 are the mean and the variance of the corresponding normal random variable respectively.

2.2.3 Small-Scale Fading

Small-scale fading, also known as fast fading, describes the random fluctuations of the received power over short distances, typically a few wavelengths, due to constructive or destructive interference of MPCs impinging at the Rx. The interference pattern may change in space due to motion of the Rx or in time due to motion of the Tx or scatterers. Different distributions are proposed to characterize the random fading behavior of the signal envelope, suitable for different wireless systems and propagation environments. The Rayleigh and Rice distributions, both based on a complex Gaussian distribution, are the most commonly used models. Considering a large number of MPCs with amplitudes and random phases, the signal envelope of small-scale fading thus follows a Rayleigh distribution with PDF [15],

$$f(x) = \frac{x}{\sigma_{SS}^2} \exp^{-\frac{x^2}{2\sigma_{SS}^2}}, \quad x \geq 0. \tag{2.7}$$

It stems from a signal that is zero-mean complex Gaussian with a standard deviation σ, as motivated by the Central Limit Theorem (CLT) [15]. The zero-mean makes this distribution useful for Non Line Of Sight (NLOS) conditions. The Rayleigh is a special case of the Ricean distribution.

However, if a strong coherent component dominates the others, then signal envelope of small-scale variations follows the Ricean distribution with PDF given by,

$$p(x) = \frac{x}{\sigma_{SS}^2} \exp^{\left(-\frac{x^2+A^2}{2\sigma_{SS}^2}\right)} I_0\left(\frac{Ax}{\sigma_{SS}^2}\right), \quad x \geq 0, \tag{2.8}$$

where I_0 is the zero-order modified Bessel function of the first kind and A is the amplitude of the dominant component. Usually, the Ricean distribution is described by the Ricean K-factor, defined as [15],

$$K = \frac{A^2}{2\sigma_{SS}^2}. \tag{2.9}$$

Thus (2.8) can then be rearranged as

$$f(x) = \frac{x}{\sigma_{SS}^2} \exp^{-\left(K+\frac{x^2}{2\sigma_{SS}^2}\right)} I_0\left(\frac{\sqrt{2K}}{\sigma_{SS}^2}x\right), \quad x \geq 0, \tag{2.10}$$

where the Rician K-factor determines the amount of fading. This important parameter of the Ricean distribution represents the ratio between the average power of the specular and diffuse components of the signal. In this case, the small-scale fading has unit average power when $2\sigma_{SS}^2 = 1/(K+1)$. A Rician K-factor $K = 0$ corresponds to a Rayleigh fading distribution (i.e., strong fading conditions), while large values K indicate no fading (or weak fading conditions). Conventionally in the literature, the Rician distribution is often associated with the presence of an LOS component [15], however it can also be strong in presence of coherent specular reflections, e.g., a static scatterer located in the vicinity of the moving Rx [14]. The K-factor is a frequently studied parameter in channel modeling research; as illustrated in Chapter 4.

From a system design point of view, the type of fading distribution envelope is vital as it determines the fading margin [15] required to achieve coverage with a certain outage probability. A Ricean fading channel exhibits minimal fading at larger K values, and approximates an Additive White Gaussian Noise (AWGN) channel. The combined effects of large-scale and small-scale fading can be illustrated through a joint distribution, e.g., the Suzuki distribution [19]. However, the more familiar approach is to provide separate PDFs for two fading types.

2.2.4 WSSUS Considerations

A common approach used in statistical channel modeling is the Wide-Sense Stationary Uncorrelated Scattering (WSSUS) assumption. It is actually the combination of two independent assumptions [15]:

- The Wide-Sense Stationary (WSS) which implies that the channel statistics do not change with time and that the temporal autocorrelation function of the channel is only dependent on the lag, i.e., not on the particular time instant considered. This also requires a constant Doppler spectrum over time.

- The Uncorrelated Scattering (US) which implies that each path originates from independent scatterers or equivalently each tap of the IR fade independently.

However in practice, the spatial structure of the channel (i.e., the number, strength and direction of arrival of MPCs) changes considerably over time and/or space, hence require estimation of stationarity intervals. A stationarity region on the order of 10λ has been used traditionally for outdoor mobile scenarios [15]. However, a stationarity interval can be considerably shorter for indoor scenarios. A survey of the literature reveals that there are no universally accepted criteria to determine stationarity intervals within measurements.

2.2.5 Aspects of MIMO Channel Modeling

The propagation channels influence the achievable spatial diversity in MIMO systems. Therefore, adequate models of MIMO channels are desired both for network planning and for system simulation to design and compare MIMO algorithms. While channel models should optimally capture propagation effects which have impact on the system design, they should be simple to use as well. The multiple antennas at the Tx and the Rx require that the MIMO channel is specified for all Tx-Rx antenna links, as each link experiences different realization of the propagation channel. This means that if one link is affected by a deep fade due to interference of MPCs, then reliable communication is still feasible by using the other link (that will most likely not be in the fade, as fading effects vary quite rapidly from one antenna element to another). A schematic diagram of a MIMO system is shown in Fig. 2.4. For an $N_R \times N_T$ MIMO system, a time-variant wideband channel is represented by an $N_R \times N_T$ channel matrix,

$$\mathbf{H}(t,\tau) = \begin{bmatrix} h_{11}(t,\tau) & h_{12}(t,\tau) & \cdots & h_{1N_T}(t,\tau) \\ h_{21}(t,\tau) & h_{22}(t,\tau) & \cdots & h_{2N_T}(t,\tau) \\ \cdots & \cdots & \ddots & \cdots \\ h_{N_R1}(t,\tau) & h_{N_R2}(t,\tau) & \cdots & h_{N_RN_T}(t,\tau) \end{bmatrix}$$

where each element of $\mathbf{H}$ represents the time-variant IR between the $i-th$ Tx and $j-th$ Rx antenna, t is the absolute time and τ is the delay. For the MIMO case, the relation between the input and the output signal given in (2.2) can be written as,

$$\mathbf{y}(t) = \mathbf{H}(t,\tau) * \mathbf{x}(t) + \mathbf{n}(t), \tag{2.11}$$

where $\mathbf{x}$ represents a $N_T \times 1$ vector in which each line contains the signal transmitted on each transmit antenna, $\mathbf{y}$ denotes a $N_R \times 1$ vector containing the signal received on each receive antenna and $\mathbf{n}$ is the Rx noise.

MIMO systems are sensitive to the angular spectrum at the Tx and at the Rx [14, 20]. It determines the correlation between different elements of $\mathbf{H}$. For example, assume a communication link between BS

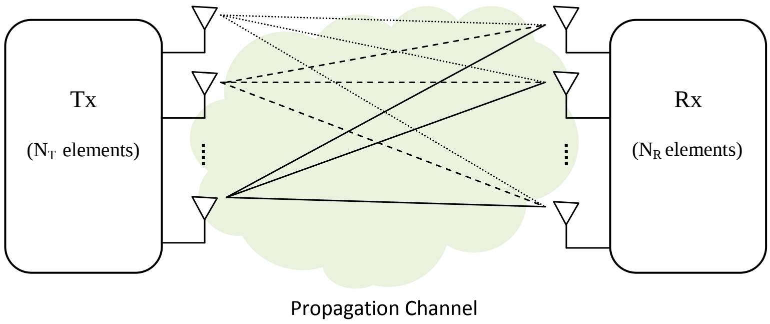

Figure 2.4: An $N_T \times N_R$ MIMO system

and MS (see Fig. 2.5), where MS is shadowed with a large building block (the only scatterer in its vicinity), which may result in a very narrow angular spread at the MS. In other words, all propagation paths arrive at the MS from approximately the same angle, thus introducing strong correlation between rows of the MIMO channel matrix **H** (it means independent and identical distributed assumption is not valid). In addition, combined Tx-Rx interactions increase complexity by causing correlation between different elements of **H** (i.e., rows and columns). Thus amount of correlation between elements of **H** helps deciding different signal processing techniques to be used. In case of uncorrelated matrix entries, diversity techniques can be used to exploit the propagation channel [21, 22]. In case of strongly correlation between matrix entries, beam-forming can be used to steer the Tx or Rx signals in a particular direction [23].

2.3 State of The Art Channel Models

The propagation channel models are important tools to simulate propagation phenomena without actually implementing the real communication systems [24, 25]. The wireless channel models can indeed be advantageous in network planning and system design by predicting the potential influencing sources. These can be useful in testing signal processing algorithms without actually building up the system, and to allow a better utilization and optimization of wireless resources. In wireless channel modeling, several classifications of modeling approaches can be made, though sometimes they overlap. This section provides a brief

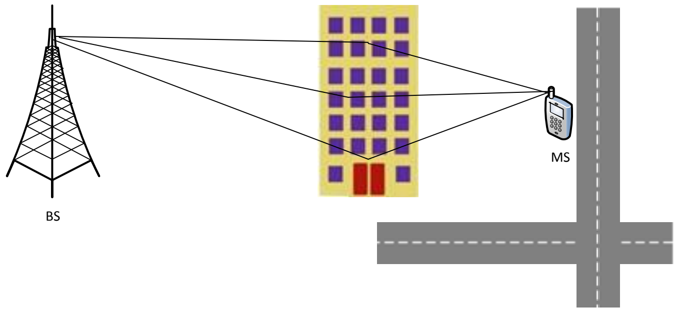

Figure 2.5: The propagation paths arriving at the MS with narrow angular spectrum

overview of the different approaches with their advantages, disadvantages and applications, while focusing on multi-link aspects. The choice of model mainly depends upon the application scenario and trade-off between acceptable accuracy and complexity.

2.3.1 Analytical Channel Models

The analytical models, also termed as stochastic models, provide the statistics of the channel matrix $\mathbf{H}$ by predicting the PDF of parameters such as delay, Doppler shift, Angle of Arrival (AoA), Angle of Departure (AoD), etc [24]. The parameters are usually extracted from experimental measurement campaigns, which may not necessarily require a physical justification. However, it is sometimes possible to give a physical explanation to measured statistical parameters.

The great mathematical simplicity of analytical channel models is one of their key advantages. On the contrary, the complexity of such models depends on the number of phenomena included in the model. For example, a MIMO channel can be modeled by channel fading statistics only; however it will require modeling of correlation matrix if one wants to include the inter-antenna correlation aspects. Nevertheless, defining environments with identical statistics is difficult. Different environments essentially provide diverse statistical properties. The major drawback of analytical channel models is their non-flexible nature. Since the influence of antennas is embedded in models, which effectively make the model applicable only to those antenna systems which are similar to one used for model parametrization, therefore they lack in generality. Another drawback is their incapability to detect non-stationarities in the channel. It means some peculiar conditions of propagation environments might not be covered with these models. Further classifications of analytical models are described here.

2.3.1.1 Tapped-Delay Line Model

The Tapped-Delay Line (TDL) model is one of the famous analytical models based on the WSSUS assumption. It is described by means of a finite number of delay taps spaced by 1/B (i.e., inverse of system bandwidth), each one assumed to fade independently with specified statistics (e.g., amplitude distribution, etc.). The delay taps can be either extracted from experimental measurement campaigns or ray-tracing simulations. The expectation distance to estimate average Power Delay Profile (PDP) is usually taken between 20λ to 40λ, where spacing between each point is one wavelength. TDL models are simple but are unable to capture some vital propagation aspects (e.g., non-stationarity) of the physical channels. This may cause a significant impact on the performance of communication systems.

2.3.1.2 Correlation-based Analytical Model

In correlation-based analytical model, the spatial correlation in the MIMO channel matrix $\mathbf{H}$ (over all elements) is used to model the spatial structure of the channel. Correlated MIMO channel matrices can be generated by correlating Independent Identically Distributed (i.i.d.) Gaussians, while a full correlation matrix $\mathbf{R}$ is estimated from measurements on $\mathbf{H}$. The analytical model with $\mathbf{R}$ (a scaled identity matrix) is a well-known i.i.d model. It corresponds to all entries of the Gaussian channel matrix $\mathbf{H}$ being independent of each other, where uniformly distributed MPCs in all directions provide the physical interpretation. This is usually referred to as a rich-scattering environment, and the antenna elements are spaced apart by at least half the carrier wavelength. For large array sizes, full correlation matrix $\mathbf{R}$ becomes cumbersome, however it can be approximated by introducing some assumptions.

The Kronecker Channel Model

The Kronecker model [26] approximates $\mathbf{R}$ by a Kronecker product of the antenna correlation matrices

$$\mathbf{R} = \mathbf{R}_{\mathrm{Tx}} \otimes \mathbf{R}_{\mathrm{Rx}}, \tag{2.12}$$

where $\mathbf{R}_{\mathrm{Tx}} = E[\mathbf{H}^H\mathbf{H}]$ and $\mathbf{R}_{\mathrm{Rx}} = E[\mathbf{H}\mathbf{H}^H]$ are the antenna spatial correlation matrices at the Tx and Rx side respectively and $\otimes$ is the Kronecker matrix product. The Kronecker model requires few parameters compared to the full correlation model. Its simplicity and ability to fit in measurement scenarios makes it a well-accepted choice for large number of communication algorithms. On the negative side, the Kronecker model generally underestimates the channel capacity [27].

2.3.1.3 Multi-Link Separation Models

In 4G (LTE and LTE-A)and beyond 4G wireless networks, each node will be equipped with multiple antennas, thus resulting multi-antenna channels can be correlated at the link level owing to the shadow fading. The shadow fading correlation between different links is an important factor which can affect the system performance considerably [28]. Therefore, multi-link models characterizing the separation (or distance) are introduced.

Shadow Fading Correlation Models

The Shadow Fading Correlation (SFC), expressed as ρ_S, is a complicated mechanism which occurs when two links share some dominant propagation paths. The goal of shadow fading correlation models is to propose simple methods to evaluate the shadow fading correlation between two links. Usually, two types of correlation is considered in cellular networks,

- **Auto-correlation** is the correlation between shadow fading of same BS-to-MS link at multiple locations (i.e., multi-user) in the moving path of MS, as illustrated in Fig. 2.6 for two users.
- **Cross-correlation** is the correlation between two links from two different BSs at the same MS location (i.e., single user), as depicted in Fig. 2.7.

Despite many years of research, presently there is no agreed-upon model for shadow fading correlation characterization. Therefore, characterization of only auto-correlation in terms of multi-user distance and angular difference is included in this thesis. The measurement-based analytical models of shadow fading found in the literature can generally be classified as:

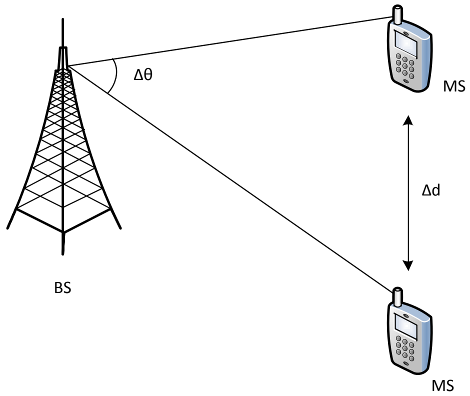

Figure 2.6: Definition of shadow fading auto-correlation

1. **Distance-only models** represent the shadow fading correlation as a function of the distance between the two users. These models actually better fit the shadow fading auto-correlation than the cross-correlation between users [29]. The most common auto-correlation model is a decaying exponential of distance [30], given by,
$$\rho_{\mathrm{S}}(\Delta d) = e^{-\left(\frac{\Delta d}{\Delta d_0}\right)^{v}}, \tag{2.13}$$
where Δd is the distance between users, Δd_0 corresponds to the decorrelation distance (mostly defined for $1/e$ correlation coefficient), and v is a tunable parameter, set to unity in the model of Gudmundson [30].

2. **Angle-only models** report the correlation as a function of the azimuth angle difference $\Delta\theta$ between the users and expressed as ρ_S. In [31], it is modeled as,
$$\rho_S(\Delta\theta) = e^{-\alpha\Delta\theta}, \tag{2.14}$$
where α is a tunable parameter.

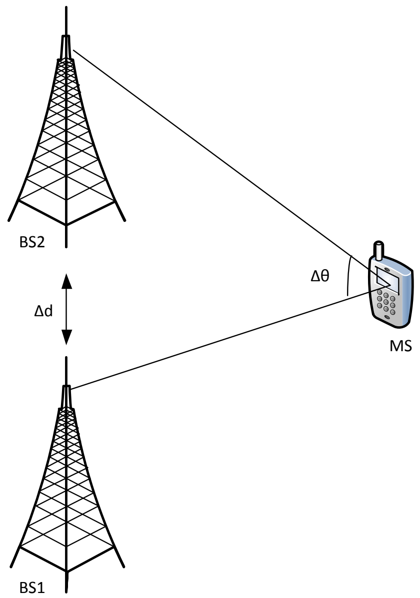

Figure 2.7: Definition of shadow fading cross-correlation

In [32, 33], a cosine model was proposed,

$$\rho_S(\Delta\theta) = A\cos\Delta\theta + B, \tag{2.15}$$

with two positive tunable parameters A, B and $A + B \leq 1$. In [34, 35], typical parameters are given as $A = 0.3$, $B = 0.5$ and [36, 37] provides $A = 0.3$, $B = 0.699$.

A piecewise linear model extracted from the measurement was given by [38],

$$\rho_S(\Delta\theta) = \begin{cases} 0.8 - \frac{\Delta\theta}{150}, & \Delta\theta \leq 60^\circ, \\ 0.4, & \Delta\theta > 60^\circ. \end{cases} \tag{2.16}$$

A similar linear model was also proposed in [89] as,

$$\rho_S(\Delta\theta) = \begin{cases} 0.78 - 7\Delta\theta/1250^\circ, & 0^\circ \leq \Delta\theta < 15^\circ, \\ 0.48 - 7\Delta\theta/1250^\circ, & 15^\circ \leq \Delta\theta < 60^\circ, \\ 0, & 60^\circ \leq \Delta\theta \leq 180^\circ. \end{cases} \tag{2.17}$$

3. **Angle-distance models** consider the effects of both angle and separation distance between users. These models can be constructed from the multiplication of distance-only and angle-only models, and often named as separable models. An example model is given in [39] as,

$$\rho_S(\Delta\theta, \Delta d) = \rho_S(\Delta d)\rho_S(\Delta\theta), \tag{2.18}$$

where

$$\rho_S(\Delta d) = e^{-\frac{\Delta d}{\Delta d_0}}, \tag{2.19}$$

and

$$\rho_S(\Delta\theta) = \begin{cases} 1, & \Delta\theta \leq 90^\circ, \\ 0, & \Delta\theta > 90^\circ. \end{cases} \tag{2.20}$$

In fact, the angle-distance approach is similar to angle-only, because within a same coverage area, the shorter distance between users most likely corresponds to small angle.

4. **Non-separable models** are more elaborate models where the distance and angle difference can not be separated, contrary to separable models. Saunders proposed a model in [28] which takes into account impacts of not only Δd and $\Delta\theta$ but also the Tx-Rx distance. It is written as,

$$\rho_S(\Delta d, \Delta\theta, d_1, d_2) = \begin{cases} \sqrt{\frac{d_1}{d_2}}, & \Delta\theta < \Delta\theta_0, \\ \sqrt{\frac{d_1}{d_2}} \left(\frac{\Delta\theta_0}{\Delta\theta}\right)^\gamma, & \Delta\theta \geq \Delta\theta_0, \end{cases} \tag{2.21}$$

where

$$\Delta\theta_0 = 2 \arcsin \frac{\Delta d_0}{2\min[d_1, d_2]}, \tag{2.22}$$

and Δd_0 is the decorrelation distance, d_1, d_2 are respective distances from Tx to Rx and γ is a positive tunable parameter, typically taken as 0.3 [28].

MIMO Multi-Link Separation

The degree of correlation in MIMO multi-links cannot be fully characterized by SFC only, because it does not provide any information on the alignment between the subspaces of different links. Therefore, the angular properties describing the subspace alignment should be considered in order to characterize MIMO multi-links. If two links share a common

Tx having a similar angular spectrum for both links, thus using space division access at the Tx is not possible, because both links are likely to be seen through the same subspace by the Tx array. The subspace separation appears therefore as critical parameters for the performance of multi-link signal processing techniques [29].

The MIMO multi-links separation can be characterized through various distance metrics [14, 40], the most important of them are detailed below.

1. **The channel matrix collinearity (CMC)** measures the amount of change in the spatial structure of two correlation matrices. It actually compares the subspaces of two complex valued matrices and assesses their similarity. The distance between two matrices $\mathbf{R}_1$ and $\mathbf{R}_2$ of same dimensions can be quantified by the collinearity as [14, 41],

$$c_{\mathbf{R},12} = \frac{\mathrm{tr}\{\mathbf{R}_1\mathbf{R}_2\}}{\|\mathbf{R}_1\|_f\|\mathbf{R}_2\|_f}, \tag{2.23}$$

   where $\mathrm{tr}\{.\}$ and $\|.\|_f$ are respectively the trace and the Frobenius norm of a matrix. The CMC ranges between zero (no collinearity, when the correlation matrices differ to a maximum extent) and one (full collinearity, when the correlation matrices are equal up to a scaling factor).

   Note that the Correlation Matrix Distance (CMD) denoted as $\Omega_{\mathbf{R}}$ is a special case of CMC which is only valid for Hermitian (or correlation) matrices [41]. It can be expressed as [41, 42],

$$\Omega_{\mathbf{R},12} = 1 - c_{\mathbf{R},12}. \tag{2.24}$$

2. **The condition numbers ratio** is another metric for similarity and can be expressed as,

$$\chi_{\mathbf{R},12} = 10\log_{10}\left(\frac{\sigma_{\max}(\mathbf{R}_1)}{\sigma_{\min}(\mathbf{R}_1)} \Big/ \frac{\sigma_{\max}(\mathbf{R}_2)}{\sigma_{\min}(\mathbf{R}_2)}\right), \tag{2.25}$$

   where $\sigma_{\max}(\mathbf{R})$ denotes the largest singular value of the matrix $\mathbf{R}$. The similarity between condition numbers is indicated by values close to 0 dB and a mismatch is reflected by positive or negative values of χ.

Note that above two metrics provide a different view of the (dis) similarity of the spatial structure of multi-link channels. On one side, the collinearity metric is sensitive to the alignment or non-alignment between the subspaces of different links. On the other side, the condition number ratio compares the degree of directivity of different channels.

2.3.2 Deterministic Channel Models

Deterministic channel models characterize the propagation channel in a site-specific environment, which has to be built with a certain level of accuracy. This requires details of the environment (i.e., a database) which include intrinsic properties of the physical objects (geometries, positions and material properties) as well as people and weather conditions etc. Ray-Tracing (RT) technique is widely accepted deterministic channel model [43]. In RT, several possible propagation paths between the Tx and the Rx in a particular environment are determined by using geometrical optical laws as presented in Fig. 3.2 [8, 44, 45]. Further details of RT model and developed tool are provided in Chapter 3.

The precise estimation of the propagation channel is one of the major advantages of deterministic models. They are often easy to use as no understanding of the underlying model is required. They can provide realistic field values for optimum positions (e.g., placement of a BS vital for telecom operators). RT models are used in urban macro-/microcellular environments and street canyons to determine average

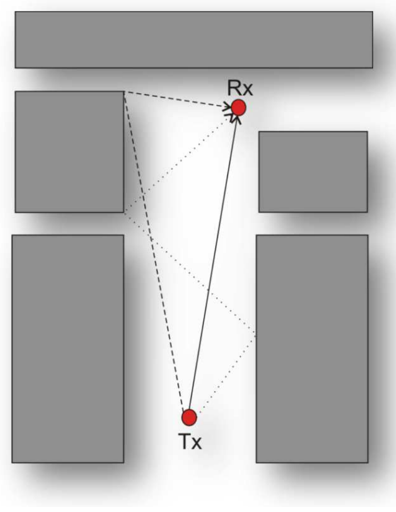

Figure 2.8: An example of ray-tracing model

received powers, pathloss coefficients, shadow fading values and Root Mean Square (RMS) delay spreads [8,46]. The computational complexity is the major disadvantage of deterministic models, depending upon the number of parameters (i.e., propagation phenomena) used to describe the specific environment and the required level of accuracy. It becomes highly complicated to enter all details of the environment in the RT tool, hence practical implementations compromise the accuracy.

2.3.3 Hybrid Channel Models

Hybrid models, or Geometry-based Stochastic Channel Models (GSCM), have characteristics of both analytical and deterministic models, hence often presented as an alternative balancing the generalization and complexity. In these models, the wave propagation and scattering aspects are decoupled. In GSCM models, the location of the scatterers is specified randomly according to suitable statistical distributions. Subsequently, MPCs are obtained through simple models (e.g., ray-tracing) for the propagation of rays and their interactions with scatterers. Each MPC is then assigned fading properties drawn from statistical distributions. The parameters of MPCs (e.g., fading properties) are adjusted automatically with movement of terminals or scatterers so that the correct fading correlation is generated. The concept of multipath clusters is often used in most variants of these models. Different types of hybrid models are presented in the following sections.

2.3.3.1 IEEE 802.16 Channel Model

The IEEE 802.16 channel model is a Correlation-Based Stochastic Model (CBSM), which is based on Stanford University Interim (SUI) models and was extended to cover relay scenarios in IEEE 802.16j Worldwide Interoperability for Microwave Access (WiMAX) systems. This channel model supports a centre frequency of 5 GHz and a maximum system bandwidth of 20 MHz. However, this model can be used in the frequency range 1 to 4 GHz. Pathloss models can also be used in the extending frequency range, with appropriate frequency correction factors. This model can be used for simulations, design, development, and testing of technologies suitable for broadband fixed wireless applications [47]. Some typical scenario details are given as follows,

- cells are less than 10 km in radius
- above rooftop BTS antennas (15-40 m)

- below rooftop directional Rx or relay antennas (2-10 m).

IEEE 802.16 presents nine types of channel models, Types A−H and Type J, commonly experienced in WiMAX multi-hop relay networks. The IEEE 802.16 model distinguishes between two different locations of BSs and RSs as Above Roof Top (ART) and Below Roof Top (BRT) respectively. Three terrain features are defined by IEEE 802.16, hilly terrain with moderate to heavy tree densities, intermediate pathloss condition, and flat terrain with light tree densities. Types A, B, C, F, and G support both LOS and NLOS conditions, Types D and H support only the LOS condition, while Types E and J support only the NLOS condition [48].

The IEEE 802.16 channel model is characterized by the following random parameters, pathloss (including shadow fading), multipath delay spread, Doppler spread, fading characteristics and co-channel interference. These parameters depend upon terrain, tree density, antenna height and beamwidth, wind speed and season. For modeling pathloss variations with different frequencies and receive antenna heights, correction terms have to be included. Furthermore, it employs a TDL structure to construct the wideband channel impulse response, with each tap representing a resolvable path or a cluster of scatterers with a different delay. The numbers of taps used in this channel model are fixed to 3. In IEEE 802.16 model, the correlation of lognormal shadow fading is perhaps the most important system-level correlation because it directly influences the macro-diversity gain. Therefore, it uses a distance-dependent exponential decaying function to describe the intra-site SF correlation (also called auto-correlation), and a distance and angle-dependent function to describe the inter-site SF correlation (also called cross-correlation).

Gain Reduction Factor

The use of directional antennas in wireless channels can increase the received power as much as the antenna gain. However, the gain due to the directivity can reduce because of the scattering, thus causing an increase in pathloss. The effective gain is less than the actual gain and characterized as antenna Gain Reduction Factor (GRF) denoted as ΔG_{BW}. The IEEE 802.16 channel model evaluates GRF parameter for directional antennas and recommends a careful consideration of directional antennas. This parameter is a random quantity (Gaussian distributed dB value) with a mean (μ_{GRF}) and standard deviation (σ_{GRF}) given by the IEEE

802.16 model [47],

$$\mu_{\mathrm{GRF}} = -(0.53 + 0.1I)\ln\left(\frac{\beta}{360}\right) + (0.5 + 0.04I)\left(\ln\left(\frac{\beta}{360}\right)\right)^2, \quad (2.26)$$

$$\sigma_{\mathrm{GRF}} = -(0.93 + 0.02I)\ln\left(\frac{\beta}{360}\right), \quad (2.27)$$

where β is the beamwidth in degrees, $I = 1$ for winter and $I = -1$ for summer, and ln is the natural logarithm.

GRF should be considered in the link budget of a specific receiver antenna configuration. In the link budget calculation, if G is the gain of the antenna (dB) and ΔG_{BW} is the GRF, the effective gain of the antenna equals $G - \Delta G_{\mathrm{BW}}$. For example, if a 20 degree antenna is used in an omnidirectional scattering scenario, the mean value of ΔG_{BW} would be close to 7 dB.

Fading Characteristics

The narrowband received signal fading can be characterized by a Ricean distribution. The key parameter of this distribution is the K-factor K. The model of the K-factor (in linear scale) for directional antennas is given by [47],

$$K = K_{\mathrm{omni}} \cdot \left(\frac{\beta}{17}\right)^{-0.62}, \quad (2.28)$$

where K_{omni} is the K factor for an omnidirectional antenna and β is the beamwidth (in degrees) of the directional antenna.

2.3.3.2 3GPP Spatial Channel Model

The Spatial Channel Model (SCM) developed by 3GPP [49, 50] is a geometry-based model. The validity range of SCM is narrow (i.e., carrier frequency of 2 GHz and system bandwidth of 5 MHz) as it is specifically established for 3G networks in urban micro-cells as well as suburban macrocells covering both LOS and NLOS scenarios. It is not defined as a continuous model, but prescribes a specific discrete implementation (i.e., Direction of Departures (DoDs), Direction of Arrivals (DoAs) and azimuth spreads are assigned fixed values). However, the model is constructed to incorporate correlations between these different large-scale parameters [29]. Hence, it does not allow for continuous, large-scale movements of the MS, but considers different possible segments of the mobile movement within the cell. The SCM provides implementation in form of a TDL model where each tap consists of several sub-paths sharing the same delay, but different directions of arrival and departure. Several defined options can be switched on to obtain a better agreement with real-world data, such as polarized antennas, far scatterer clusters, LOS, and urban canyons. Interference is handled by modeling strong interferers as spatially correlated, while weak interferers are taken as spatially white. Finally, shadow fading correlation is assigned fixed values of 0 when considering different MSs connected to a single BS and 0.5 when considering a single MS connected to multiple BSs.

The SCM actually served as first version (interim) of the WINNER model [51], in which number of additional parameters are included such as intra-cluster delay-spreads, a LOS and K-factor model for all scenarios, as well as time-variant shadow fading, path angles and delays. This is implemented by defining a number of large-scale parameters: the shadow fading standard deviation, the Ricean K-factor, the delay-spread and the directions spreads at departure/arrival. For a given link, the model fixes the large-scale parameters according to prescribed distributions. This implies that only short segments of successive channel matrices can be generated: these short segments correspond to one sample of large-scale parameters. Different segments (i.e., different periods of time for a given link) are related by correlating large-scale parameters as a function of the inter-segment distance, but clusters for each segment are generated for that segment only. This means that even though two segments can be very close, clusters (or scatterers) for each segment are generated independently: both segments share highly correlated large-scale parameters, but see totally different clusters. For any segment, the WINNER model then generates multipaths in a similar way as the COST approach, i.e., using clusters of scatterers.

2.3.3.3 WINNER II Channel Model

The WINNER II channel model (update of the WINNER channel model in 2007) is a system level model based on GSCM approach, which allows creation of an arbitrary double directional radio channel model [52]. It includes number of propagation environments (13 scenarios) for single or multi-links, while supporting multi-antenna technologies, polarization, multi-user, multi-cell, and multi-hop networks. The WINNER II model is applicable in a frequency range of 2 to 6 GHz and for system bandwidth up to 100 MHz. This model is antenna independent, i.e., different antenna configurations and element patterns can be inserted. The channel parameters are determined stochastically, based on statistically distributions extracted from channel measurements. Different scenarios are modeled using the same approach, but different parameters. Several measurement campaigns provide the basis for the parametrization of propagation scenarios for both LOS and NLOS conditions. This stochastic model has two level of randomness. First, large scale parameters (e.g., shadow fading, delay and angular spreads) and then the small scale parameters (e.g., delays, AoAs and AoDs) are drawn randomly according to distribution functions. It also employs a TDL structure to construct the wideband channel IR, with each tap represents a resolvable path or a cluster of scatterers with a different delay. The numbers of taps can vary between 4 and 24 [52].

Pathloss Aspects

With proper parametrization, WINNER II channel models are usually accurate and flexible for describing different scenarios. However, such models are complex and computationally inefficient, especially if one wants to account for the effect of narrow-beams directive antennas on pathloss. Pathloss models for various WINNER II scenarios have been developed based on measurement results as well as results from the open literature, however only two scenarios (which are similar to considered scenarios later in this thesis) are detailed here:

1. **Fixed Relay Scenario (B5f):** The sub-scenario B5f consists of relay antennas some meters above the rooftop or some meters below the rooftop. It covers the LOS/NLOS link between rooftop to below/above rooftop. It is possible to create LOS links with antennas below rooftop and NLOS links with antennas above the average rooftop. In 5Bf, it is also assumed that the RS is shadowed due to some obstacles. The pathloss model equation is given [52],

$$PL = A \log 10(d) + B + C \log 10 \left(\frac{f_c}{5} \right) + X, \tag{2.29}$$

where d [m] is the distance between the Tx and the Rx, f_c [GHz] is the system frequency, A is the pathloss exponent, B is the intercept parameter, C models the pathloss frequency dependence, and X is the optional environment-specific term. The parametric values to calculate pathloss for NLOS case are,

$$A = 23.5,\ B = 57.5,\ C = 23.$$

These values are given for heights h_{BS}= 25 m and h_{RS}= 15 m. In B5 scenario, one scatterer per cluster is assumed to be in motion while others are stationary. This model is based on the B5a LOS fixed relay model by attenuating artificially its direct component by 15 dB in average and adding up a normally distributed random number with standard deviation 8 dB.

2. **Urban macro-cell scenario (C2):** The urban macrocell environment (C2) considers outdoor MSs at street level (1.5 m from the ground) and fixed BSs clearly above surrounding building heights [52]. It represents mostly NLOS or OLOS propagation conditions, since street level is often reached by a single diffraction over the rooftop and it includes Doppler spread. Buildings in the urban macro-cell can form either a Manhattan like grid, or more irregular shapes. Building heights and density is mostly homogeneous; otherwise it results in a clearly dispersive propagation environment in the delay and angular domain [52]. To determine its pathloss, the following relations are given [52].

   LOS Model: If $d_{\mathrm{BP}} < d < 5$ km and h_{BS}= 25 m, h_{MS}= 1.5 m

$$PL = 40\log_{10}(d) + 13.47 - 14\log_{10}(h_{\mathrm{BS}}) - 14\log_{10}(h_{\mathrm{MS}}) + 6\log_{10}\left(\frac{f_c}{5}\right). \quad (2.30)$$

   NLOS Model: If 50 m $< d < 5$ km and $h_{\mathrm{BS}} = 25$ m, h_{MS}= 1.5 m

$$PL = (44.9-6.55)\log_{10}(d)+34.46+5.83\log_{10}(h_{\mathrm{BS}})+23\log_{10}\left(\frac{f_c}{5}\right). \quad (2.31)$$

Multi-Link Aspects

In WINNER II channel model, multiple links between BS, RSs and/or MSs can be simulated simultaneously, as shown in Fig. 2.9, running separate simulations for each link analogous to the SCM methodology. Regarding the correlation between multiple links, WINNER II models the shadow fading correlation between various BSs and a single MS (contrary to SCM, where correlation is considered 0) as well as the shadow fading correlation between various MSs links to a single BS (correlation is distance-dependent). This modeling is actually quite simple, and might reflect the reality.

The advantage of WINNER II model is that the large-scale statistics in a specific scenario are always guaranteed by any realization. However, the independent initialization of the propagation environment in each realization prohibits connecting different realizations, which is critical to characterize the time variations caused by the user movement. Typically, when new large-scale parameters such as the channel correlation in multi-link scenarios are included into the analysis, the entire initialization of the propagation environment must be re-defined, hence limiting the straightforward extension of the model.

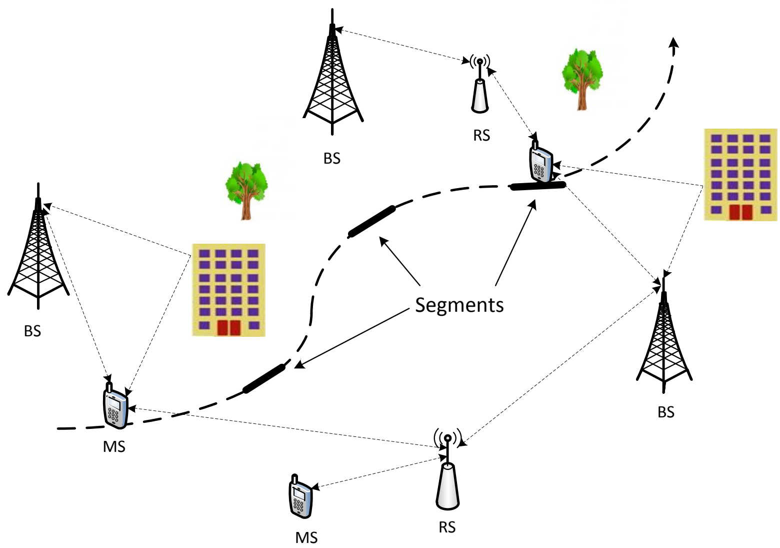

Figure 2.9: WINNER II multi-link model

2.3.3.4 COST Cluster-Based Channel Model

The COST 2100 channel model is Cluster-Based Channel Model (CBCM) that can reproduce stochastic properties of multi-link MIMO systems [53, 54]. It is the latest available channel model from COST family, established on the conception of previous COST models. The COST

259 directional channel model was originally established for the simulation of systems with multiple antenna elements at either the BS or the MS [29, 55].

COST 273 Model

The COST 273 model [56–58], visualized in Fig. 2.10, can be seen as the double-directional extension of the COST 259 model. It is a general geometric physical MIMO channel model valid for macro-cells, micro-cells and pico-cells. It is based on a generic structure of clusters, i.e., groups of MPCs which describe the wideband propagation channel in delay and direction domains. Each MPC is characterized by its delay, AoA, AoD, Elevation of Arrival (EoA) and Elevation of Departure (EoD). MPCs which are close, i.e., with similar delay and direction at both BS and MS sides are grouped into clusters. The angular domains can then be transformed into the spatial dimension for MIMO channel simulations. One of the main features of COST 273 model is that it uses a uniform structure to describe the local clusters, the single-interaction clusters and the multiple-interaction clusters. Another feature of the COST 273 model is the concept of Visibility Regions (VR) of each cluster (i.e., a circular region with fixed size in azimuth plane), which describes the cluster activity in the environment and is used to model non-stationary channels.

COST 2100 Model and Multi-Link Aspects

The COST 2100 model [53] is an extension of the COST 273 model considering the following,

- a polarization model of multipath contributions,
- addition of dense MOCs to specular contributions,
- multi-link (multi-cell, multi-user) MIMO scenarios.

However, we only focus multi-link aspects of this recent model by reminding that the single-link COST 273 and 2100 models are multi-user by definition, as the propagation environment is characterized with respect to one BS irrespective of the MS location, so that channels between one BS and multiple MSs dropped in different locations can be simultaneously modeled [29].

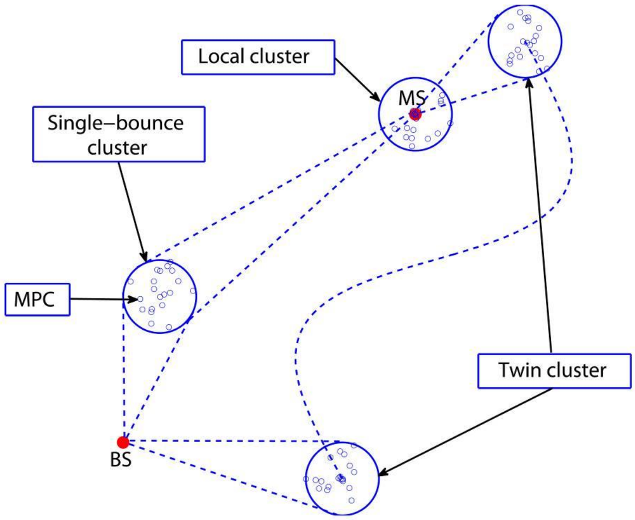

Figure 2.10: Representation of COST 273/2100 model with local, single bounce and twin-clusters

A similar principle was applied for COST 2100 model to describe channels in multiple-BS multiple-user scenarios, simply by adding up multiple single-link channel realizations. However, since clusters and corresponding visibility regions are generated separately and independently for each BS, there is no guarantee that multiple links reflect the important features of multi-link scenarios realistically, in particular the large-scale correlations, such as the shadow fading correlation [29]. One possible modeling approach is therefore to consider that clusters are simultaneously visible in different links, i.e., that some clusters are common between multiple links [59, 60]. This solution requires to characterize the cluster visibility in different links, and without altering the physical properties of clusters to guarantee the compatibility with the existing COST 259/273 approach. The extension to multi-link scenarios is thus achieved by considering that the visibility regions now define the cluster visibility to multiple BSs, i.e., the VR associated to a given cluster determines to which BS the cluster will be connected once an MS is located inside that VR. Typically, clusters will be associated to multiple VRs, and therefore, multiple BSs. Because of its recent extension, the COST 2100 model is a good candidate to investigate virtual MIMO schemes from the BSs to the MSs. The main drawback of this model is that it currently parameterized for a few environments only, including outdoor macro-cells and indoor pico-cells [29].

2.4 Conclusions

In this chapter, basic phenomena of wireless propagation channels have been presented to understand rest of the thesis. A number of channel modeling approaches have been reviewed and compared, in particular focusing on shadow fading correlation models, multi-link MIMO separation metrics and recent standardized hybrid channel models. Various advantages, disadvantages and applications of analytical, deterministic and hybrid channel models in different environments have been discussed. On the one side, mathematical simplicity of analytical models is advantageous, while complexity and non-flexible nature are main disadvantages. On the other side, deterministic models are realistic and site-specific, however require a certain level of accuracy and details of the environment (i.e., database) which increases the computational complexity. As an alternative, hybrid channel models balance the generalization and complexity comprise of both analytical and deterministic models. Therefore, it can be concluded that the choice of model mainly depends upon the application scenario and trade-off between acceptable level of accuracy and complexity.

CHAPTER 3
Simulation and Measurement Tools

In order to characterize and model the wireless propagation channel, two approaches are used in this thesis. First, an enhanced ray-tracing simulation tool is utilized to characterize wireless channels in various scenarios, in particular to analyze impact of the multi-beam BS antenna on channel characteristics. Same approach is applied to characterize interference in multi-links. Second, an extensive experimental measurement campaign is conducted to probe multi-link and multi-user characteristics of the wireless propagation channel. The basic principles of these distinct approaches and associated paraphernalia are detailed in this chapter.

3.1 Ray-Tracing

The deterministic approaches to model the wireless channel are Ray-Tracing (RT) and Ray-Launching (RL) [43, 61]. In such approaches, a ray represents propagation of the electromagnetic wave with certain characteristics, e.g., amplitude, phase, polarization, a direction and a position in space etc. The difference instigates from the algorithm used to find paths between the source and the observation point [62]. However, only RT is considered in this thesis as a useful tool for site-specific channel modeling in urban environments. Therefore, basics of the RT approach, the diffuse scattering model, its implementation along with validation and state of the art RT models are briefly described in this section.

In RT algorithms, Geometrical Optics (GO) technique is implemented according to the method of images. This technique is a high frequency approximation that can be used to describe the propagation of electromagnetic waves [8]. In GO, propagation is described in terms of rays that are used to evaluate paths as they interact with the environment. The applied principle in RT is to find a reflection point between the source and the observation point. It lies on intersection of the line which connects the observation point and the image with the surface on which reflection takes place [8].

3.1.1 Theory of Interactions

In practice, when an electromagnetic ray impinges a boundary between two media (with different refraction indices), it produces different interactions as depicted in Fig. 3.1. There are several types of interactions, however generally can be attributed to the following:

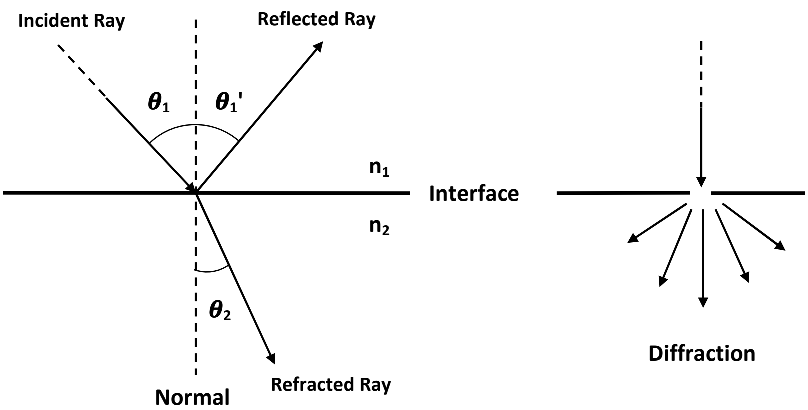

Figure 3.1: Illustration of propagation mechanisms: reflection, refraction and diffraction

Reflection

Reflection or specular reflection is the change in direction of an impinging ray at an interface (assumed perfectly smooth) between two different media, hence the ray returns into the medium from which it originated. For example, mirror exhibits specular reflection. The law of reflection states that the angle at which the wave is incident on the surface equals the angle at which it is reflected. It can be written as,

$$\theta_1 = \theta_1', \tag{3.1}$$

where θ_1 is the incidence angle and θ_1' is the reflection angle.

Diffuse Reflection

Contrary to assumption of perfectly smooth surface for specular reflection, energy of an incident ray spreads in multiple directions if the surface is rough [63]. However, relativity of surface smoothness or roughness depends on frequency of the impinging ray. It leads to define a criterion that a surface can be considered smooth if its generated scattered waves have very small phase difference between each other [64]. It can be expressed by the Rayleigh criterion for a rough surface,

$$\Delta h = \frac{\lambda}{8\cos\theta_1}, \tag{3.2}$$

where Δh is the height of the roughness that creates the phase difference. The relationship also shows that scattering diffuseness depends on the incident angle θ_1.

Refraction

Refraction is the change in direction of a ray due to change of the transmission media. It is described by Snell's law, which provides the relationship between angles of incidence and refraction for a ray impinging on an interface between two media with different refraction indices n. It can be formulated as,

$$\frac{\sin\theta_1}{\sin\theta_2} = \frac{n_2}{n_1}, \tag{3.3}$$

where θ_1 is the incidence angle and θ_2 is the refraction angle and n_1 and n_2 are the refractions indices of two media.

Diffraction

Diffraction is the apparent bending of rays around small obstacles (i.e., edges, curved surfaces and vertices etc), thus generating diffracted rays. The diffracted rays leads to derivation of different laws of diffraction, namely law of edge diffraction, law of surface diffraction and law of vertex diffraction. The diffraction effects are mostly prominent for rays having wavelength closer to dimensions of the diffracting objects. If the obstructing object contains multiple regions (closely spaced), it results in a complex pattern of varying intensity due to the superposition.

3.1.2 Diffuse Scattering Model

In general, classical RT tools take into account LOS propagation and specular reflection, sometimes also diffraction as illustrated in Fig. 3.2, but they do not account for diffuse scattering paths [44, 45, 65, 66]. Yet, the diffuse scattered power may represent a significant part of the received power, especially in NLOS conditions [67, 68]. Therefore, it is important to account for the diffuse power, which classical tools invariably overestimate. Generally, the percentage of diffused scattered power is high in NLOS conditions [8]. Hence, a diffuse scattering model [69] is described here which is incorporated in the pre-existent RT algorithm [8, 70, 71].

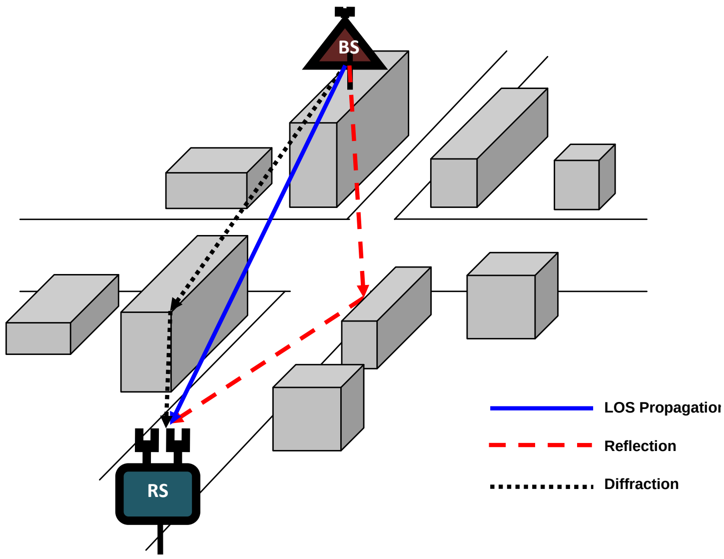

Figure 3.2: An example of the RT model, including three interactions: LOS propagation, reflection and diffraction

The diffuse scattering model allows to account for macroscopic roughness effects, such as windows, balconies, irregular bricks and surface roughness, etc., which also arise in non-specular directions. The model is based on dividing large surfaces into elementary surface elements, which act as scatterers. The size of each surface element is selected by far-field condition [72],

$$r > \frac{2D^2}{\lambda}, \tag{3.4}$$

where r is the distance between center of the element and the terminal and D is the dimension of the surface element.

The diffuse scattering rays are supposed to originate from center of each surface element incoherently. While different pattern models estimate the scattered field, the power of the diffuse field P_S is modeled by a directive pattern model [69] expressed as,

$$P_S = P_{S0}\left(\frac{1+\cos\phi_r}{2}\right)^{\alpha_r}, \tag{3.5}$$

where ϕ_r is the angle between the specular reflection direction and the scattering direction and α_r is a parameter which sets the width of the scattering lobe (the higher α_r, the narrower the lobe).

3.1.3 UCL Enhanced Ray-Tracing Tool

As mentioned previously, the 3-D RT tool used in this thesis is an enhanced version of previous one that was only taking into account LOS propagation, specular reflection and diffraction [44]. The new version improved the prediction capabilities of the pre-existent tool by implementing diffuse scattering [8, 70, 71].

The geometry of RT tool is based on a Cartesian coordinate system where rectangular parallelepipeds are employed as basic elements to create the simulation environment. They can represent a building in outdoor scenario or a 3-D wall in indoor scenario [8]. The input parameters of the tool are following [8],

- frequency,
- position of transmit and receive antenna in space,
- 3-D radiation patterns of transmit and receive antennas,
- 3-D coordinates of building blocks in the propagation environment,
- permittivity and conductivity values of materials in the environment,
- parameters for different propagation mechanisms, e.g., reflection, scattering coefficients etc.

The input database of RT tool describing the propagation environment is crucial. It is important to mention that a large number of objects in a real environment increase the computation time significantly. The ability of this tool to account for 3-D antenna patterns of Tx and Rx antennas, including the polarization aspects, makes it a suitable choice to analyse impact of the antenna beamwidth on the system performance. The improved RT predictions with diffuse scattering provides a much better coverage and interference model, which has a direct impact on the achievable capacity density and deployment guidelines.

3.1.4 Ray-Tracing Tool Validation

The validation of RT tool is crucial as it tells us the prediction accuracy by comparing simulation results with real measurements. Therefore, RT tool is experimentally validated through an outdoor measurement campaign with linear arrays of four dual-polarized ±45° slanted polarizations antennas [8, 70]. The difference between simulated predictions and measurements can be computed in terms of errors. In this context, it is important to first define the error computation procedure.

For N points, M_i are measurement values and S_i are their corresponding simulated values. The most common is the simple mean error between the measured (real) and simulated values with its sign. It can be evaluated as [8],

$$e_{me} = \frac{\sum_{i=1}^{N} (M_i - S_i)}{N}. \tag{3.6}$$

The standard deviation of error e can be defined as [8],

$$\sigma = \frac{\sum_{i=1}^{N} (e_i - \bar{e})}{N}, \tag{3.7}$$

where $\bar{e}$ is the mean error. The reference measurement campaign is conducted in campus area [8] where the Tx is placed at the fourth floor of a building and the Rx is moved to 15 different locations in the street. The Rx locations are mix of LOS and NLOS propagation conditions with respect to the Tx. For this validation work, a maximum of three reflections are used along with single bounce scattering. In addition, a directive model with parameters $S = 0.4$ and $\alpha_r = 2$ is utilized to minimize the prediction error [8, 70]. Different diffuse scattering parameters are investigated and simulation results are subsequently compared with measurements in terms of the received power. Table 3.1 mentions values of mean prediction error and standard deviation for the received power [8, 70]. A significant improvement in the received power is observed after including the diffuse scattering components. Consequently, the prediction error decreases from 10.1 dB to 4.4 dB [8].

	Mean error	**Standard deviation**
Received power [dB]	4.4	4.6

Table 3.1: Computed mean prediction error for the received power in an outdoor environment

3.1.5 State of the Art Ray-Tracing

RT is useful for site-specific channel modeling when a geographical database of significant scatterers in an urban environment is available and optimum placement of a BS antenna is desired. It is probably the most common deterministic simulation tool, designed in various versions ranging from simpler two dimensional (2-D) to comprehensive three dimensional (3-D) while accounting only simple propagation mechanisms or adding complex ones as well. It is more precise than simple empirical models, yet it is less complex than electromagnetic full-wave methods (e.g., 3-D electromagnetic simulator EMX). In this section, an overview of state of the art RT tools available in the literature and their applicability is presented.

The intrinsic characteristics of an RT algorithm give this tool a high degree of flexibility in the application scenarios. 2-D RT tools are the simplest ones [73], where propagation is assumed to take place only in a single plane, either the azimuth or the elevation plane. It is normally sufficient for a rough approximation of channel characteristics. However, a combination of horizontal and vertical rays is used to produce 3-D paths. The full 3-D RT tools are most commonly used to describe propagation in the whole investigated environment. In such tools, 3-D radiation patterns of antennas are employed to generate possible interactions in 3-D space. RT algorithms implement different types of interactions, where the basic element to describe the environment is critical. Generally, RT tools utilize a perpendicular parallelepiped as a basic element to represent a building in outdoor scenario or a 3-D wall in indoor scenario [8]. Indoor specific tools implement penetration or walls transmission, while vegetation scattering is also implemented in [74]. Currently, RT tools are being applied in various outdoor [46,65,75–78], indoor [45,73,79–82], and even vehicular environments [83,84]. Moreover, they are also in use for prospective application areas, e.g., ultra-wideband communications and THz communications.

An overview of results types found in the literature is briefly presented. The 3-D RT algorithms provide various wireless channel properties, e.g., narrowband, wideband, electromagnetic, static and mobile etc. Nearly all RT tools offer received power or pathloss predictions as a common base. Therefore, accuracy of RT tool in predicting such quantities is fairly established. For narrowband channels, the polarization behaviour of the channel is, however, relatively less explored through RT. The importance of implementing diffuse scattering in order to appropriately predict the polarization behaviour of the channel is proven in [85] for an outdoor scenario and validated in [75]. To characterize wideband channels, RMS delay spread is often estimated through RT in outdoor [46, 77] and indoor [45, 79] scenarios. In general, RT is less accurate in prediction of this metric. It is mainly due to limited number of interactions implemented in simulations in order to have reasonable computation time as well as manageable simulated area. Therefore, the extracted delay spread values by RT tools are often underestimated compared with validation measurements. A 3-D algorithm easily determine angular characteristics of the channel, however validation of such characteristics with measurements is not a straight forward task. Usually ad-hoc measurement campaigns and high resolution algorithms are required to extract channel's directional properties [76,77,86]. In addition, RT tools are widely being used to estimate the performance metrics of wireless networks. For example, a good agreement is found between Bit Error Rate (BER) values computed through simulations and measurements [82] and capacity of MIMO systems is estimated in [73].

3.2 Channel Sounding

The measurement technique used to estimate the propagation channel properties is called channel sounding. The name stems from a transmitter that "sounds" (or excites) the channel, whereas the receiver records the channel output. The complexity of the channel sounders increases according to their applications and measured scenarios. On the one side, multiple antenna systems require directional channel properties while wideband wireless systems necessitate delay dispersion measurements of the channel. On the other side, applications of channel sounding have grown from traditional macrocell scenarios to more complicated scenarios such as indoor, industrial (metallic objects) and inter-vehicular environments.

All channel models rely on measurements of the wireless propagation channel where parameters of stochastic channel models are extracted from the measured data. In particular, RT models need to be validated with measurements in a real environment. The wireless propagation channel can be measured in the time or frequency domain. In time-domain measurements, the channel impulse response $h(t, \tau)$ is obtained by exciting the channel with pulses or Pseudo-Noise (PN) sequences generated deterministically. The PN sequence normally has a good time-bandwidth product and each element is named as chip. On the other hand, frequency domain measurements acquire the transfer function $H(t, f)$ by using a chirp signal (frequency increase or decrease with time) or a multi-tone signal (flat spectrum and low peak-average ratios) to sound the channel.

The synchronization between Tx and Rx units is critical in sounding techniques. Frequency offset between local oscillators of two units can cause phase rotation which results in shift of the IR delay. To overcome this issue, one way is to connect two units with coaxial or fiber-optic cables to send a synchronization signal. However, it is only possible for short range measurements, e.g., indoor scenario. Therefore, for long range measurements, atomic clocks are usually employed in the sounding equipment to keep them synchronized. The synchronization of both units can be done at beginning of the measurement campaign.

The band-limited time-invariant measurements can be performed by sampling channel at Nyquist rate such that:

- The period, T_{rep}, with which the periodic pulses are sent by the Tx unit repeatedly, must be shorter than the coherence time of the channel
$$T_{rep} \leq \frac{1}{2\nu_{max}}, \tag{3.8}$$
where ν_{max} is the maximum Doppler frequency.

- T_{rep} should be greater than the maximum excess delay of the channel in order to avoid overlap between consecutive sounding signals,
$$T_{rep} \geq \tau_{max}. \tag{3.9}$$

These two conditions jointly give the equation for the two-dimensional Nyquist criterion,
$$2\nu_{max}\tau_{max} \leq 1. \tag{3.10}$$

If this criterion is satisfied, the channel under investigation is said to be underspread.

Similarly, some specific conditions needs to be fulfilled for MIMO channels measurements. The channel responses for all possible combinations of Tx and Rx antenna elements have to be measured in MIMO channels. For this purpose, following three techniques can be applied.

- Real arrays: each array has its own RF chain, the channel can be measured simultaneously at different receiver elements. However, this costly approach requires a complex calibration procedure.

- Switched arrays: only requires one RF chain at the Rx [87]. Fast RF switches control the switching between different Tx and Rx elements, such that only one antenna pair is measured at a time.

- Virtual arrays: a single antenna at each side of the link, MIMO measurements can be performed by mechanically moving the antenna to predetermined positions.

3.2.1 Multi-Link Channel Sounding

In addition to suitable antenna arrays and conditions for time-variant MIMO channels, innovative techniques are required to extend the inherently single-link capability of classical channel sounders for measurements of multi-link propagation channels. Three commonly used techniques to measure multiple links are described here.

Single-sounder sequential

In single-sounder sequential (or virtual measurements) technique, a single sounder (SISO or MIMO) is used to measure the multi-user channel in a sequential manner [88, 89]. The obvious benefit of this technique is that already existing measurement equipment can be used. However, this technique bears mainly two drawbacks. First, the environment may change during the measurement runs [41]. Second, the sounder calibration may change, as clocks tend to drift over the measurement time. Hence, even if the environment is kept constant, phase-synchronized multi-user measurements are impossible. Nevertheless, this is a cheap and possibly accurate technique in controlled environments [29].

Single-sounder multi-node

The single-sounder multi-node (or distributed measurements) technique also relies on a single MIMO sounder, connected to distributed nodes by means of long RF cables [41, 90]. While this guarantees the phase synchronization (up to the sounder phase stability), the measurement range is limited owing to the length of cables (i.e., indoor or outdoor-to-indoor scenarios). Note that in mobile scenarios, cable movements may introduce phase jitter. Optical fibres can be used as alternatives for longer distances. This technique has two disadvantages: it is expensive, and its calibration procedure is cumbersome (as the calibration must be carried out for every cable separately, because of RF/optical transducers) [29].

Multi-sounder

The multi-sounder (or real-time measurements) technique use multiple MIMO channel sounders to measure multiple MIMO links simultaneously. It is possibly the best solution being closest to a real-world scenario [91]. Typically, such measurement architecture involves a single Tx with multiple receivers. However, multi-transmitter linked to single Rx is also possible with accurate synchronization. The main challenge for this technique is to operate two compatible channel sounders and to maintain the synchronization of multiple clocks. Since channel sounder are very expensive, therefore utilizing multiple sounders is not feasible in practice. So far only one study using two channel sounders for real time measurements has been reported in [91]. Hence, simplified measurement techniques are preferred in real-time measurements.

In the next section, technical details of the channel sounder used in outdoor measurement campaigns conducted for this thesis is presented.

3.2.2 The Elektrobit Channel Sounder

The Elektrobit channel sounder is a radio channel measurement system operated at a carrier frequency range of 3.4 to 4.2 GHz and based on the switched array principle [92]. It mainly consists of two units, a Tx unit and a Rx unit, as shown in Fig. 3.3. The Rx unit is further connected to the Data Acquisition (DAQ) module. Real Time Control Software (RTCS) is a remote user control, allowing the user to change setting at the Tx or Rx unit. It is accessed through a control notebook connected to each unit with a Local Area Network (LAN) cable.

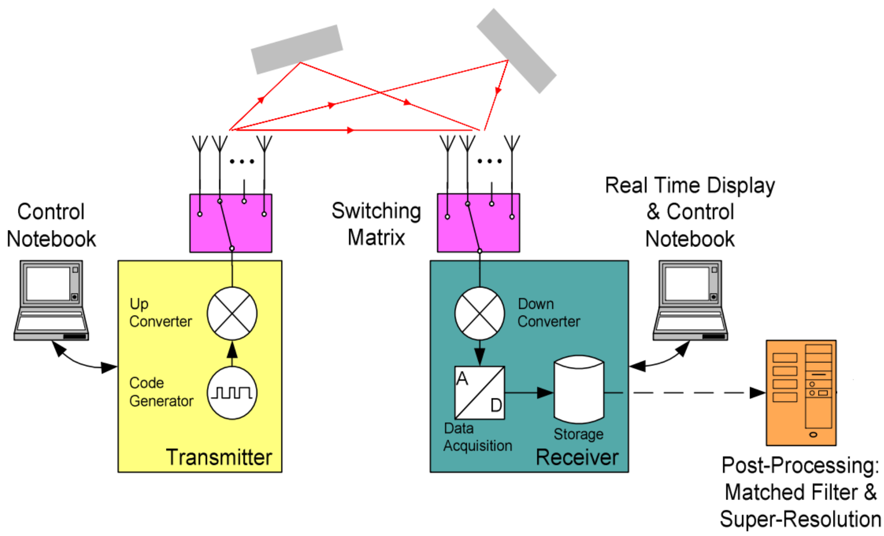

Figure 3.3: Block diagram of the Elektrobit channel sounder [92]

The Elektrobit channel sounder transmits and receives a PN sequence to determine the channel IR. A PN sequence generated at the Tx side is modulated and up-converted to the desired center frequency. Conversely, the received signal is down-converted at the Rx side and demodulated into I/Q format. An important concept of the channel sounder is the timing, where a chip is basic unit represents one symbol of a code. The chip rate controls the timing such that higher chip rate achieves better delay resolution of the IR. The delay resolution (τ_r) can be expressed as,

$$\tau_r = \frac{1}{f_{ch} \times N_{sc}}, \tag{3.11}$$

where N_{sc} is the number of samples per chip and $f_{ch} = B/2$ (B is the bandwidth). Several chips construct a transmission code that must be longer than the maximum measurable delay in the propagation scenario but shorter than the Doppler period (i.e., the time for which the channel can be considered static). Long codes provide processing gain, thus improving the dynamic range. The measurable excess delay (τ_e) is,

$$\tau_e = \frac{N_{ch}}{f_{ch}}, \tag{3.12}$$

where N_{ch} is the code length in chips. Each Tx antenna transmits a number of codes equal to the receive antennas and a guard code re-

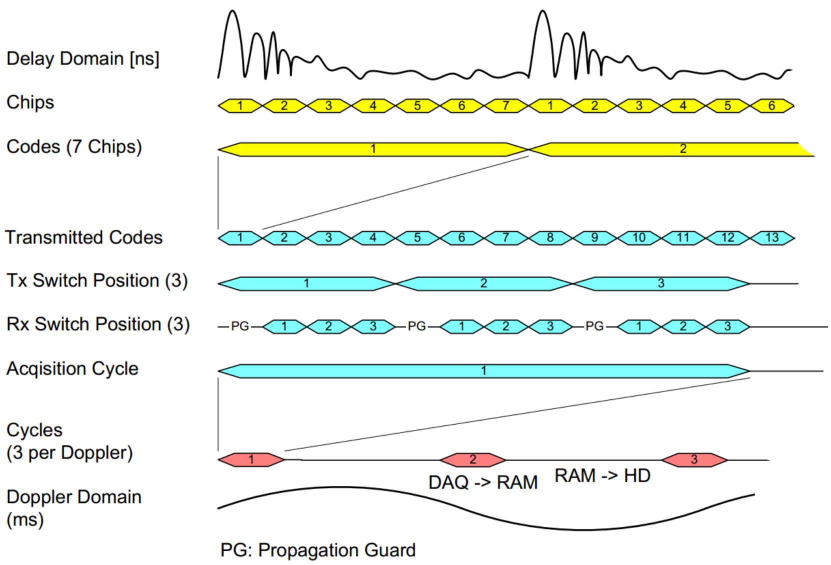

Figure 3.4: Timing concepts of the Elektrobit channel sounder [92]

quired for moving the Tx switch to the next antenna, thus total number of codes for each acquisition cycle are $N_{co} = N_{TX}(N_{RX} + 1)$. This switching principle is illustrated in Fig. 3.4. The fast switches of each unit, connected to multiple antennas, enable the channel sounder for MIMO measurements. Once all the Tx and Rx antennas are scanned, the acquisition cycle is accomplished.

In addition, Doppler frequency of the time-variant channel has to be sampled according to Nyquist criterion, therefore, the minimum channel sampling rate is expressed as,

$$f_{cs} = \frac{v_m + 2v_s}{\lambda} N_\lambda, \tag{3.13}$$

where v_m is the maximum speed of the mobile terminal, v_s is the maximum speed of the scatterers and N_λ is the number of wished channels per wavelength. In a high Doppler frequency scenario, the cycles can be measured in bursts mode. In this mode, where cycles are measured for a certain time, and then data is stored on the disk for rest of the time, without taking measurements.

The synchronization of local oscillators at the Tx and Rx employing Rubidium clocks is critical in measurement campaigns, especially when both units have to be separated. A small frequency offset can lead to phase rotation (Doppler) and sliding of the delay. The sounder can be synchronized in the following two steps,

- the clock synchronization, where the relative phase rotation is minimized by tuning the Rubidium clocks,

- the time tag synchronization, where a common absolute time reference is allocated to both units.

A calibration measurement before the data acquisition is essential in order to compensate the system and cable losses. Actually, it is measurement of a well-defined channel, usually an attenuator of a certain attenuation which is back-to-back connected to both units through RF cables. After successful synchronization and calibration measurement, two units can be moved without external power supply after putting on Clock Keep Alive (CKA) mode. Inputs parameters or sounder settings can be adjusted with the help of “Setup Wizard” in the controlling notebook. An example screen-shot of wizard is shown in Fig. 3.5. The range of input parameters to be defined before measurements is provided in Table 3.2. While different methods can be used to identify measurement locations, the Elektrobit channel sounder has capability to store the location of the Rx by Global Positioning System (GPS) together with the measured data stream (time-tagged), when GPS coverage is available.

Parameters	**Range**
Carrier frequency	3.4 to 4.2 GHz
Bandwidth	1.563 to 200 MHz
Transmit power	23 dBm (default value)
No of samples per chip	1 to 10
Max. path length	min. code length in chips
Channel sampling rate	0.011 to 1358.911 Hz
Max. mobile speed	min. channel sample rate
Tx antennas	1 to 8
Rx antennas	1 to 8

Table 3.2: The range of channel sounder parameters to be defined before a measurement campaign

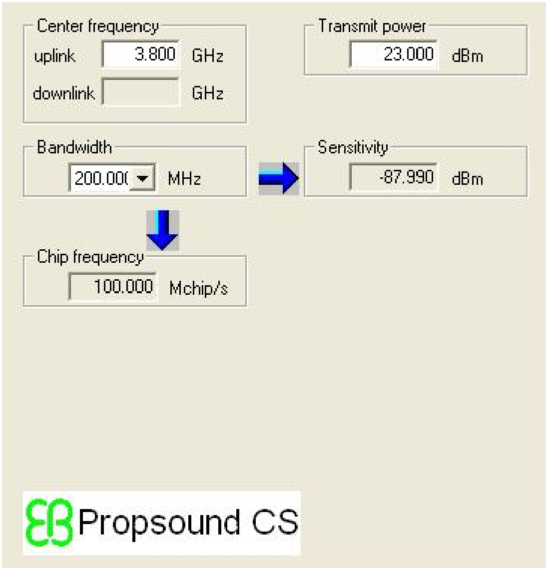

Figure 3.5: Screen-shot of setup wizard used in the Elektrobit channel sounder [92]

3.3 Conclusions

This chapter has presented simulation and measurement tools to characterize the wireless propagation channels in this thesis. First, the basic physics of the RT approach has been illustrated and followed with a brief description of the diffuse scattering model which has been implemented in the enhanced RT tool. In addition, validation of the RT tool in terms of received power has been included. Second, channel sounding approach has been detailed, in particular emphasizing on multi-link channel sounding techniques. Various techniques have been described to extend the inherently single-link capability of classical channel sounders to multi-link propagation channels. Both approaches have advantages and disadvantages, RT approach requires details of the scenario (i.e., building layout and material) under investigation as a necessary input database, while realistic measurements not only require expensive equipment but also cumbersome planning, physical efforts and extensive data post-processing. Finally, important characteristics and parameters of the Elektrobit channel sounder have been presented.

CHAPTER 4

Multi-Beam Base Station Architecture: Channel Models and Array Optimization

LTE-advanced and beyond 4G wireless networks promise the provision of ultra high capacity and unprecedented data rates. For example, LTE-Advanced promises peak data rates of 1 Gbps for the downlink and 500 Mbps for the uplink [2,93]. Apart from peak data rates, it is crucial that beyond 4G networks are able to provide high capacity density as well, i.e., to provide the average data rate to all active users simultaneously within a geographical area. Under 3GPP specifications, in a typical urban scenario the inter-BS distance is 500 m, which results in about 4 BSs/km^2 [93]. The average cell spectral efficiency for the LTE-Advanced downlink is 2.2 bps/Hz (2$\times$2 MIMO case), which for a typical bandwidth allocation of 40 MHz results in $4 \times 2.2 \times 40 = 352$ Mbps/km^2. This is not sufficient to meet future demands of the capacity density specially in ultra dense urban environments which are estimated to surpass 1 Gbps/km^2 [7, 94].

One promising solution to meet such requirement is to rely on multi-beam antennas deployed with dense topologies in relay-assisted networks. For example, in the BuNGee project [7] this technique is used to provide wireless backhaul to a large number of fixed RSs, which then serve multiple mobile terminals (i.e., users). This technique can potentially improve network performance as it greatly increases the antenna gain from the BS. Note that fixed relays are not likely to be located at the boresight of beams due to practical constraints of the BS architecture [7, 95]. For the multi-beam BS antenna architecture, multiple fixed narrow beams are created (using a fixed beamforming approach) with the aid of an antenna array fed by a Butler Matrix (BM) [96]. The BS architecture with high gain narrow beams allows the spatial reuse of spectrum thus increasing the spectral efficiency. The BS is connected to the operator backhaul on one side and distributed RSs on the other side as illustrated earlier in Fig. 1.7. However, performance evaluation of any wireless architecture heavily depends on the underlying wireless propagation channel. Channel models are useful to evaluate the capacity of the network and estimate the achievable data rates. This becomes more important for the architecture relying on aggressive frequency reuse (and thus heavy temporal and spectral interference), and dense deployment scenarios (thus unseen spatial signal and interference propagation characteristics). Therefore in this chapter, we focus on two important wireless propagation channel aspects regarding multi-beam BS architecture:

- **Channel Models:** the specificities of the multi-beam antenna and its impact on the BS-to-RS propagation link are characterized. Whilst a large amount of channel models, e.g., 3GPP, WINNER II and COST 2100 (detailed earlier in Chapter 2), are available to describe such channel, they require some significant modifications to reflect peculiarities of the innovative architecture, in particular multi-beam antenna specifications (i.e., narrow beamwidth).

- **Array Optimization:** a large number of narrow-beams cause co-channel interference thus limiting the achievable high data rates. In addition, inter-cell interference also bounds the high capacity density. Therefore, interference needs to be characterized in order to provide high capacity density in beyond 4G wireless networks. To effectively reduce interference in the multi-beam antenna architecture, the array optimization technique (i.e., amplitude tapering employed to reduce side-lobe levels of narrow beams in the BS antenna) is exploited.

Lastly, performance of interference bound backhaul links is analyzed through system level simulations. Furthermore, impact of the array optimization technique on overall capacity density and quality of service (delay and probability of retry) is evaluated. It is important to mention that due to numerous practical constraints imposed by the BuNGee project [7,95] (e.g., innovative fixed BS architecture, square-cell deployment topology and specific frequency planning etc), wireless channel characterization and modeling work in this chapter is based on RT simulations.

4.1 Multi-Beam Base Station

The provision of high capacity can be achieved by enabling the BS to generate a large number of high gain narrow-beams. Therefore, the innovative multi-beam antennas are deployed at the BS in an architecture comprising $4 \times 90^{\circ}$ sectors, each sector is capable of providing six separate beams in two slanted $\pm 45^{\circ}$ polarizations [97]. The dual-polarization is used to optimize the isolation between adjacent antennas in the array. At 3.5 GHz frequency, the dimensions of the array antennas are approximately 450 mm (width)$\times$500 mm (length)$\times$50 mm (depth), excluding the beam-forming matrix as shown by a single sector (six beams) antenna in Fig. 4.1.

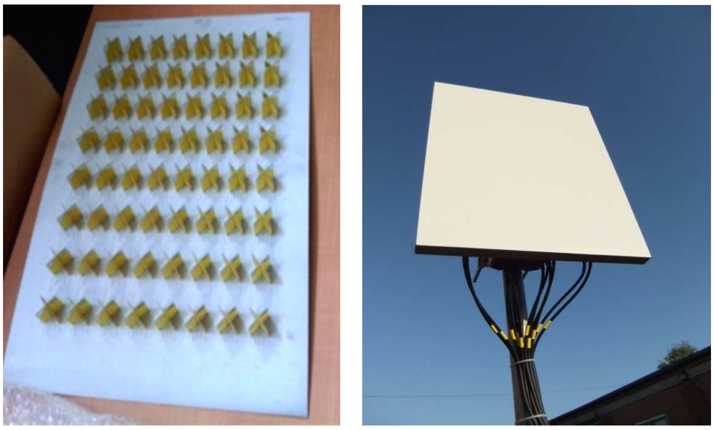

Figure 4.1: Multi-beam BS antenna, (left): front view of a single 90° sector, (right): fully housed antenna showing interconnections to the MIMO equipment

4.1.1 The Beam-forming Network

A beam-forming network connected to the 8-element antenna array produces a unique combination of six high gain narrow beams across a 90° sector in azimuth [97]. The beams can be steered in azimuth with six 15° increments by using appropriate phase-matched cables. The handover between beams occurs at half-power points thus providing continuity of coverage across the complete 90° sector of each antenna [97]. A bespoke Butler Matrix (BM) is used in conjunction with 450 mm long phase matched cables to each of antenna input ports [97]. A BM is a passive external circuit operating at microwave frequencies having N ports feeding/receiving signals to/from the antennas and N_B ports feeding/receiving signals to/from the RF chains. A BM consisting of phase shifters, quadrature hybrids and couplers, essentially implements a passive fixed RF beam-former creating N_B narrow beams, where $N_B \leq N$. Two BMs are used in each antenna, one for each polarisation, connected to antenna input ports with phase matched cables. A schematic of a typical beam-forming network illustrating 90° branch line couplers and interconnections with phase shift in each combination of connections is shown in Fig. 4.2 [97]. Only six out of eight inputs are used for the BS antenna, the remaining two inputs being terminated.

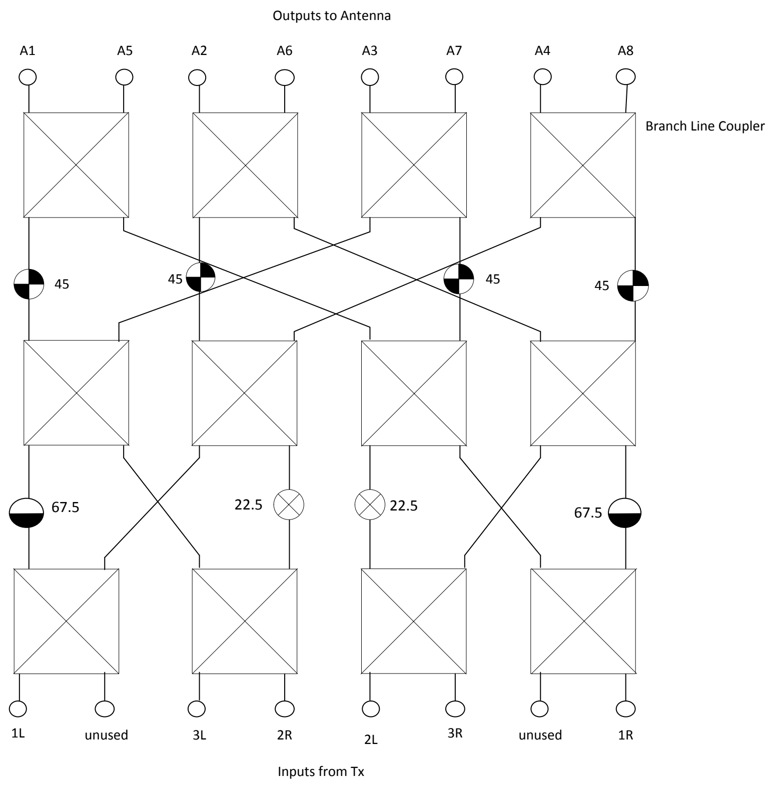

Figure 4.2: The schematic diagram of a typical beam-forming network

4.1.2 Radiation Pattern

An example beam pattern (azimuth) of the multi-beam BS antenna is shown in Fig. 4.3. Each beam has an approximate half-power beamwidth of 15° in azimuth. Azimuthal side-lobes level is approximately −14 dB and the approximate peak gain is 19 dBi. Gain and side-lobes level are a function of pointing angle and varies across the 90° sector. The elevation beamwidth of all antenna beams in the array is approximately 10° with 2° electrical down-tilt [97]

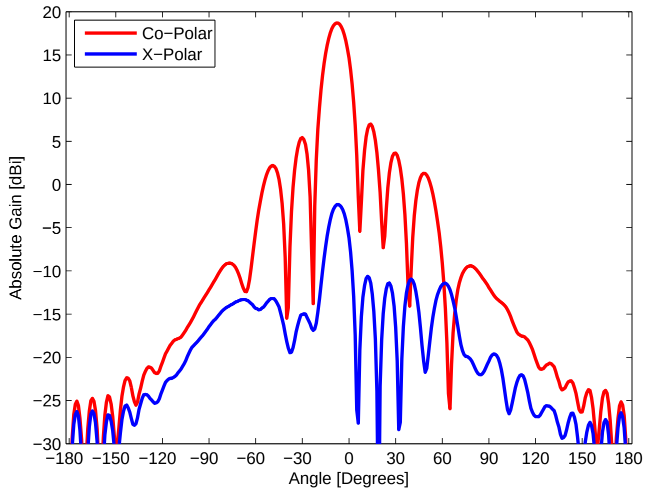

Figure 4.3: An example beam pattern (azimuth) of multi-beam BS antenna

4.1.3 Relay Station Antenna

On the receive (RS) side, dual-polarized directional antenna is used with 13 dBi gain at the height of 5 m (below roof top) from the ground level. The directional receive antenna has 40° beamwidth both in azimuth and elevation, and it has very low side-lobes that are especially suitable for slanted ±45° polarizations.. A typical radiation pattern (azimuth) of one port shows 20 dB side-lobe level below the peak gain, as demonstrated in Fig. 4.4. At 3.5 GHz frequency, the approximate sizes of RS antennas are 160 mm × 160 mm × 25 mm. Both BS and RS antennas are specifically designed and developed by Cobham Antennas within the framework of the BuNGee project [97].

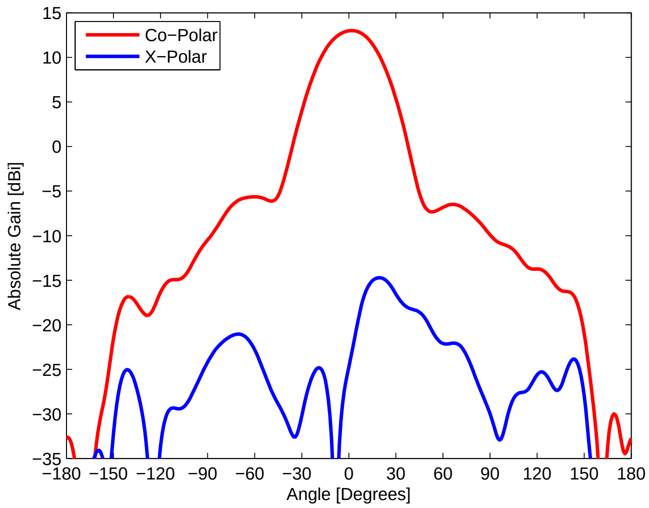

Figure 4.4: An example azimuth beam pattern of RS antenna

4.1.4 Minimum Safe Distance Calculations

The minimum safe distance can be calculated by using the Friis formula recommended by Federal Communications Commission (FCC) [95],

$$S = \frac{PG}{4\pi d^2}, \tag{4.1}$$

where S is Power Flux Density (PFD) in W/m^2, P is the input power to antenna in W, G is the liner gain of the antenna and d is the distance to radiation centre of the antenna in m. For antennas operating at 3.5 GHz with a nominal 18 dBi gain and input power of 38 dBm (or 6.3 W) as considered in the BuNGee project [95], substituting PFD values (exposure limit for Poland = 0.1 W/m^2) gives us a minimum safety distance of 16 m from boresight of the antenna [95]. In addition, a brief analysis of street geometries presented in [95] have shown that for an appropriately mounted (2 m away from the building wall) and aligned antenna of approximately 18 dBi gain with either normal (13 dB) or suppressed (19 dB) side-lobes level, a person at street level or in adjacent buildings is unlikely to experience a PFD greater than the Polish exposure limit of 0.1 W/m^2 [95].

4.1.5 Deployment Scenario - Square Topology

The deployment scenario assumes a square-cell topology in a typical urban propagation environment at 3.5 GHz [7]. This topology is valid for several European cities like Barcelona. The square-cell topology consists of a centrally located BS (above roof-top at a height of 25 m from the ground level) equipped with N_B beams and and M number of RSs in a cell. The square-cell topology has a block raster of 90 m with each block of width 75 m and street width is taken as 15 m, while the block height is fixed to 20 m. A BS cell is 450 m in each dimension which makes an approximate area 0.20 km^2. In Fig. 4.5, the block diagram explains the details of the scenario, where only $N_B/2$ beams (12 out of 24 in total) are utilized for the sake of brevity. Black dots represent RS locations at street intersections, and small arrows indicate the direction of RS antennas along the axis of streets. Both BS antenna beams and RSs are numbered in anti-clockwise fashion. The distance between BS and RS antennas varies depending upon the RS location. Note that antenna beams are not directed to specific RS locations because beam geometry of the antenna is fixed, hence any given RS is unlikely to be located on the boresight of any beam. In other words, the number of RSs served by each beam can vary according to the specific geometry, e.g., a beam along a street or a diagonal is likely to include more RSs.

4.1.6 Simulation Parameters

In RT simulations, full 3-D antenna patterns are employed at both Tx and Rx sides. In the simulation scenario, building blocks are considered of concrete. The relative permittivity and conductivity of concrete walls at 3.5 GHz are taken as 4.85 and 0.173 S/m respectively, with a maximum number of reflections equal to 3 (note that increasing this order to larger values does not modify the received power) [8, 70]. The utilized simulation parameters are summarized in Table 4.1.

Parameters	**Value**
Carrier frequency	3.5 GHz
Concrete, ε_r	4.85
Concrete, κ	0.173 S/m
No. of reflections	3

Table 4.1: RT simulation parameters

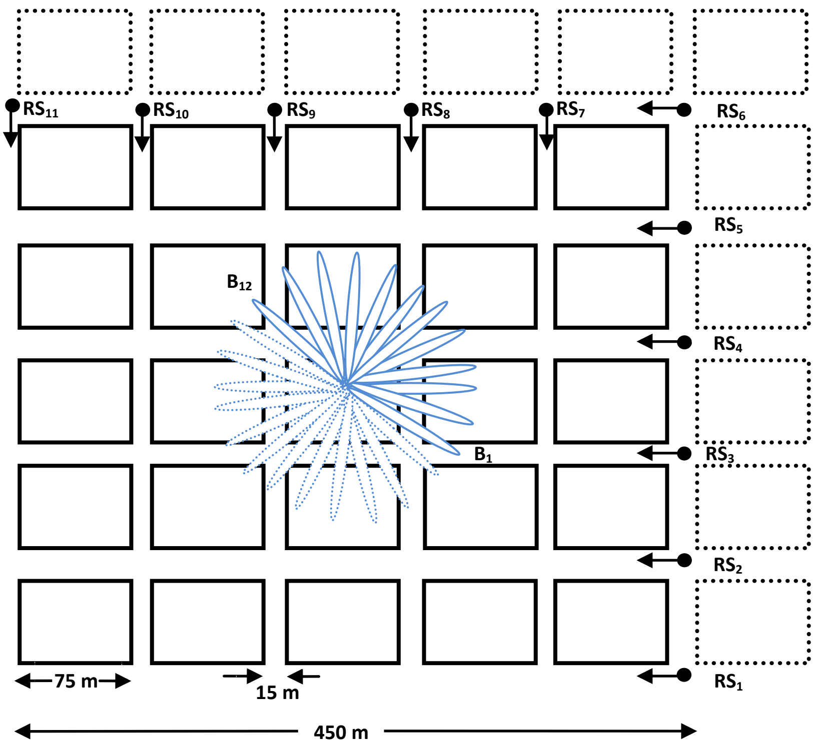

Figure 4.5: A typical urban grid scenario with a square-cell topology

4.2 Pathloss Characterization for BS-to-RS Link

Whilst a large amount of pathloss models, e.g., IEEE 802.16, 3GPP and WINNER II, are available, they require some significant modifications to reflect peculiarities of the multi-beam BS architecture, in particular impact of narrow-beams. Therefore, pathloss models for the BS-to-RS propagation link are investigated by the RT tool in this section and simultaneously compared with the potential of WINNER II channel models. To determine pathloss, the received power at the Rx is calculated by using following expressions,

$$P_{\text{coh}} = |\sum_{\text{coh}} \alpha_l|^2, \tag{4.2}$$

$$P_{\text{ncoh}} = \sum_{\text{ncoh}} |\beta_k|^2, \tag{4.3}$$

where P_{coh} is the coherent power obtained from specular MPCs, P_{ncoh} is the part of power received from dense MPCs (diffuse scattering), α_l and β_k are the complex amplitudes of contributing rays for coherent and non-coherent power respectively. Generally, implementation of the diffuse scattering improves accuracy of the prediction. The total received power (P_{Rx}) in dB is the sum of coherent and non-coherent received powers,

$$P_{\text{Rx}} = P_{\text{coh}} + P_{\text{ncoh}}. \tag{4.4}$$

The received power (P_{Rx}) in dB is also predicted by the Friis law as a function of the distance d in free space [15],

$$P_{\text{Rx}} = P_{\text{Tx}} + G_{\text{Tx}} + G_{\text{Rx}} + 20 \log \left(\frac{\lambda}{4\pi d} \right), \tag{4.5}$$

where P_{Tx} is the Tx power (dB), G_{Tx} and G_{Rx} are gains (dB) of the Tx and the Rx antenna respectively, d is the distance between the Tx and the Rx and λ is the wavelength. The free space pathloss (PL) in dB when antenna gains are excluded is given by [15],

$$PL = P_{\text{Tx}} - P_{\text{Rx}} = -20 \log \left(\frac{\lambda}{4\pi d} \right). \tag{4.6}$$

Substituting (4.6) in (4.5) gives us [15],

$$PL = P_{\text{Tx}} + G_{\text{Tx}} + G_{\text{Rx}} - P_{\text{Rx}}. \tag{4.7}$$

Note that the Friis law is only valid for far field conditions when the Tx-to-Rx distance is at least one Rayleigh distance (also known as the Fraunhofer distance). The Rayleigh distance is defined as [15],

$$d_R = \frac{2L_a^2}{\lambda}, \tag{4.8}$$

where L_a is the largest dimension of the antenna. In addition, the far field requires $d \gg \lambda$ and $d \gg L_a$ [15].

4.2.1 Effective Pathloss

While pathloss is classically defined as the deterministic distance dependence of the received power for omnidirectional antennas [15], an effective pathloss (PL_e) is introduced which accounts for the pathloss increase caused by the use of narrow beam antennas. It can be written as,

$$PL_e = PL + \Delta PL, \tag{4.9}$$

where ΔPL is the increase in pathloss due to narrow beamwidth antenna. Simulation results are evaluated for BS-to-RS links in a defined square-cell topology. Some extra RS locations are considered in order to get better distance-dependent-pathloss statistics as depicted by hollow dots in Fig. 4.5. Note that BS narrow beams are not directed to specific relay locations because of the fixed BS architecture (a practical constraint). Therefore, RS antennas may lie outside the boresight of the beam thus causing higher pathloss. Results in Fig. 4.6 have revealed that pathloss at some locations (e.g., RS_3, RS_4 , RS_8, RS_9) is notably lower than other locations mainly due to the street canyon effect. The corner locations (e.g., RS_1, RS_6, RS_{11}) have comparatively higher pathloss due the larger distance and higher level of obstruction from the BS.

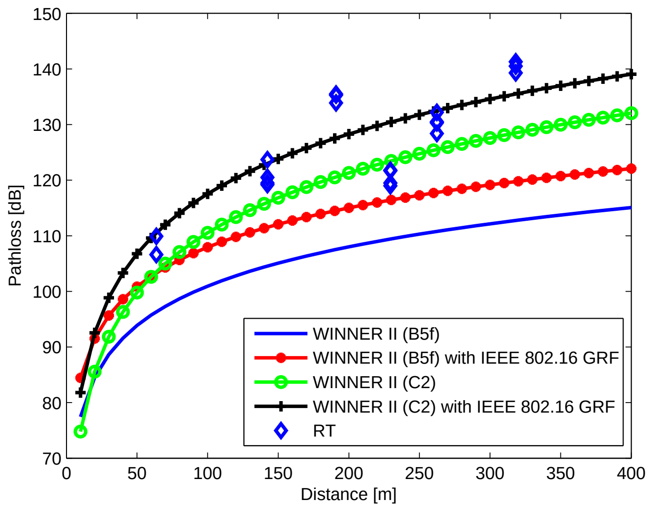

Figure 4.6: A comparison of RT simulations with the WINNER II channel model (with and without IEEE 802.16 GRF)

4.2.2 Comparison of RT and WINNER II Channel Model

As shown in Fig. 4.6, the pathloss exponent seems to be similar for both approaches, however, generally the WINNER II channel model yields lower pathloss compared to the RT. Although the higher difference of B5f compared to C2 might be due to fact that former is based on a non-grid environment, the main effect is the reduction of BS antenna beamwidth, which has been taken into account in the RT approach, but not in WINNER II. This illustrates that it is actually not correct to compare the effective pathloss derived from the RT with the WINNER II pathloss, as the latter does not consider the effect of the BS antenna (reduced antenna beamwidths) on the effective pathloss. It can also be observed that the C2 pathloss exponent (i.e., the slope of the curve) is higher than RT results generally. This is probably caused by the fact that in RT simulations, RSs are located higher than C2 mobile terminals. The C2 model is indeed not intended for relay links.

To tentatively provide a fair comparison with WINNER II models, those values are combined with a Gain Reduction Factor (GRF). The only available GRF model is provided by IEEE 802.16 model [47], which determines the ΔPL factor in the effective pathloss equation (4.9). Including the GRF, the analytic curves of B5f and C2 model come closer to RT results, as shown in Fig. 4.6. There could be a number of other reasons for discrepancies (assuming that the RT provides correct values [8, 70]):

- neither WINNER II (B5f) nor IEEE 802.16 models are based on a grid environment,
- 5Bf is based on RS located at 15 m, while in RT scenario RS is 5 m high and IEEE 802.16 assumes high BSs,
- in IEEE 802.16 GRF empirical formula is formulated with the directional antennas used at RS side; hence value should be adapted to BS side,
- lastly, the tested hybrid model has never been validated, and is made of two separate components.

4.2.3 Impact of BS Antenna Narrow-beams

The effective pathloss increases due to directivity of the antenna, as mentioned briefly in Section 2.3.3.1. In other words, the effective gain of

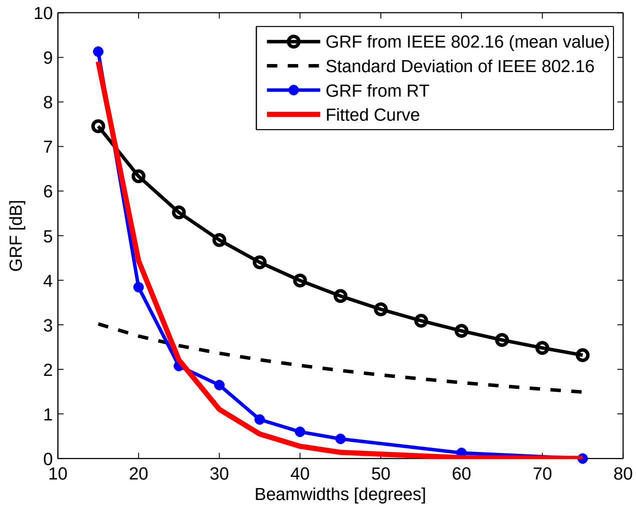

Figure 4.7: GRF [dB] curves from RT simulations and the IEEE 802.16 channel model

a directive antenna is less than the actual gain. This can be characterized by the quantity ΔPL, or equivalently by GRF [47] described earlier as a Gaussian distributed random quantity (dB value) with a mean and standard deviation in Section 2.2. GRF is an important parameter and it should be considered in the link budget of a specific receive antenna configuration. For this reason, it is re-estimated from the RT tool, by comparing results with omnidirectional antennas both at the BS and the RS. The so-obtained GRF curve is shown in Fig. 4.7. GRF (or ΔPL) values decrease with larger beamwidths, where higher GRF values correspond to higher pathloss. Note that for 15 degree beamwidth, the RT-based GRF is higher than the IEEE 802.16 model. The difference between the IEEE 802.16 model and the RT-based GRF curve can be explained by the fact that the former is not based on a grid environment. The RT-based GRF (for the given building height and street width) has been fitted by the following relationship,

$$\Delta PL[dB] = 72e^{-0.14\beta}, \tag{4.10}$$

where β is the beamwidth in degrees. The exponential decaying relationship is based on empirical results extracted through RT simulations.

4.2.4 Impact of BS Antenna and Building Heights

To analyse impact of the BS multi-beam antenna and building heights for the BS-to-RS fixed link, different heights are evaluated at selected RS locations in a square-cell topology. RSs are placed at the height of 5 m from the ground, whereas BS antennas are placed in two ways,

- fixed heights: $h_{BS} = 25$ m,
- variable heights: ($h_b + 5$ m) where building heights (h_b) are distributed between 10 to 24 m with a 2 m increment.

As shown in Fig. 4.8, increasing building heights generally corresponds to increase in the pathloss due to increased level of obstructions. Fixed BS heights have less pathloss values compared with variable BS heights, when building heights are smaller. However, they have higher pathloss values at larger building heights in comparison to variable BS heights. Further, it can be observed that increase in pathloss for for some RS locations (e.g., RS_2, RS_5 and RS_6) is large due to increased shadowing effect of buildings. On the contrary, there is less increment in pathloss values at RS_3 location (specially for variable building heights) as it experiences less obstruction due to the street canyon effect.The level of obstruction (or shadowing) also increases with the propagation distance which results in higher pathloss as it can be seen for RS_6 in Fig. 4.8. Note that RS_2 and RS_5 are placed at an equal distance from BS antenna, while RS_6 is the farthest placed in the considered scenario.

In addition, simulations are carried out to analyse the impact of different grid sizes (i.e., 75, 90, 110 and 130 m). The results have shown that pathloss generally increases with increase in the grid size. It is due to increased sizes of building blocks (i.e., concrete) taken in RT simulations.

4.3 Impact of BS on Polarized MIMO Characteristics

In this section, polarized MIMO characteristics of the BS-to-RS fixed relay link are investigated to reflect peculiarities of the multi-beam BS architecture. While the impact of directive patterns on MIMO characteristics could be predicted using WINNER II models, polarization aspects are yet to be added (as the WINNER II model is essentially

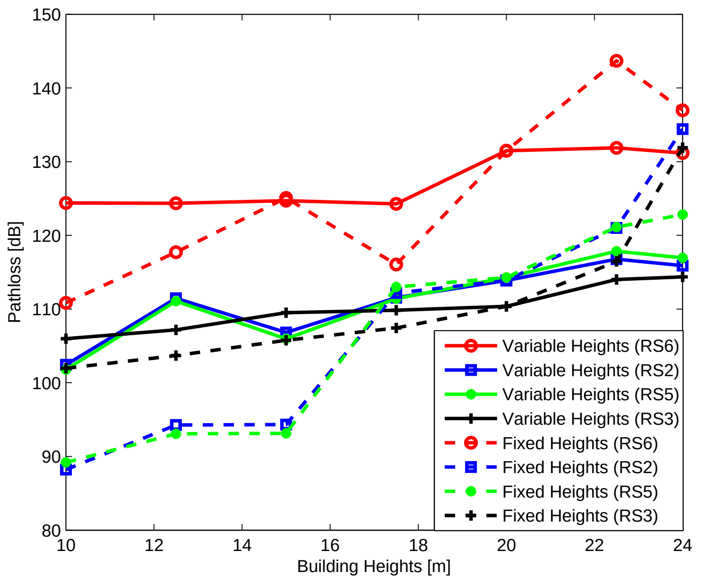

Figure 4.8: Impact of varying heights of the BS antenna and buildings on pathloss

two-dimensional). To combine polarization and narrow beamwidth aspects in a 3-D propagation environment, fixed relay polarimetric links in a square-cell topology are characterized. Subsequently, RT-based results are compared with relevant parameters of existing models.

4.3.1 Simulation Setup

The block diagram in Fig. 4.5 illustrates the simulation scenario. Only BS-to-RS$_4$, -RS$_6$ and -RS$_{10}$ links are simulated with three beams B$_4$, B$_7$, and B$_{12}$ respectively. The propagation distance between antennas varies depending upon the RS location. The distances of RS$_4$, RS$_6$ and RS$_{10}$ from the BS are 230, 318 and 262 m respectively. In order to characterize spatial and polarized MIMO statistics at each RS location, a total of 400 spatially separated simulations are performed over a 20×20 square grid. The spacing between these grid points is one wavelength (i.e., $\lambda = 8.56$ cm). The use of dual-polarized antennas at both sides (2×2) makes a total of 1600 simulations for each BS-to-RS link.

4.3.2 Spatial Fading

A spatial K-factor can be defined as the ratio of the coherent (fixed) to non-coherent (spatially fluctuating) power of MPCs, in order to characterize the severity of spatial fading. This parameter is important in fixed links, as it highlights how the channel gain may vary as a function of small displacements of the RS antenna [47]. It can be expressed as,

$$K = \frac{m^2}{2\sigma^2}, \tag{4.11}$$

where m^2 is the power of coherent components and $2\sigma^2$ is the power of non-coherent components. The estimated spatial K-factor values (dB) for polarized link range from 5 to 20 dB at three RS locations, as summarized in Table 4.2. K-factors at RS_4 are exceptionally higher compared with other locations due to higher street-canyon effect. In general, high K-factor values naturally result from the use of narrow-beamwidth BS and RS antennas. However, it can be observed that the K-factor generally decreases with the propagation distance.

Pol. at Tx/Rx	$\mathbf{RS_4}$	$\mathbf{RS_6}$	$\mathbf{RS_{10}}$
+45/+45	20.1	5.9	14.3
+45/−45	12.2	7.4	10.0
−45/+45	18.1	5.7	10.3
−45/−45	16.0	8.3	11.0

Table 4.2: Spatial K-factor values (in dB)

K-factor values decrease when increasing the antennas beamwidths as given in (2.28) by IEEE 802.16 fixed wireless channel model [47]. The relation implies that increasing antenna beamwidth from 15° to 90° reduces K-factor values by an approximate factor of 3, or equivalently by 4.8 dB [47].

In Fig. 4.9, the Cumulative Distribution Functions (CDF) of received powers for co- and cross-polarized links are plotted for three RS locations. Note that the co-polar received power (P_{CO}) is the average of $P_{+45/+45}$ and $P_{-45/-45}$ and similarly the cross-polar received power (P_{XP}) is the average of $P_{+45/-45}$ and $P_{-45/+45}$. These figures confirm that received powers generally exhibit small variations (over a spatial square grid) for simulated fixed relay polarimetric links, and that received power variations increase with the distance. For example, CDF curves for RS_6 show comparatively larger variations than RS_4. In addition, differences in polarized links at three RS locations are caused by the geometry and different orientations of RS antennas.

4.3.3 Covariance Matrix

Short antenna separations generally increase the channel correlation, as adjacent antennas will receive similar signal components. On the other side, dense multipath propagation decreases the correlation by spreading the signal such that MPCs are received from many different directions. If the polarized channels are highly correlated, then the potential multi-antenna gains may not always be obtainable. Therefore, covariance matrices of two polarized complex received signals $X(t)$and $Y(t)$ are evaluated through the following expression,

$$\rho = \frac{E\{(X - E(X))\,(Y - E(Y))^*\}}{\sqrt{E\{|X - E(X)|^2\}E\{|Y - E(Y)|^2\}}}. \tag{4.12}$$

Polarization-based correlation coefficients are presented in Table 4.3 for all polarimetric combinations at each RS location. Note that each polarized link is averaged over a 20 × 20 square grid. Listed correlation coefficients are all below 0.6, except for the covariance between (-45°/-45°) and (+45°/-45°) links. Such low correlation guarantees a good achievable polarization diversity gain.

4.3.4 Cross Polarization Discrimination

An important parameter to characterize the channel (propagation environment) polarization is the Cross-Polarization-Discrimination (XPD). It is defined as the ratio of the expected co-polarized average received power to the expected cross-polarized average received power [98]. It can be formulated as,

$$XPD = \frac{E\{P_{CO}\}}{E\{P_{XP}\}}, \tag{4.13}$$

where

- P_{CO} is the average of $|h_{+45/+45}|^2$ and $|h_{-45/-45}|^2$,
- P_{XP} is the average of $|h_{+45/-45}|^2$ and $|h_{-45/+45}|^2$,

where $h_{+45/+45}$, for instance, is the IR of co-polar link from +45° Tx to +45° Rx antenna, $h_{+45/-45}$ is the IR of cross-polar link from +45° Tx

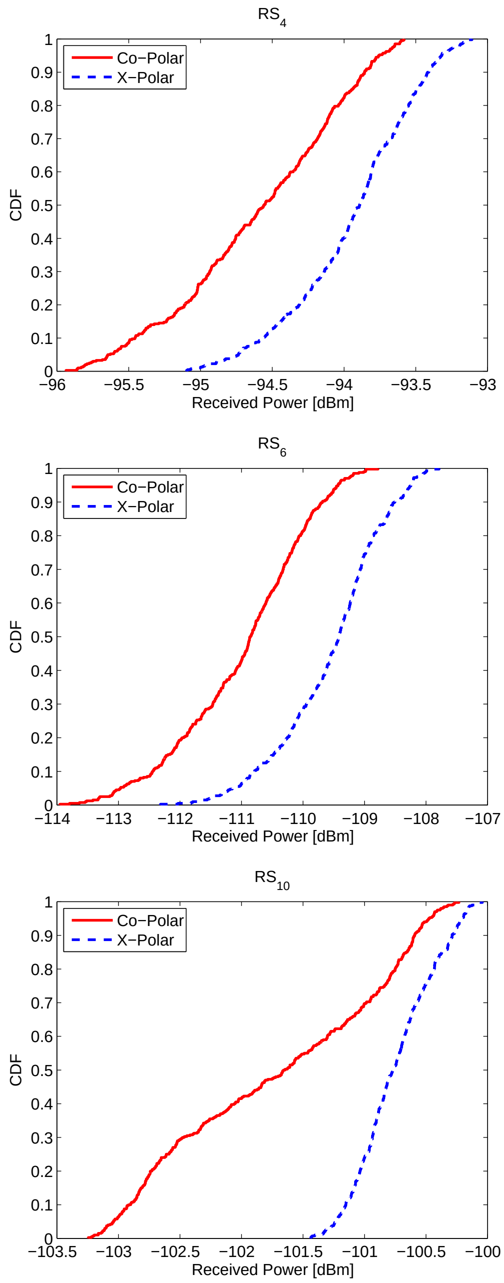

Figure 4.9: CDF [dB] curves of co- and cross-polar received powers for fixed polarimetric links at RS_4, RS_6 and RS_{10}

RS	Pol.	**+45/+45**	**+45/−45**	**−45/+45**	**−45/−45**
RS_4	+45/+45	1	0.58	0.17	0.52
	+45/−45	0.58	1	0.02	0.80
	−45/+45	0.17	0.02	1	0.10
	−45/−45	0.52	0.80	0.10	1
RS_6	+45/+45	1	0.14	0.57	0.45
	+45/−45	0.14	1	0.27	0.89
	−45/+45	0.57	0.27	1	0.14
	−45/−45	0.45	0.89	0.14	1
RS_{10}	+45/+45	1	0.37	0.23	0.44
	+45/−45	0.37	1	0.15	0.91
	−45/+45	0.23	0.15	1	0.27
	−45/−45	0.44	0.91	0.27	1

Table 4.3: Polarization-based covariance matrix (absolute values) at RS_4, RS_6 and RS_{10}

to −45° Rx, and so on. Note that the expectation in (4.13) is taken over the previously defined square grid. The XPD quantifies the separation between two transmission channels that use different polarization orientations [99]. The larger the XPD, the less energy is coupled between the cross-polarized channels [99].

Mean values of XPD over a square grid for three selected RS locations are listed in Table 4.4. Generally, mean values of XPD are small for all simulated links. XPD values are maximum within main direction of beams (in azimuth and elevation) and decrease when moving away from the main-lobe. This fact can be a possible reason for small XPD values because BS beams are not directed to any specific RS location. Small XPD values indicate high cross-coupling between channels, possibly due to lower RS antennas surrounded by dense scatterers resulting in depolarization [100]. The diffuse scattering components help for the depolarization at all locations. The depolarization effect due to the propagation environment (e.g., multiple reflections, diffractions and scattering) becomes more obvious in NLOS conditions [99], which is the case here in all simulated links. Small XPD values can cause CCI and consequently reduce the diversity gains. Therefore, such important parameters should be taken into account while exploiting the diversity gains of wireless channels.

Parameter	**RS_4**	**RS_6**	**RS_{10}**
XPD	0.65	1.40	0.97

Table 4.4: Mean XPD values (in dB) at three RS locations

4.4 Impact of BS on Wideband Characteristics

In this section, impact of the multi-beam BS antenna on wideband characteristics of fixed relay links is investigated, while focusing on the influence of narrow beams. Firstly, values of RMS delay spread are computed in a densely deployed environment. Secondly, since time domain channel models are helpful to investigate the most suitable transmission schemes in wireless networks, a TDL model with 20 MHz bandwidth is developed and subsequently analysed.

4.4.1 RMS Delay-Spread

The RMS delay-spread is calculated by the following relation [8, 101],

$$\tau_{RMS} = \sqrt{\frac{\Sigma_i \left[t_i - \frac{\Sigma_i t_i P_i}{\Sigma_i P_i}\right]^2}{\Sigma_i P_i}}, \tag{4.14}$$

where t_i is the time of arrival of i^{th} ray and P_i is the power of the corresponding ray.

RMS delay spread values at various RS locations in a square-cell topology are summarized in Table 4.5. Note that these values are extracted by utilizing the BS beam which provide maximum received power at that particular RS location. The RMS delay spread values are comparatively smaller for RS_3, RS_4, RS_8, RS_9 due to the street canyon effect. In general, RT-based values for RS locations are quite small, and remain around 20-35 ns. In addition to generally underestimated τ_{RMS} values by the RT tool owing to limited number of implemented interactions, small τ_{RMS} values may caused by the narrow beamwidth of the BS antenna. Indeed, the WINNER II model 5Bf prescribes delay-spread of around 76 ns for omnidirectional antennas [52]. At the same time, the IEEE 802.16 model mentions that for 10° antenna beamwidths, the delay-spread is reduced by a factor of approximately 2.6 [47]. Hence, RT-based values approach close to this ratio. Generally, small RMS delay spread corresponds to less effective pathloss for fixed relay links and vice versa.

RS	1	2	3	4	5	6	7	8	9	10	11
$\tau_{\mathbf{RMS}}$[ns]	29	32	20	21	24	26	34	22	20	29	35

Table 4.5: RMS delay spread values for BS-to-RS links in square-cell topology

4.4.2 Tapped Delay Line Model

The Power Delay Profile (PDP) gives the intensity of a signal received through a multipath channel as a function of the time delay [98]. The PDP of a given channel consists of a number of MPCs or taps. A tap is defined by its power (P) and relative delay (τ), as well as its K-factor. For the simulation setup described in Section 4.3.1, the PDP can be estimated by taking the spatially averaged IR of a multipath channel over a 20×20 square grid area. It can be formulated as,

$$P(\tau) = E\{|h_\tau|^2\}. \tag{4.15}$$

The spacing between grid points is one wavelength (i.e., $\lambda = 8.56$ cm). As an example of how the average power of polarized fixed link varies as a function of the delay, a spatially averaged PDP of -45° polarized BS to -45° polarized RS_4 link is given in Fig. 4.10. Note that both power and delays are spatially averaged to achieve exponential decaying power trend in the figure. The actual number of taps depends on the system bandwidth and on the propagation scenario. The reduction of RMS delay spread due to narrow beams results in fewer paths. On the contrary, the tap spacing depends inversely on the system bandwidth; hence larger bandwidth requires smaller tap spacing, resulting in a larger number of taps for a given maximum excess delay [98]. To develop the TDL model, averaged powers and delays (over a square grid) are normalized to the power and delay of the first tap respectively, thus only depicting the multipath effect. In this work, a 20 MHz system bandwidth is used. An example TDL model of the BS-to-RS link is shown in Fig. 4.11, and it is summarized in Table 4.6 including K-factor values for each tap. A threshold level of -30 dB is applied, so that any tap whose magnitude relative to the maximum falls below this level is excluded (30 dB would correspond to a typical system dynamic range). Tap magnitudes are roughly exponentially decaying. In most TDL models present in the literature, the tap amplitudes are considered as Rayleigh-distributed, except for the first tap. First tap is Ricean distributed if a strong direct contribution, i.e., LOS link exists. The first tap in our

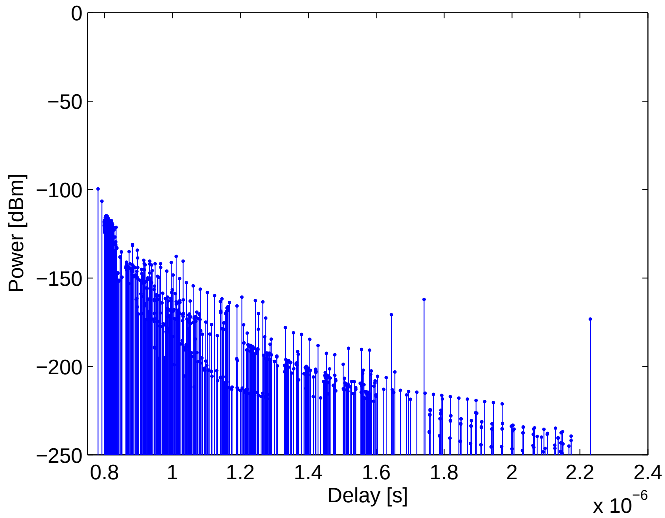

Figure 4.10: An example spatially averaged PDP of the BS-to-RS fixed relay link

model is Ricean distributed and its high K-factor is comparable to the reported first tap K-factors in IEEE 802.16 model for 30° beamwidth antenna [47]. However, magnitudes of all other taps (multipaths) listed in Table 4.6 are also Ricean distributed instead of Rayleigh, with high K-factors values, again owing to the narrow-beamwidth antennas. In other words, the number of paths falling within the main beamwidth becomes very small at large delays. This is in contrast to what happens when using antennas with larger beamwidths (in this case, the number of effective paths increase with delay). Furthermore, results show no significant change in K-factor values after first three taps.

4.5 Multi-beam BS Array Optimization

To provide increasing demands of high capacity densities in wireless networks, an innovative multi-beam BS architecture is proposed in the BuNGee project [7, 95]. However, performance of such high capacity architecture is often limited by interference. In order to suppress interference in the considered multi-cell scenario, an appropriate frequency planning is considered [95]. To further optimize BS antenna beams, a promising technique of array optimization is investigated in this section.

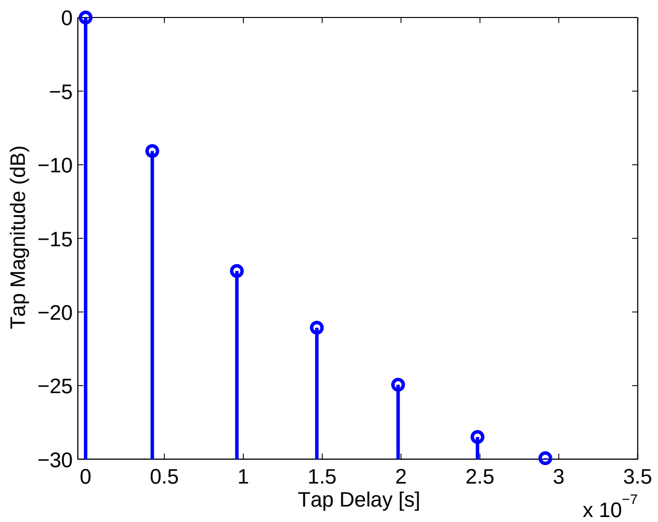

Figure 4.11: Tapped delay line model of the BS-to-RS fixed relay link

Parameters	**Delay [ns]**	**Power [dBm]**	**K-factor [dB]**
1	0	0	14.9
2	50	-9.06	19.8
3	100	-17.22	17.3
4	150	-21.07	27.8
5	200	-24.95	25.2
6	250	-28.49	26.5
7	300	-29.93	25.7

Table 4.6: Tapped delay line model of the BS-to-RS fixed relay link

4.5.1 Simulation Setup

In Fig. 4.12, the block diagram explains details of the scenario based on a square-cell topology described earlier in Section 4.1.5. It consists of five centrally located BSs (above roof-top at a height of 25 m from the ground level) equipped with N_B beams and M number of RSs in each cell. The central BS3-cell comprised of 24 beams, four corner cells only include half beams (12 out of 24) directed towards central cell for the sake of brevity. Different colors denote the frequency channels assigned to BS beams. Black dots depict the location number of RS antennas at the street intersections. Both BS and RS antennas are numbered

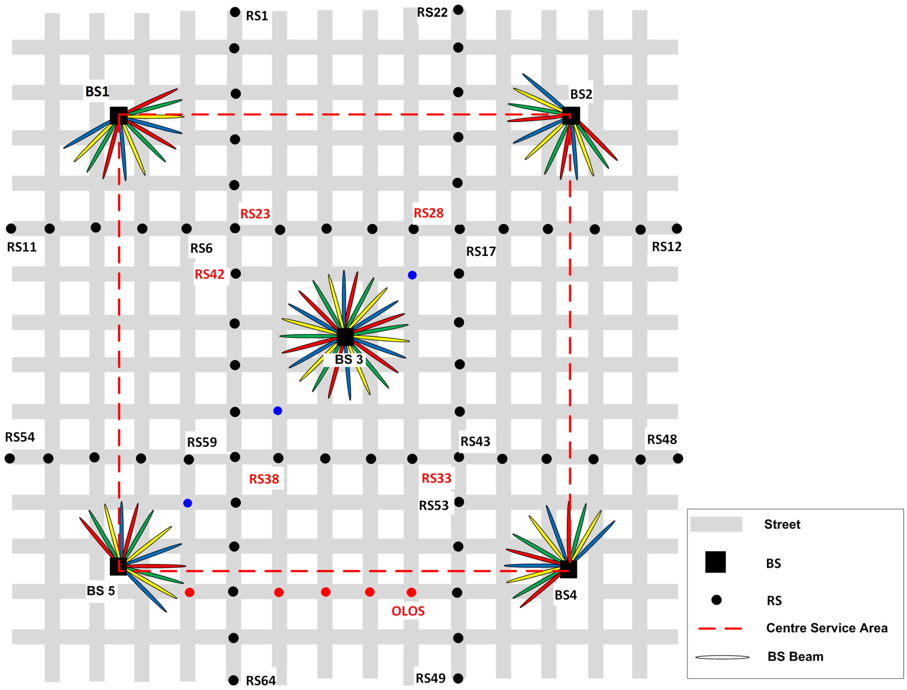

Figure 4.12: A multi-cell grid scenario based on a square-cell topology

in a clock-wise fashion. RS antennas are directed in streets towards respective BS in each cell. The number of RSs served by each beam can vary according to the specific geometry, e.g., a beam along a street or a diagonal is likely to include more RSs. The described setup has a scope to minimize the inter-cell interference between adjacent cells with an adequate frequency planning strategy [7] explained in the next section.

4.5.2 Frequency Planning

A significant improvement in interference can be expected by adopting the appropriate frequency planning in dense deployment scenarios with multi-beam antennas. The received signal at the i^{th} RS can be represented as the combination of signals from different beams,

$$y_i = H_{ij}x_j + \sum H_{ik}x_k + n_i, \tag{4.16}$$

where x_j is the transmit signal of the j^{th} beam, H_{ij} is the 2×2 channel matrix between the i^{th} RS and the j^{th} beam and n_i is the noise.

However, the throughput of one RS may severely be restricted due to interference from other beams using the same frequency channel. In this context, adequate frequency planning can potentially reduce interference (or equivalently the middle term in (4.16)) thus increasing the throughput.

Four channels are distributed such that potential interfering scenarios (i.e., co-located RSs at corner locations) are avoided through allocation of different frequency channels. Further details of the multi-BS frequency plan are illustrated in Fig. 4.12. Four different channels (red, green, yellow, blue) are utilized for four neighbouring beams in the order of channel 1 to channel 4. A total of 40 MHz frequency band (as proposed in the BuNGee project [7]) divided into four channels each of 10 MHz is utilized in simulations. Although different frequency planning strategies are possible, this particular frequency planning for a square-cell topology is chosen for efficient radio resource management within the BuNGee project [95].

While an appropriate frequency planning is vital for densely deployed scenario, reliable radio channels from narrow beamwidth antennas are still not guaranteed. The backhaul links are mainly bounded by interference which is often a direct consequence of multi-beam antenna side-lobes. Therefore, in order to further reduce the amount of interference, impact of array optimization on the downlink interference is investigated and analyzed by means of RT simulations.

4.5.3 Amplitude Tapering

The amplitude tapering technique is used to reduce side-lobe levels of the antenna relative to the main-beam. In general, highly directional antennas have side-lobes, which are often undesired as they may cause interference from different directions. Therefore, multi-beam antenna arrays are optimized by applying in-line attenuators between the beamforming network (see in Fig. 4.2) and the antenna inputs. Since the BM did not feature built-in taper, external attenuators in line with the interconnecting phase-matched cables are used.

Three patterns of side-lobe levels are attained by using different combinations of low value series attenuators at eight antenna ports. Two central ports remain un-attenuated (or 0 dB attenuators to preserve the fidelity). The next two ports utilize either 0 dB or 1 dB, while the remaining ports have progressively larger value attenuators such that the greatest attenuation occurs at extremities of the array [97]. In other

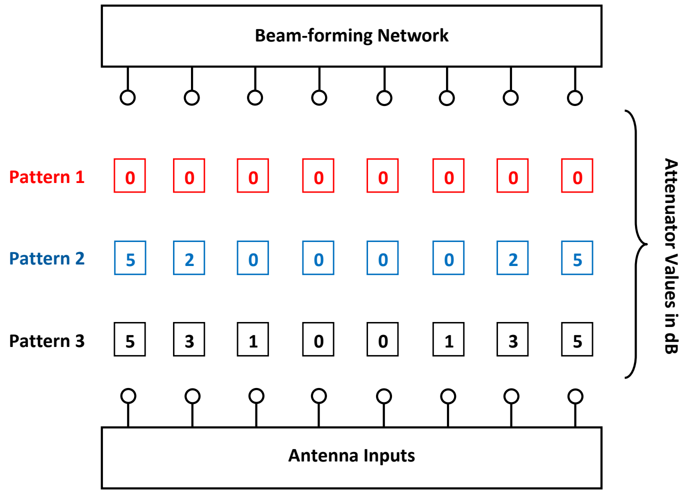

Figure 4.13: The schematic diagram of amplitude tapering showing attenuator values (dB) between the beam-forming network and the antenna inputs

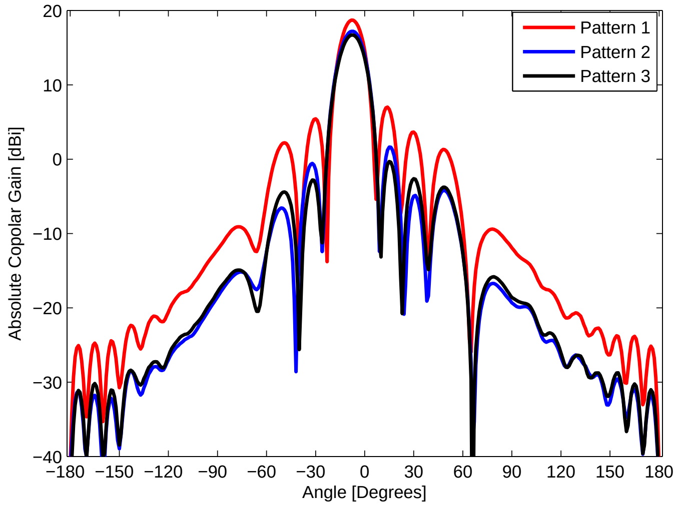

Figure 4.14: Example measured beam patterns (azimuth) of the multi-beam BS antenna with and without amplitude tapering

words, values of used series attenuators are 0 dB for Pattern 1; 0, 0, 2, 5 dB for Pattern 2 and 0, 1, 3, 5 dB for Pattern 3 as illustrated in Fig. 4.13. Note that further tapering is not recommended in order to maintain gain of the main-beam. Indeed, amplitude tapering is a trade-off between achievable low side-lobe levels and gain of the main-beam. Example azimuth beam Pattern 1 (no tapering) along with Pattern 2 (intermediate amplitude tapering) and Pattern 3 (maximum tapering) are illustrated in Fig. 4.14. It can be observed in the figure that the side-lobe level drops with increasing amplitude taper relative to the main-beam in the azimuth plane without significantly affecting the peak gain. Peak gains and side-lobes level are a function of pointing angle and varies across the 90° sector. 3 dB beamwidth in azimuth vary slightly with amplitude tapering. The elevation 3 dB beamwidth of all the beams is approximately 10° with 2° electrical down-tilt and it remains unaffected with amplitude tapering [11]. Various relevant parameters of three patterns are summarized in Table 4.7.

Parameters	**Pattern 1**	**Pattern 2**	**Pattern 3**
Peak gain [dBi]	18.7	17.2	16.7
Beamwidth [deg]	13.6	14.9	15
1st right side-lobe [dB]	-12.8	-15.6	-17.0
1st left side-lobe [dB]	-14.3	-17.8	-19.5
2nd right side-lobe [dB]	-15.1	-22.1	-19.3
2nd left side-lobe [dB]	-16.5	-23.8	-20.4
3rd right side-lobe [dB]	-17.4	-21.4	-21.1
3rd left side-lobe [dB]	-27.8	-32.6	-31.6

Table 4.7: Parameters of three beam patterns (azimuth) of the BS antenna

4.5.4 Co-Channel Interference

Co-Channel Interference (CCI), also referred to as intra-cell interference, is introduced in a cell due to excessive spectral reuse in multi-beam antennas spatially. It is evaluated in terms of Signal to Interference Ratio (SIR). For a scenario shown in Fig. 4.12, SIR at a particular RS location can be expressed as,

$$SIR = \frac{P_{\max}(RS)}{I_{\text{agr}}}, \tag{4.17}$$

where $P_{\max}(\text{RS})$ is the largest (in magnitude) received power at a particular RS location transmitted by a BS beam and is therefore defined as the carrier (i.e., the wanted signal). I_{agr} is aggregate interference from all other N_B/R interfering beams of the same cell. N_B are the total number of beams and R is the spectral reuse factor. I_{agr} can be expressed as,

$$I_{\text{agr}} = \sum_{i=1}^{\frac{N_B}{R}-1} P_i, \tag{4.18}$$

where P_i is the power level of the i^{th} beam at a particular RS location. Naturally, power level P_i differ at a desired RS location, due to different BS beams orientations and multipaths. The interfering beams mostly contribute through side-lobes, however some adjacent beams interfere with the power levels close to $P_{\max}$ at a desired RS, especially when they have similar arrival paths in the street.

4.5.5 Inter-Cell Interference

Apart from CCI, multiple beams (of same frequency channel) from neighbouring cells can also contribute a significant interference in the cell, known as Inter-Cell Interference (ICI). It is imperative to limit the ICI between different cells for efficient radio resource management. Therefore, ICI is evaluated by considering multiple cells as illustrated in Fig. 4.12. It can be estimated by replacing I_{agr} in (4.17) by,

$$I_{\text{agr}} = \sum_{i=1}^{\frac{N_B}{R}-1} P_i + \sum_{j=1}^{\frac{N_B}{R}} P_j + \sum_{k=1}^{\frac{N_B}{R}} P_k + \sum_{l=1}^{\frac{N_B}{R}} P_l + \sum_{m=1}^{\frac{N_B}{R}} P_m, \tag{4.19}$$

where P_i is the power level of i^{th} interfering beam at a particular RS location in the cell. Similarly, P_j, P_k, P_l and P_m are power levels of interfering beams from neighbouring BS1, BS2, BS4 and BS5 cells respectively.

In order to reduce the interference to an acceptable level, narrow beams of the BS antenna are exploited. However, reducing the beamwidth lower than 15°-20° significantly increases the effective pathloss as described in Section 4.2.3. For example, a narrow beam of 15° beamwidth causes approximately 9 dB increase in the effective pathloss, thus suggesting a trade-off between acceptable interference level and effective pathloss. This implies that large number of narrow beams still have the

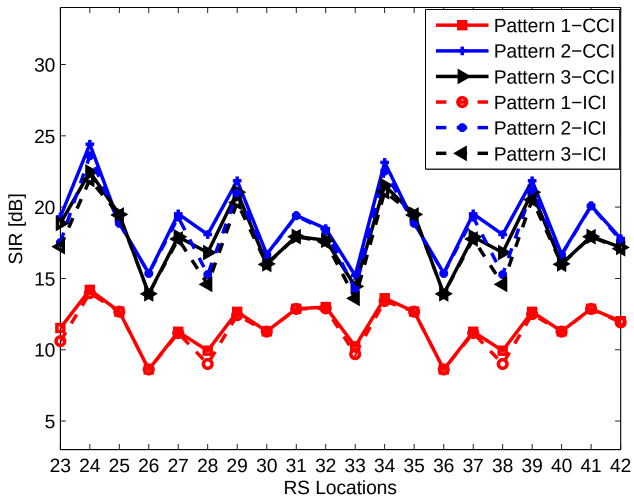

Figure 4.15: Combined CCI and ICI in BS3-cell for three patterns of the multi-beam antenna

potential to interfere with each other, thus not fully removing the CCI. The farther the co-channel beams are separated from each other; the lower the expected CCI level as the antenna pattern gradually tapers off with increasing angles from the boresight. Results based on the array optimization technique are evaluated and analyzed in the next section.

4.5.6 Results and Analysis

To demonstrate the improvement with array optimization in the multi-beam BS antenna, RT simulations are performed in an interfering environment. Fig. 4.15 illustrates the combined (including CCI and ICI) results for central-cell (BS3) at 20 RS locations (RS23-42) with three patterns. Results of only one frequency channel (out of four frequency channels) are presented here. Similar results of other frequency channels are not included for the sake of brevity.

It can be observed that both amplitude tapered patterns (Pattern 2 and Pattern 3) have significantly improved the SIR level compared with the non-tapered Pattern 1. SIR improvement ranges from 5 to 10 dB at different RS locations. However, in general Pattern 2 performs slightly better than Pattern 3. This discrepancy may be explained by the fact that the 2nd and 3rd side-lobes of Pattern 2 are smaller than those

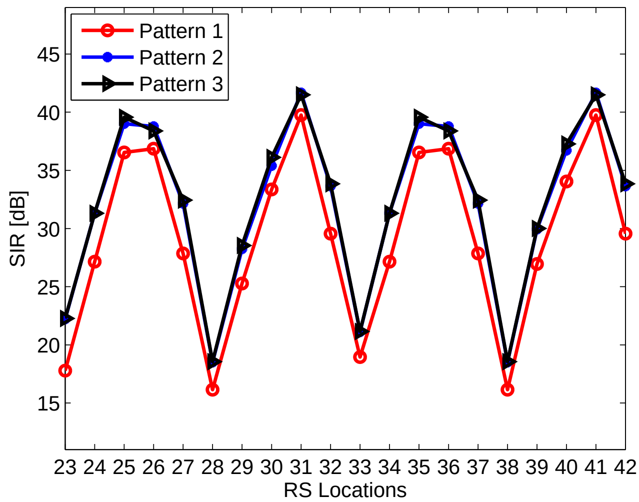

Figure 4.16: ICI excluding CCI of BS3-cell for three patterns of the multi-beam antenna

of Pattern 3 (as summarized in Table 4.7), resulting in slightly better SIR levels. Furthermore, magnitude of the wanted signal at the desired RS location remains almost unaffected for three investigated patterns. It confirms that the received power or equivalently gain loss is independent of the tapering effect and largely depends upon antenna beamwidths and other relevant channel parameters.

When taking into account the ICI from the neighbouring cell, results depicted in Fig. 4.15 show that SIR level slightly decreases for all patterns (dashed lines). The noticeable results are observed at cell-edges (i.e., RS23, 28, 33, 38) because of equal distance from two BSs. This fact is further illustrated in Fig. 4.16, where only ICI is considered excluding impact of CCI of the BS3-cell, or equivalently dropping the first term in (4.19). Results in Fig. 4.16 confirm that SIR values decrease significantly at corner-located RSs due to high ICI, regardless of beam patterns. However, a slight improvement in SIR is achieved by Pattern 2 and 3. In general, it can be reported that ICI from the immediate neighbouring cell is high only at cell-edges (i.e., corner locations in a square-cell topology). In this analysis, only the downlink transmission is discussed, although similar approaches can readily be applied in the uplink transmission links.

4.5.7 Obstructed LOS and NLOS Scenarios

To further characterize CCI and ICI, impact of array optimization in two scenarios, Obstructed LOS (OLOS) and NLOS, is investigated in this section. For this purpose, seven RS antennas (A to G) at street intersections are placed in two different directions, as depicted by red and blue dots in Fig. 4.12. Results shown in Fig. 4.17 confirm again a significant improvement in SIR with tapered patterns for both cases. Generally, the SIR improvement is in the range of 5 to 8 dB. However, the SIR exhibits better performance in the OLOS than the NLOS scenario. It appears again that Pattern 2 performs better than Pattern 3 in both scenarios. A slight increase in the SIR level with the distance in both scenarios is also observed.

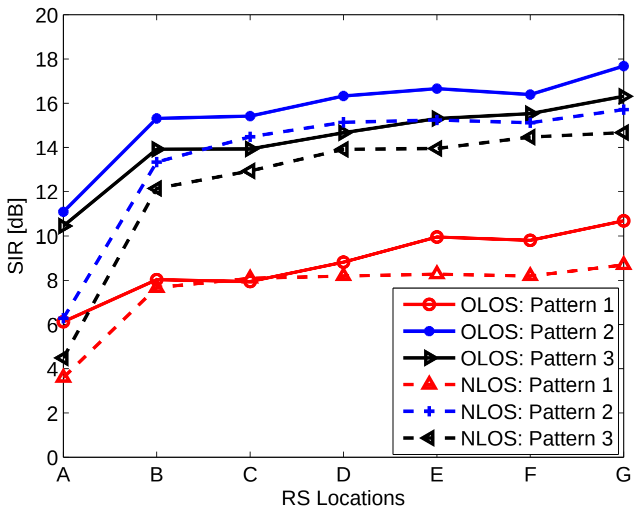

Figure 4.17: SIR (dB) for three beam patterns when RSs are placed in OLOS and NLOS directions

From the above analysis it is evident that array optimization in multi-beam antennas can play an important role in reducing interference, especially CCI, in dense deployment scenarios. By controlling side-lobes of multi-beam BS antennas, SIR can be maintained above 12 dB in a cell which guarantees the required quality of service in wireless networks. This further ability can lead to increase the throughput density as evaluated in the next section.

4.6 Performance Evaluation of Backhaul Links

In order to boost the throughput density of the overall wireless network, high capacity backhaul links are required. For this purpose, the density of distributed RSs below the rooftop (e.g., on utility poles or traffic lights etc) is increased in the considered deployment scenario (i.e., square-cell topology) [7]. As mentioned earlier, multi-beam antennas combined with aggressive spectral reuse are promising to create high-capacity hubs and to provide greatly increased throughput density. However, large number of narrow beams causes interference which can be reduced by employing the array optimization technique as revealed by results (i.e., SIR improvement of 5 to 8 dB) in the previous section. In this context, within framework of the BuNGee project, system level simulations are performed to evaluate the performance of interference bound backhaul links in high capacity wireless networks. Part of this work is jointly published in [11, 12] with BuNGee partners.

4.6.1 Simulation Setup

A multi-cell square topology in an urban environment is applied for the system level modeling as shown in Fig. 4.12. A total number of 5 BSs (64 beams) are assumed to serve 64 RSs. There are 16 streets both East-West (E-W) and North-South (N-S), and that forms a 15×15 block area. The BS antennas are placed above rooftop in centre of the cell and 5 BS form a 9 square-cell deployment environment in this case. The total service area is 1.82 km^2 (1.35 km $\times$ 1.35 km). The parameters used for system level simulations are summarized in Table 4.8

Parameter	**Value**
BS transmit power	37 dBm
RS transmit power	27 dBm
Carrier frequency	3.5 GHz
No. of channels	4
Lognormal shadowing	6 dB
Noise floor	-114 dBm/MHz

Table 4.8: Parameters for system level simulations

On the receive side, a total of 1500 users (MSs) are uniformly distributed on the streets. This work primarily focuses on outdoor users, however a dedicated indoor coverage can be assumed for indoor users.

The distributed users are served by 64 RSs placed outdoor at the street level. MSs are associated to the best available RSs in terms of Signal-to-Noise Ratio (SNR) levels. The user density is considered as 800 MSs per square kilometer. However, only MSs placed in the highlighted centre service area in Fig. 4.12 are taken into account when measuring the throughput density, in order to provide a more representative interference environment of a larger network. Moreover, the noise is also always present in any real world wireless network. Therefore, a noise floor level (-114 dBm/MHz) is taken into account for system level simulations of the throughput density [12].

Four 10 MHz channels in total are assumed for simulations. 30 OFDMA format sub-channels are assumed within each 10 MHz channel. RSs located at the top and bottom of each cell are designed to serve N-S streets, and RSs on the left and right serve the E-W streets. The two RS beams pointing in opposite directions should use two different channels and neighboring RS beams use two different channels. Similarly, RSs that serve N-S streets use two different channels from those that serve E-W streets. A $50\% - 50\%$ TDD split is assumed in simulations between the downlink and the uplink. To estimate pathloss of multi-links, RT simulations are performed for the BS-to-RS fixed relay link (also referred to as the backhaul link), while the RS-to-MS link (i.e., access link) is estimated through a similar existing scenario B1 of the WINNER II channel model [52]. Pathloss for the BS-to-MS link, a common scenario in wireless networks, is also obtained by using C2 scenario of the WINNER II channel model [52]. The access link is assumed to utilize the same resources (i.e., time slots or frequency channels) as the backhaul link, hence referred to as in-band backhauling.

A file-transfer based traffic model is applied to generate traffic for the downlink transmission. The inter-arrival time of transmissions follow a negative exponential distribution and the file size follows Pareto distribution. The PDF of Pareto distribution is defined as [102],

$$p_X(x) = \alpha.(x_m^{\alpha}/x^{\alpha+1}) \qquad \text{for } x \geq x_m, \tag{4.20}$$

where the mean value of the distribution is given as,

$$E(X) = \frac{\alpha x_m}{\alpha - 1} \qquad \text{for } \alpha > 1. \tag{4.21}$$

Retransmission is assumed such that file transmissions that are initially blocked will back-off for a random time. The mean back-off time is set equal to the mean inter-arrival time of files in the simulation. Again, a fairly basic back-off strategy is used in order to have limited impact on the network performance. The offered traffic levels can be adjusted by changing the average file size and average inter-arrival time [102].

4.6.2 Performance Measures

In this section, based on [12], impact of the array optimization technique (i.e., amplitude tapering to reduced side-lobes) is investigated at the system level by examining mainly the throughput density and the Grade of Service (GoS) measurements (i.e., delay and probability of retry). Note that system level simulations are performed within framework of the BuNGee project and the joint work is published in [11, 12].

Throughput Density

The throughput density is used as a main measure to describe the network performance. The average throughput density can be defined as [11, 102],

$$Thr_D = \frac{Thr_s}{A_s}, \tag{4.22}$$

where A_s is the service area and Thr_s is the backhaul throughput which can be defined as [102],

$$Thr_S = \frac{\sum_{i=1}^{N_u} \sum_{k=1}^{n_i} \sum_{t=0}^{T_k} Thr(t)}{t_s} .P_{TDD}, \tag{4.23}$$

where $Thr(t)$ is the throughput value of a link obtained at time t, and it is updated constantly in the simulation. Tk is the transmission time of the k^{th} transmission of an entity, and n_i is the total number of transmissions that have been completed by the i^{th} entity in the simulation. N_u is the total number of entities in the simulation. t_s is the simulation time and P_{TDD} is the percentage of time slots allocated to the downlink or the uplink. Since a $50\% - 50\%$ TDD split is assumed between the downlink and the uplink, therefore P_{TDD} is 0.5 [12].

Grade of Service

Two GoS measurements are considered to describe the network performance, the system delay and the retry probability. The system delay is obtained by the following expression [11],

$$t_D = \frac{\sum_{i=1}^{N_u} \sum_{k=1}^{n_i} (t_T(k) + t_B(k))}{N_f}, \tag{4.24}$$

where t_T is the transmission time of file k and t_B is the back-off time of file k, n_i is the total number of files that have been transmitted by the i^{th} entity in the simulation and N_u is the total number of entities in the simulation.

The probability of retry is also used in this simulation to describe the probability that the current file transmission request has been rejected by the system. The probability of retry $P_{retry}(t)$ at time t is defined by [102],

$$P_{retry}(t) = \frac{N_r(t)}{N_a(t)}, \tag{4.25}$$

where $N_r(t)$ is the total number of reject file transmissions of the system by time t, and $N_a(t)$ is the total number of file transmission requests (including retries) of the system by time t.

4.6.3 Results and Analysis

The performance results obtained from system level simulations are presented and analyzed in this section. Fig. 4.18 shows the downlink end-to-end system throughput density performance of the hierarchical wireless network at different system offered traffic levels. Pattern 2 and Pattern 3 perform better than Pattern 1 as expected due to reduced side-lobes. Pattern 1 achieves the lowest throughput density in general and its performance is especially poor at high traffic levels. The performance of Pattern 2 and Pattern 3 are almost identical throughout the simulation. It can be explained in the same way as explained in Fig. 4.15, with the difference in the performance being only marginal. Both amplitude tapered patterns (2 and 3) in this case have significantly improved performance with a throughput density as high as 680 Mbps/km^2 at 1.6 Gbps/km^2 offered traffic density.

Fig. 4.19 and Fig. 4.20 illustrate GoS measurements of the hierarchical wireless network. It can be clearly seen that Pattern 1 which has normal side-lobes (i.e., without amplitude tapering) suffers a higher level of interference which in turn leads to a higher level of interruption to the system. Both the delay and the retry probability of Pattern 1 are significantly higher than those with reduced side-lobe patterns. Pattern

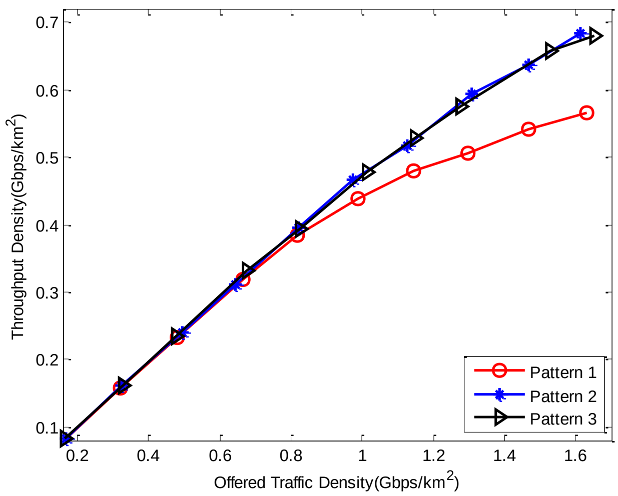

Figure 4.18: Downlink system throughput density versus system offered traffic density

2 performs slightly better than Pattern 3 due to second and third level side-lobes difference as explained earlier. Results are also consistent with earlier results in Fig. 4.15.

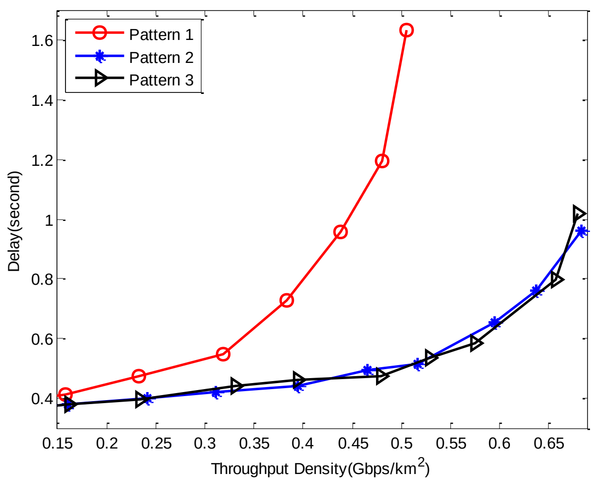

Figure 4.19: Downlink delay versus system throughput density

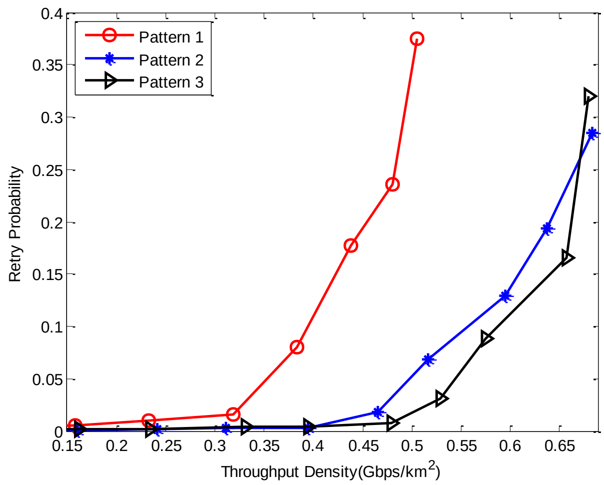

Figure 4.20: Probability of retry versus system throughput density

It can be seen from figures that a downlink throughput density over 0.6 Gbps/km^2 can be achieved with a satisfactory GoS performance by reducing the side-lobe level of the multi-beam BS antenna. An overall throughput density of 1.2 Gbps/km^2 can be expected since a $50\% - 50\%$ TDD split between the downlink and the uplink is assumed. Pattern 1 with normal side-lobes can only achieve about 0.35 Gbps/km^2 downlink throughput density if 5% GoS requirements for the system retry probability is applied. The overall end-to-end throughput density is only about 0.7 Gbps/km^2 in this case. A significant improvement in the overall throughput density is achieved through reducing side-lobe levels of narrow beams. It is clear that the relative gain between the main-lobe and side-lobes has a significant impact on the system performance, and the relative gain may be better improved in some circumstances by reducing side-lobes rather than boosting the peak gain.

4.7 Conclusions

In first part of this chapter, architecture of the multi-beam BS has been detailed. The impact of narrow beams on the pathloss model has been characterized. It has been found that pathloss increases due to narrow-beamwidths of the multi-beam BS antenna. RT-based GRF model has been derived to adequately compare pathloss results of the WINNER II channel model and RT simulations. None of WINNER II models is able to adequately represent RT-based pathloss in the evaluated scenario. However, C2 model can be used in conjunction with an appropriate GRF model to offer a good compromise in the targeted range of distance. Moreover, the RT-based pathloss exponent seems to match the B5f and C2 exponents after taking GRF into account. Furthermore, several polarized MIMO characteristics (e.g., spatial K-factor, polarization-based covariance matrix and cross polarization discrimination) of BS-to-RS fixed polarimetric links have been investigated in this chapter. Results have illustrated discrepancies mainly due to narrow beams and the densely deployed scenario. However, RT-based results seem to agree with the existing models (e.g., WINNER II and IEEE 802.16), when peculiarities (specifically, narrow-beamwidth antennas) of the innovative architecture are taken into account. Spatial K-factor values come closer to reported K-factors in the literature when a beamwidth factor from IEEE 802.16 is included. It can be concluded from the analysis of correlation coefficients and mean values of XPD that some fixed polarimetric links are correlated due to higher cross-coupling and greater degree of depolarization in NLOS conditions. However, generally statistics are in agreement with those in existing models. A TDL model developed for 20 MHz bandwidth has also demonstrated a strong dependence upon narrow beamwidth of antennas.

In the second part of this chapter, interference caused by the multi-beam BS architecture with dense deployment topologies has been characterized. Two types of interference (CCI due to excessive spectral reuse and ICI due to the same frequency beams from the neighboring cell) have been analyzed. The array optimization in the multi-beam BS antenna has revealed that,

- tapered beams reduce the CCI (improve SIR) significantly, between 5 and 8 dB,
- no substantial increase in pathloss has been observed at investigated RS locations, because the peak gains of the investigated patterns are almost identical,
- SIR can be maintained above the acceptable level of 12 dB by reducing side-lobes which guarantees the required quality of service in wireless networks.

Therefore, array optimization can be a promising solution to suppress the CCI encountered by a multi-beam antenna and hence lead to a higher achievable throughput density.

In the last part, performance of interference bound links in high capacity wireless networks has been evaluated within framework of the BuNGee project. System level simulations have demonstrated a significant improvement in the throughput density by array optimization in the multi-beam BS antenna. The wireless backhaul links suffers significantly less interruption because of reduced side-lobes which in turn results in a significantly improved achievable throughput density. The wireless network achieves a downlink throughput density over 0.6 Gbps/km^2. An overall throughput density of 1.2 Gbps/km^2 is expected when taking both up- and downlinks into account.

CHAPTER 5

Relay Architecture Designs

To address constantly growing capacity demand, the concept of small cells (denser deployment) is gaining popularity [2]. The small cells are expected to be powered with low positioned antennas enabling high frequency reuse and high SINR. For this purpose, the relay architecture is introduced in the literature as a network element designed to increase the network capacity and coverage. Essentially the idea is to place the RS in such a way that it has a good wireless connection with the BS (referred to as backhaul link), yet much closer to some of the user terminals (named as access links). The relay technology has significant advantage in its capability for in-band operation due to the sharing of resources between the backhaul and access links [2, 4, 103]. Especially, it promises to be an economically efficient solution in coverage-limited conditions when wired backhauling becomes more complicated or the use of high frequencies ($>$ 6 GHz) requires LOS which cannot be assured in dense deployments. However, there are number of associated parameters that must be carefully chosen to ensure efficient relay architecture designs in wireless networks. Two such parameters are considered and characterized in this chapter:

- the optimal orientation of the relay antenna (i.e., the direction in which main-lobe has to be steered) is an important factor to be considered carefully in order to maximize the potential relay contributions.

- the relay antenna height is another important parameter which must be considered carefully in the channel modeling. The relay antenna should be placed at a favourable radio location such that the BS-to-RS propagation link provide high quality transmission as depicted in Fig. 5.1. However, in this case the RS can more likely cause interference to adjacent cells.

Both parameters are investigated and characterized for a square-cell topology (urban environment) presented earlier in Chapter 4.

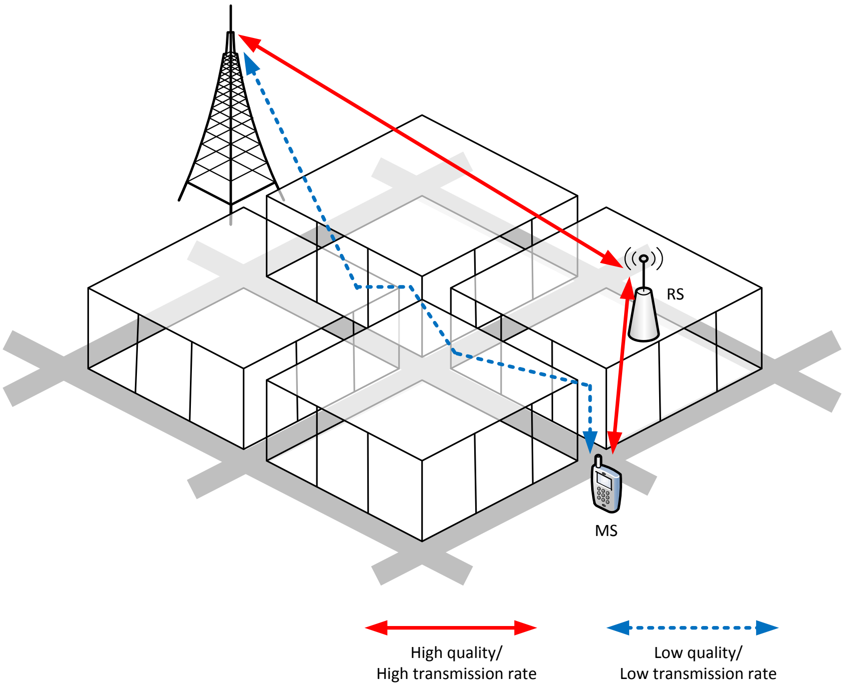

Figure 5.1: An example of a typical high quality relay link

5.1 Relay Station Antenna

To meet rising demands of the high capacity and throughput, the concept of spatially distributed RSs (forming small cells) over large areas, being fed directly by a large number of BS beams, is considered as a promising solution in context of the BuNGee project [7]. In such an architecture, each RS is equipped with a dual-polarized directional antenna as shown mounted on a mast in Fig. 5.2 (left). The directional antenna has approximate 13 dBi gain and 40° beamwidth both in azimuth and elevation without any downward tilt. The RS antenna uses a 4×4 element network in diamond formation as depicted in Fig. 5.2 (right). This format produces very low side-lobes and is especially suitable for slanted $\pm 45°$ polarizations. It is designed to have an isolation of about 30 dB between ports. A typical radiation pattern (azimuth) of one port shows approximately 20 dB side-lobe level below the peak gain as demonstrated in Fig. 5.3 (top). A full 3-D radiation pattern

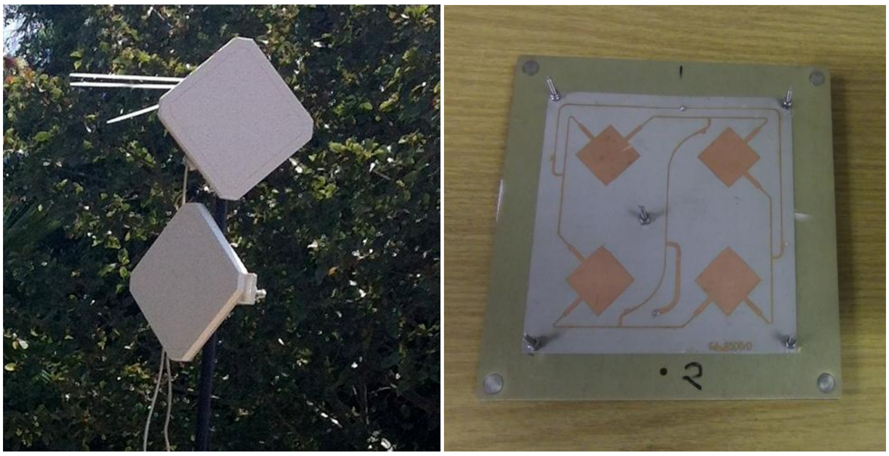

Figure 5.2: RS antenna: front view mounted on a mast (left), the diamond element design to produce slant 45° polarization (right)

is presented in Fig. 5.3 (bottom). At 3.5 GHz frequency, approximate sizes of the RS antenna are 160 mm × 160 mm × 25 mm. The RS antenna is specifically designed and developed by Cobham Antennas within framework of the BuNGee project [97].

5.2 Impact of Relay Antenna Orientation

To increase the capacity density, spectral efficiency and coverage, highly directional antennas are proposed for wireless backhaul links in the BuNGee project [7]. However, highly directional narrow-beam BS antennas necessitate to steer main-lobe of the RS antenna in an appropriate direction. A correct antenna orientation is relevant to achieve maximum benefit from the antenna's gains, thus providing better wireless link quality. Therefore, RT simulations are performed to investigate optimal orientation of RS antennas in a densely deployed environment.

5.2.1 Setup Description

Like in Chapter 4, a square-cell topology in an urban environment is considered to investigate orientation of the relay antenna at 3.5 GHz

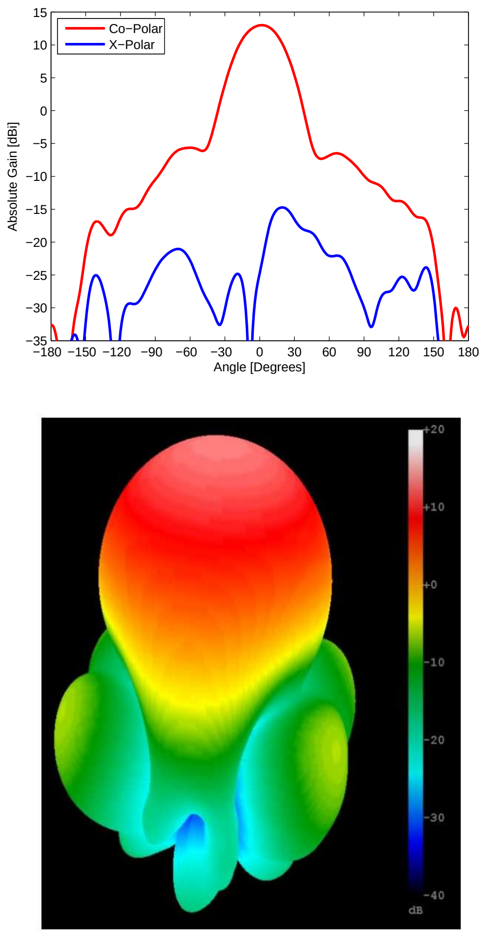

Figure 5.3: RS antenna radiation patterns: a single azimuth beam pattern (top), a full 3-D radiation pattern (bottom)

carrier frequency as illustrated in Fig. 5.4, where black dots represent RS locations at street intersections. The BS is placed in the centre of the cell at a height of 25 m (i.e., 5 m above the rooftop), whereas the RS antenna is placed at a height of 5 m (below roof top) from the ground level. While exploiting the symmetric property of a square-cell topology, only two sectors of the multi-beam BS antenna are used for the sake of brevity. Full 3-D radiation patterns of both antennas are employed in RT tool for simulations. The details of radiation patterns of BS and RS antennas are already presented in respective sections, whereas RT specific parameters are summarized in Table 5.1.

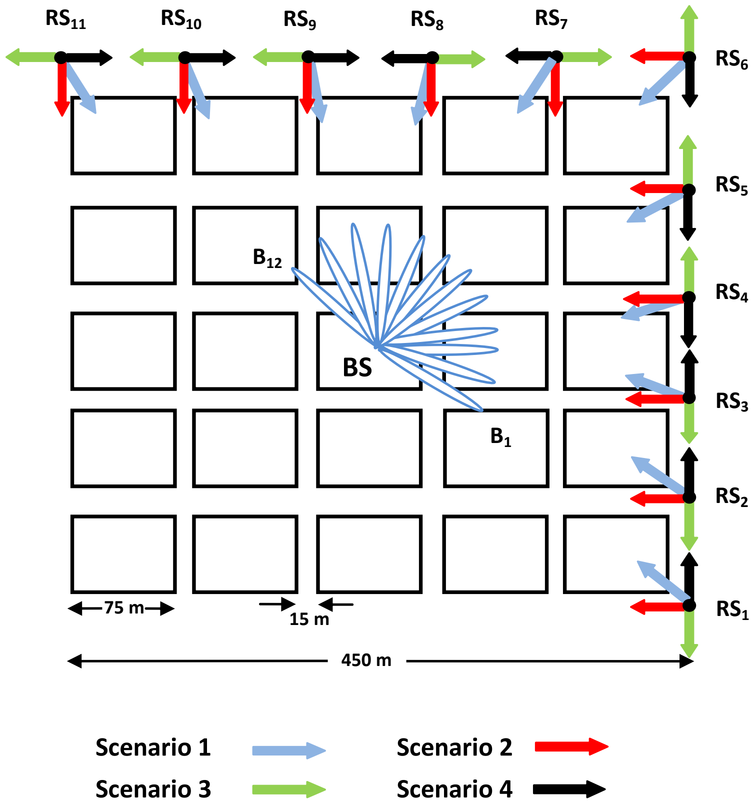

Figure 5.4: Block diagram of a square-cell topology illustrating four scenarios of the RS antenna orientation

Parameters	Value
Carrier frequency	3.5 GHz
Concrete, ε_r	4.85
Concrete, κ	0.173 S/m
No. of reflections	3
BS antenna gain	18.8 dBi
RS antenna gain	13 dBi

Table 5.1: RT simulation parameters

Several practical deployment scenarios within BuNGee project [7,95] are considered to investigate the optimal orientation of the RS antenna as indicated by arrows in Fig. 5.4. Each RS is placed at the street intersection which corresponds to a distance of 7.5 m from buildings on either side of the street. The wall at 7.5 m distance will receive less PFD exposure than a wall at 2 m by directing antennas along the axis of the street (see Section 4.1.4 for details). In the context of the BuNGee project [7], following four scenarios are investigated:

- **Scenario 1**, where main-lobe of the RS antenna is steered in the largest power ray direction (considering both azimuth and elevation angles) as shown by blue arrows in Fig. 5.4. The procedure to compute the corresponding azimuth and elevation angles for the largest power ray will be described later.
- **Scenario 2**, where main-lobe of each RS antenna is directed inward along the axis (azimuth) of the street without any up- or downward tilt as indicated by red arrows in Fig. 5.4.
- **Scenario 3**, where main-lobes of RS antennas are directed in perpendicular streets with respect to Scenario 2. For example, RS_1, RS_2 and RS_3 are directed towards south direction, while RS_4, RS_5 and RS_6 are steered towards north direction. The respective directions are indicated by green arrows without any elevation tilt.
- **Scenario 4**, in which RS antennas are directed in opposite directions of Scenario 3. Black arrows in Fig. 5.4 show directions of RS antennas without any up- or downward tilt.

First scenario seems intuitively the optimal choice. However, this needs to be confirmed through RT simulations along with magnitude of improvement in pathloss. Last three scenarios represent practical orientations of the RS antenna along the axis of three streets. Note that outward orientation (i.e., in the fourth street) of the RS antenna with respect to the central BS is not considered due to comparatively larger pathloss.

To compute the largest power ray (or MPC) reaching at any RS location, RT simulations are performed with an omnidirectional antenna at the Rx side. Fig. 5.5 shows example plots of the received power against azimuth (θ) and elevation (ϕ) angles separately. The largest contributing ray (in the total received power) is selected for both azimuth and elevation angles. In this particular example, θ = 178° and ϕ= 15° upward represent direction of the largest power ray. Naturally, most of interacting rays (or MPCs) reach at the RS location through streets (i.e., 90°, -90°, 0° or 180° in azimuth).

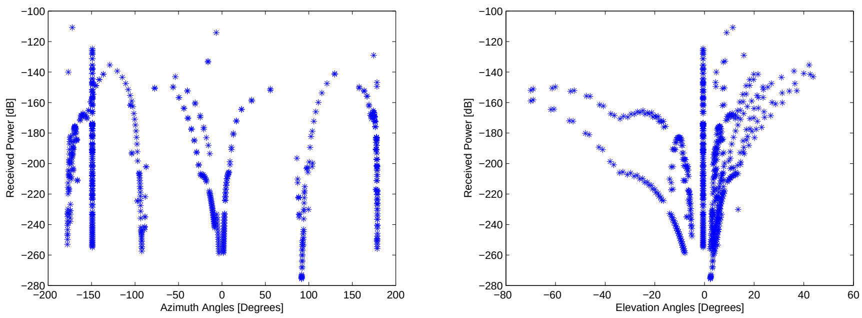

Figure 5.5: Example plots of the received power showing each contributing ray (MPC) against azimuth angles (left) and elevation angles (right)

5.2.2 Results and Analysis

RT simulations are performed for all BS-to-RS links (i.e., from 12 BS beams to 11 RS locations in the defined topology) with +45° polarization both at the Tx and Rx sides. The results are evaluated in terms of pathloss calculated by (4.9). The CDF of pathloss is plotted in Fig. 5.6. Scenario 1 demonstrates the smallest pathloss compared with other scenarios. It is followed with Scenario 2, while Scenario 3 and Scenario 4 indicate comparatively larger pathloss from all BS beams.

To characterize differences among the scenarios at each RS location, a single beam is selected which provides maximum power at the investigated RS location. The corresponding results for four simulated scenarios are illustrated in Fig. 5.7. It is shown again that Scenario 1 performs better than other investigated scenarios at all RS locations. However, performance of Scenario 2 becomes comparable at some RS locations (e.g., 3, 4, 8 and 9) owing to the street canyon effect. As a matter of fact, largest power rays found for such locations lie in the same street as of Scenario 2, thus pathloss values of both scenarios approach closer. On the other side, Scenario 2 demonstrates a significant increase in pathloss at some RS locations (e.g., 1, 2, 6, 10 and 11) compared to Scenario 1. This increase in pathloss can mainly be explained by orientation of

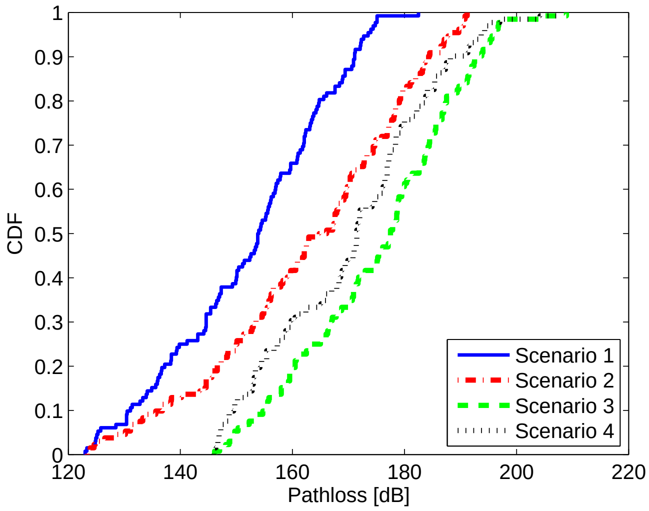

Figure 5.6: Empirical CDF of pathloss for four simulated scenarios

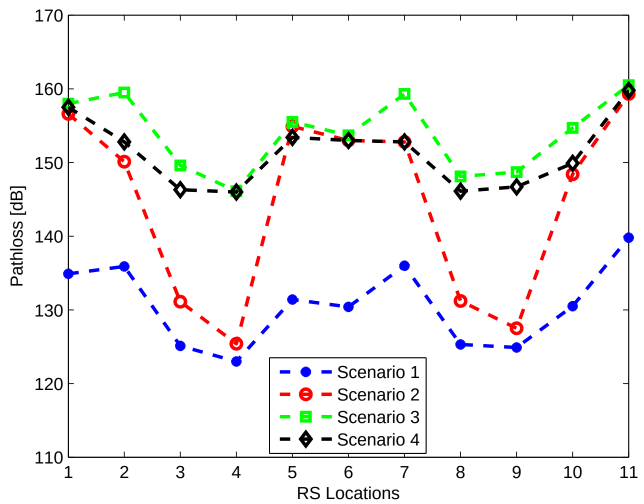

Figure 5.7: Pathloss for four simulated scenarios at 11 RS locations in a square topology

the RS antenna's main-lobe. If a narrow beam antenna is steered in a particular direction, it may fail to capture some important MPCs falling outside of antenna beamwidth coming from other directions. This effect is more dominant in deep NLOS conditions or dense scattering environments, thus causing a significant increase in pathloss [9]. Note that the pathloss difference between Scenario 1 and Scenario 2 vary approximately in a range of 5 to 15 dB at different locations, which is not negligible especially in the context of small cells.

Furthermore, it can be observed from results that Scenario 3 and 4 have comparatively larger pathloss due to orientation of antennas in perpendicular streets. However, results of both scenarios are comparable with each other. Based on this analysis, it can be suggested that directing RS antennas in the largest power ray direction is optimal choice in order to achieve maximum antenna gain. However, mounting antennas in random directions is not a feasible solution from a deployment view point due to varying directions of the largest power ray at each RS location.

5.3 Impact of Relay Antenna Height

The characterization of wireless propagation channels incorporating specificities of the relay antenna architecture is required in order to design efficient relay-assisted wireless networks. Since RS consumes radio resource of the backhaul link, it is crucial to characterize the BS-to-RS propagation link. A possible solution is to favour as much as possible the BS-to-RS link by placing the RS in favourable radio locations. For this purpose, an important parameter of antenna height is investigated to find the optimal RS position thus maximizing the potential relay contributions. Although several models characterizing the relay architecture already exist such as IEEE 802.16 [47], 3GPP [4] and WINNER II [52] channel models, their applicability in a dense environment employing narrow-beam antennas is yet to be examined. Therefore, impact of the antenna height (in terms of pathloss) accounting influence of narrow beams at different RS locations in a square-cell topology is evaluated in this section.

5.3.1 Results and Analysis

RT-based results are extracted with narrow beam antennas at both sides (-45° polarization at the Tx and +45° at the Rx). In order to compute pathloss at a particular RS location, a single beam of the BS antenna is selected which provides maximum power at the investigated location.

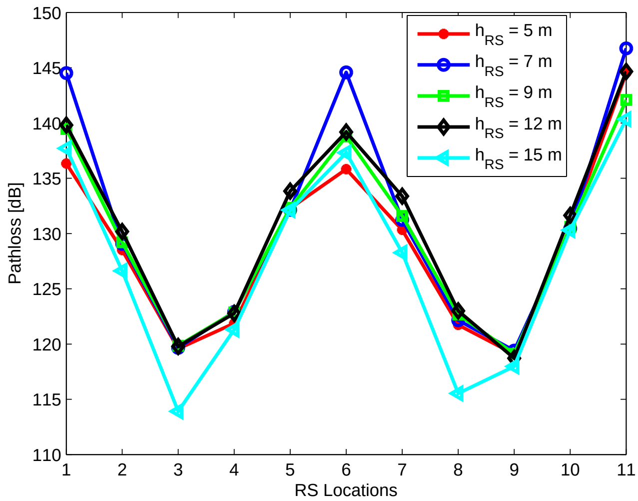

Figure 5.8: Pathloss curves of different RS heights at 11 RS locations in a square-cell topology

The BS-to-RS link pathloss is calculated by (4.9). For each RS location, pathloss is evaluated for five relay antenna heights (h_{RS}) and subsequently compared to each other. A comparison of results is shown in Fig. 5.8, where a little dependence of pathloss on h_{RS} is observed. The pathloss decreases within a range of 2 to 7 dB when the RS antenna is raised from 5 m to 15 m at different RS locations. In general, increase in height of the RS antenna corresponds to decrease in pathloss. In particular, a significant decrease in pathloss for $h_{RS} = 15$ m can be noted at RS_3 and RS_8 owing to the street tunneling effect. However, pathloss reduction for all other relay antenna heights is less significant.

To explain peculiarities and dependence of pathloss on h_{RS}, it is important to mention that the BS is considered over the rooftop, while all RS locations (forming BS-to-RS links) are in NLOS conditions. For this reason, the transmitted signals (rays) mostly propagate over the rooftop. However, when h_{RS} increases and approaches to the roof level, it causes the emergence of LOS or obstructed LOS conditions. Hence, received signals are less attenuated by the reflection, diffraction or scattering caused by the surrounding environment.

5.4 Conclusions

In this chapter, specificities of the relay antenna architecture have been characterized in order to design efficient relay-assisted wireless networks. Different BS-to-RS links have been investigated in terms of pathloss. First, a correct orientation of the relay antenna has been investigated by steering it in different directions in order to maximize antenna contributions at relay terminals. RT-based results have revealed that directing RS antenna in the largest power ray direction is the most appropriate choice with an approximate pathloss reduction of 10 to 15 dB. The improvement has been explained by the fact that due to narrow-beamwidth, antenna fails to capture some significant energy falling outside its main-lobe specially in dense scattering environments. Once the RS antenna is properly aligned in the direction of maximum MPCs, it contributes maximally to reduce pathloss.

Second, the influence of the RS (equipped with narrow-beamwidth antenna) height on pathloss has been investigated. RT-based results have indicated that pathloss generally decreases with height of the RS antenna. However, different impact has been observed at different RS locations in a simulated square-cell topology. When a BS-to-RS link was under deep NLOS conditions and longer propagation distance, difference in pathloss is not significant. Conversely, the dependence of pathloss on the RS height was noticeable for RS locations under OLOS conditions (i.e., streets). For the latter, decrease in pathloss was found in an approximate range of 2 to 7 dB when the RS height was raised from 5 m to 15 m at different RS locations. This improvement can mainly be attributed to the change in propagation (LOS or NLOS) conditions between BS and RS antennas. For example, with high RS location the received signal would be less attenuated by the diffraction or reflection caused by surrounding buildings.

CHAPTER 6

Multi-User Channel Models

Multi-User MIMO (MU-MIMO), is a key technology to achieve higher capacity in wireless networks. Whereas the number of multi-antenna terminals is constantly increasing in order to achieve rising demands of the capacity and throughput, this results in increased level of interference between users. This eventually reduces the network capacity and user throughput [104, 105]. However, interference-aware communication techniques enable to mitigate these performance impairments, but their effectiveness largely depends on the interfering channel behavior for different links, in particular upon the so-called spatial separation between multi-user channels. The capacity of MU-MIMO networks drops drastically owing to strong multi-user correlation (or interference) when the users are geographically clustered in a microcellular scenario [104]. Therefore, wideband MIMO channel measurements are conducted in a typical urban microcellular environment to relate the multi-user separation in the signal-space sense to their geographical separation. Instead of RT simulations performed for characterization of the BS and RS architecture in previous chapters, realistic measurements are conducted to characterize multi-user channels. Details of the measurement campaign I and II are provided in Section 6.1 and Section 6.2 respectively. Section 6.3 describes the data post-processing and parameter extraction procedure.

To characterize the spatial separation in MU-MIMO wireless propagation channels, Section 6.4 provides the definition of three metrics namely: (i) the Shadow Fading Correlation (SFC), (ii) the Channel Matrix Collinearity (CMC) and (iii) the Wideband Spectral Divergence (WSD). Each metric has a distinct signal processing aspect and correspond to time, spatial and delay domain respectively. The SFC has a large impact on the performance of cooperative communication schemes [42, 106–109], while the CMC is considered as a meaningful measure to characterize the spatial structure of MIMO wireless propagation channels [41, 110, 111]. Since both previous metrics are essentially narrowband, a third metric WSD [112], is included in this thesis to quantify the multi-user separation in a wideband sense.

Before characterizing multi-user separation, non-stationarity of MIMO propagation channels is evaluated in Section 6.5 because behaviour of the underlying channel can change due to movement of the Tx and/or Rx as well as the scatterers in the surrounding environment. Consequently, the WSS assumption may hold for short intervals but not infinitely. If these intervals are large enough, then wireless networks can take advantage to estimate the Channel State Information (CSI) at the Rx side and feed them back to the Tx side, so that it can adapt its transmission scheme accordingly. However, for short intervals such adaptive techniques are not feasible, as the CSI would be outdated when fed back to the Tx side, which could lead to degradation of the wireless network performance. Thus characterization of non-stationary wireless propagation channel is critical, e.g., for the design optimization of adaptive wireless networks. For this purpose, CMC is considered as the meaningful measure for the non-stationarity behaviour of MIMO propagation channels, based on the amount of change in their spatial structure over time.

Experimental results for multi-user separation are evaluated in Section 6.6 to quantify geographical minimum distances between multiple users. It includes the derived empirical models for three separation metrics. The similarities and differences between all metrics are highlighted through metric cross-correlation analysis in Section 6.7. Finally, Section 6.8 provides a conclusion and a discussion.

6.1 Measurement Campaign I

The outdoor measurement campaign aimed to characterize the non-stationarity of MIMO wireless propagation channels is presented in this section. It includes a brief description of the measurement setup, investigated scenarios as well as the used antennas.

6.1.1 Measurement Setup

The measurements were taken by means of a UCL-ULB Elektrobit MIMO channel sounder (presented earlier in Chapter 3), at a center frequency of 3.8 GHz with 200 MHz bandwidth. The frequency band is already being considered for LTE-Advanced [2] and expected to be used for beyond 4G wireless networks. The maximum transmit power is 23 dBm (i.e., 3.28 W). The Rx sensitivity is -88 dBm and a Rubidium clock reference in both Tx and Rx units ensured accurate timing and clock synchronization. The cycle rate (i.e., the rate at which the time-varying

Parameters	Values
Central frequency	3.8 GHz
Measurement bandwidth	200 MHz
Transmit power	23 dBm
Cycle rate	90.6 Hz
Code length	5.11 μs
Samples per chip	4
Chip frequency	100 MHz
Number of channels	16

Table 6.1: Channel sounder parameters for the measurement campaign I

complex CIR matrix was measured) is fixed to 90.6 Hz, which is well above the maximum Doppler spread given the pedestrian speed of the mobile unit (i.e., 1 m/s approximately). Two sets of fast switches are employed at the Tx and Rx, enabling MIMO channel measurements for 2×8 antennas, i.e., 16 links [92]. The main channel sounder parameters for measurement campaign I are summarized in Table 6.1.

6.1.2 Measured Scenarios

An extensive outdoor measurement campaign was carried out in a typical microcellular environment (campus area) located in Louvain-la-Neuve (Belgium). The investigated environment consists of three- to four-storey office buildings, parking lots and relatively narrow streets. It is further characterized by a small tree density and mostly pedestrian traffic. Measurements were carried out exclusively in pedestrian streets to avoid any disturbance from traffic, but the influence of walking-by people could not be eluded. For practical reasons, channel sounding took place between a mobile Tx unit placed on a trolley as shown in Fig. 6.1 and a fixed Rx unit taken as a BS. Two BS sites were chosen at the top of two four-storey buildings, Maxwell and Boltzmann, denoted as BS1a and BS2 each at an approximate height of 18 m above the local ground level. The reference direction of two BS antennas was always pointing towards the centre of measured areas as highlighted in Fig. 6.2.

The wideband CIR was measured in three separate areas: (i) around Parking-11 (Area 1), (ii) around Marie-Curie building (Area 2) and (iii) around Sainte-Barbe building (Area 3), as shown by red, blue and green colors respectively in Fig. 6.2. The approximate lengths of measured

Figure 6.1: The Tx (mobile) unit of the Elektrobit channel sounder on a trolley

routes in Area 1, 2 and 3 are 170, 230 and 300 m respectively. From BS1a site, all three measured areas are under NLOS conditions owing to dense building blockage, except for a small portion of Area 3, when the mobile Tx was in direct view of BS1a. However from BS2 site, measured areas are under a mix of LOS and NLOS conditions. Area 1 was mostly under LOS conditions, except blockage from dense trees, while different portions of Area 2 and 3 were also directly exposed to BS2. The average ground level in all areas varied from 1 to 5 m below and above the ground level at BS1a and BS2 (situated at relatively lower ground level) sites respectively. Three successive measurements (M1, M2 and M3) were carried out to enable adequate averaging. The trolley speed in all measurements was approximately 3 km/h (i.e., 1 m/s).

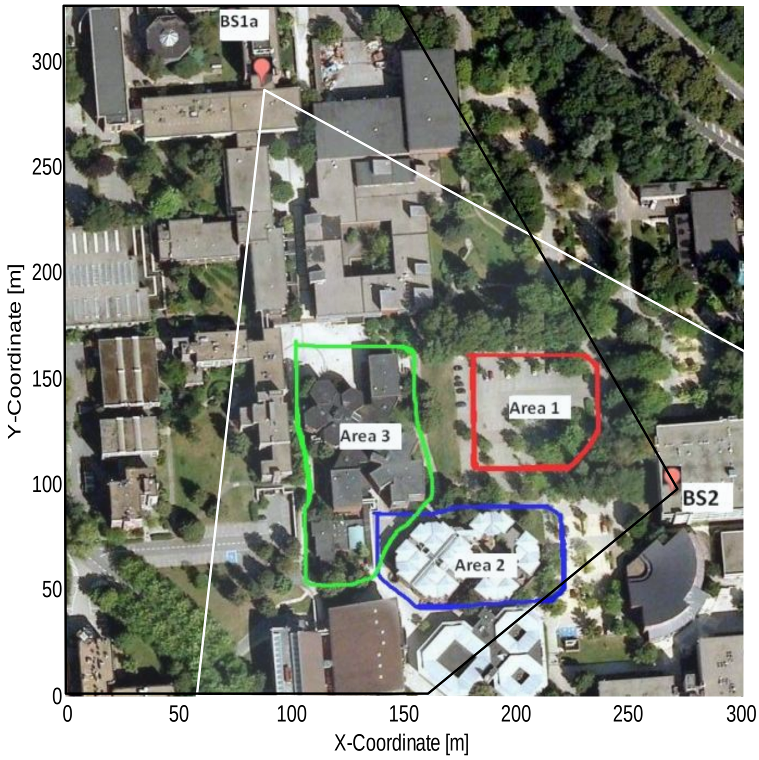

Figure 6.2: Area map of the outdoor measurement campaign I

6.1.3 Antennas

The BS antenna array consisted of a dual-polarized (horizontal and vertical) directional log-periodic antenna of 7-dBi gain, with 3-dB beamwidth of 80° in the azimuth plane and 70° in the elevation plane. It was mounted on a tripod platform located on the terrace (for BS1a) and above roof-top (for BS2) at an approximate height of 18 m (see Fig. 6.3). Typical radiation patterns of the log-periodic antenna in azimuth and elevation planes are shown in Fig. 6.4. The cross-polar isolation between both horizontal and vertical polarizations is above 20 dB.

At the MS side, an omnidirectional circular array (see Fig. 6.5) made of 8 vertically-polarized dipoles (gain of 2-dBi) was mounted at the height of 2 m on a fixed mast attached to a moving trolley. This global antenna configuration created therefore a 2×8 MIMO matrix for each MS-to-BS link.

Figure 6.3: The BS dual-polarized sectoral antenna mounted on a tripod platform: at BS1a site (left), at BS2 site (right)

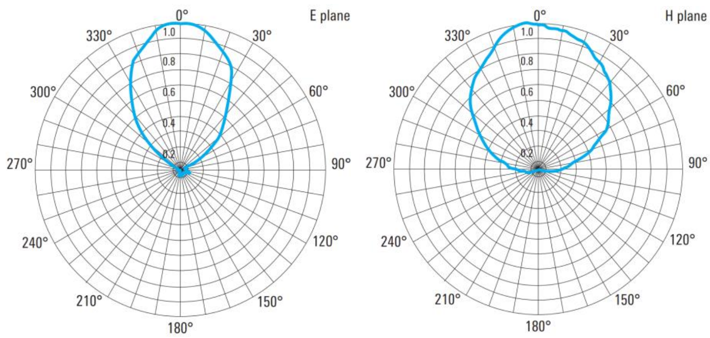

Figure 6.4: Radiation patterns of the BS sectoral antenna (measurement campaign I)

6.2 Measurement Campaign II

The objective of outdoor measurement campaign II was to characterize MU-MIMO wireless propagation channels. This section provides details of the measurement setup, used antennas as well as measured scenarios of this measurement campaign, with a special focus on differences from the previous one.

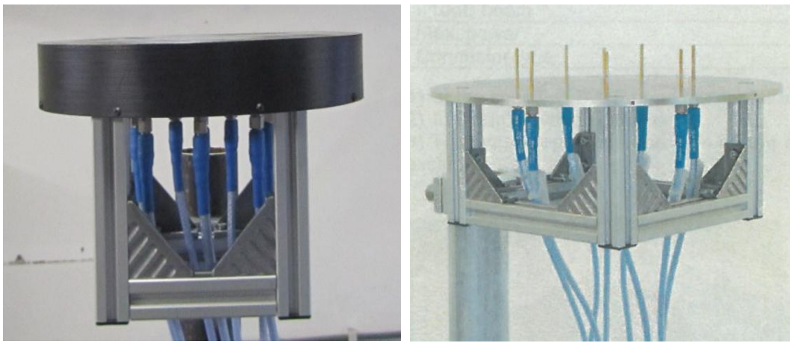

Figure 6.5: The MS omnidirectional circular array, seven elements at circle and one in the middle

6.2.1 Measurement Setup

The UCL-ULB Elektrobit MIMO channel sounder was again used for this measurement campaign, with key parameters being the same as described earlier in Section 6.1. The major difference was the BS antenna array, i.e., 2×4 dual-polarized ($\pm 45°$ slanted polarizations) planner array. The cycle rate was fixed to 30.2 Hz in this measurement campaign, which is above the maximum Doppler spread given the pedestrian speed of the mobile unit. Two sets of fast switches are employed at the Tx and Rx, enabling MIMO channel measurements for 8×8 antennas, i.e., 64 links [92]. The main channel sounder parameters for measurement campaign II are summarized in Table 6.2.

Parameters	**Values**
Central frequency	3.8 GHz
Measurement bandwidth	200 MHz
Transmit power	23 dBm
Cycle rate	30.2 Hz
Code length	5.11 μs
Samples per chip	4
Chip frequency	100 MHz
Number of channels	64

Table 6.2: Channel sounder parameters for the measurement campaign II

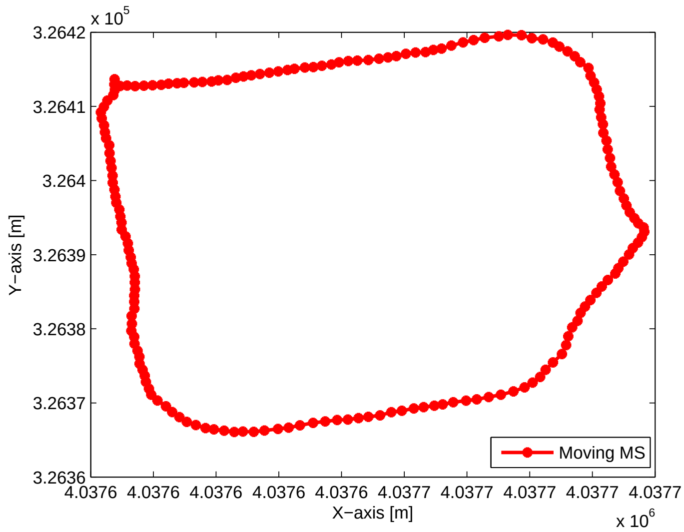

Figure 6.6: An example GPS map of the mobile unit

The sounder was further equipped with a Global Positioning System (GPS) receiver to enable a precise and accurate position of the moving mobile unit. Every second (at a rate of 1 Hz), the GPS receiver recorded the relative location of the mobile unit relative to the BS, whose position was stored. The objective is to localize the measurement route on a geo-referential map and assign to each measurement point Lambertian coordinates $(x, y) \triangleq \mathbf{r}$ (see Fig. 6.6 as an example).

6.2.2 Measured Scenarios

The outdoor measurement campaign II was again conducted in a typical microcellular environment (campus area) located in Louvain-la-Neuve (Belgium). Two BS sites were chosen at the top of two four-storey buildings, Maxwell and Mercator, denoted as BS1b and BS3 at height of 18 m and 20 m above the local ground level respectively. The first location was the same as the one described in Section 6.1.2. The respective orientation of BS antennas is highlighted in Fig. 6.7. The wideband CIR was measured in same three separate areas as described in Section 6.1.2: (i) around Parking-11 (Area 1), (ii) around Marie-Curie building (Area 2) and (iii) around Sainte-Barbe building (Area 3), as shown by red, blue and green colors respectively in Fig. 6.7. All three measured areas are under NLOS conditions owing to dense building blockage, ex-

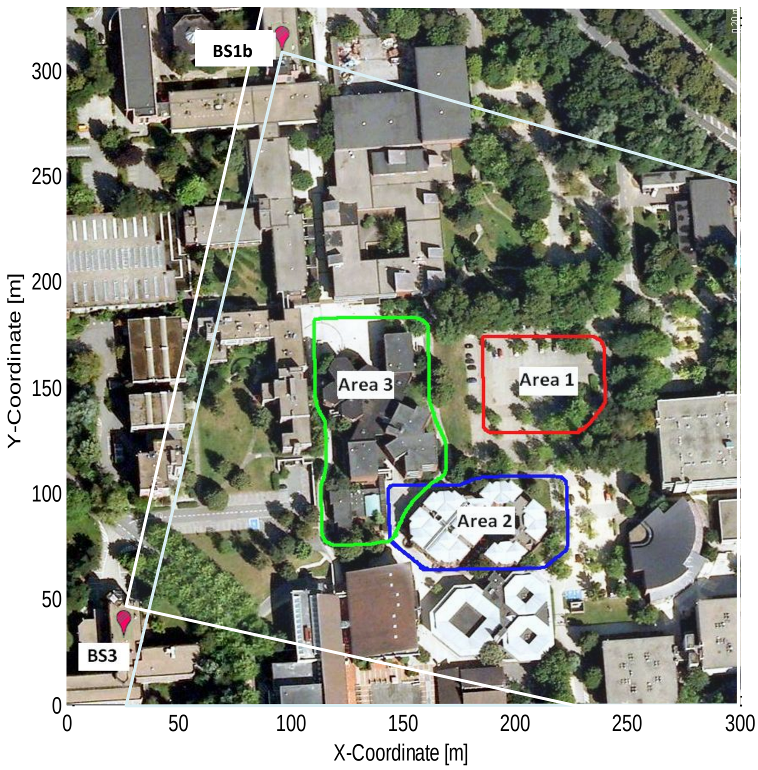

Figure 6.7: Area map of the outdoor measurement campaign II

cept for a small portion of Area 3, when the mobile Tx was in direct view of BS1b and BS3 (though at different positions with respect to each BS). The average ground level in all areas varied from 1 to 5 m below and above the ground level at BS1b and BS3 sites respectively.

Note that in order to investigate multi-user channel characteristics, multiple links should ideally be measured. A link is defined as the MIMO channel matrix from any position of the mobile unit to the BS. Simultaneously comparing multiple links would require a large number of synchronized mobile transmitters. As this is extremely difficult in outdoor environments, different users are assimilated to different transmit positions in a measured area. This comes to a so-called single-sounder sequential measurement technique, as highlighted in Section 3.2.1 [29, 41, 113]. Naturally, this technique bears two drawbacks:

- the environment might have changed between two distant measurement points: to minimize this risk, three successive measurements (M1, M2 and M3) were carried out to enable adequate checks (note that [41] has shown that such risk is not major in non-vehicular environments),
- absolute phase-synchronized multi-user measurements are impossible (depend upon the sounder phase stability). However, the investigated metrics are absolute phase-independent, so that this point is not an issue.

6.2.3 Antennas

A 2×4 dual-polarized ($\pm 45°$ slanted polarizations) planner array is used at the BS side. The array has approximately 6-dBi gain, with 3-dB beamwidth of 95°. It was mounted on a mast at the approximate height of 18 m for both BS1b and BS3 sites as shown in Fig. 6.8. The typical radiation patterns of the antenna in azimuth and elevation planes are shown in Fig. 6.9. The cross-polar isolation between both polarizations is above 20 dB.

At the MS side, again a uniform circular array (as detailed in Section 6.1.3) was used. The array was mounted at the height of 2 m on a fixed mast attached to a moving trolley.

6.3 Data Extraction Procedure

6.3.1 MIMO Channel Matrix and Received Power

As already mentioned, the MIMO complex CIR matrices $\mathbf{H}(\mathbf{r}, \tau)$ are obtained as the output of the channel sounder, where $\mathbf{r}$ designates the position in the area and τ is the delay. For $N_T \times N_R$ antennas, MIMO channel matrix can be represented as,

$$\mathbf{H}(\mathbf{r}, \tau) = \begin{bmatrix} h_{11}(\mathbf{r}, \tau) & h_{12}(\mathbf{r}, \tau) & \cdots & h_{1N_T}(\mathbf{r}, \tau) \\ h_{21}(\mathbf{r}, \tau) & h_{22}(\mathbf{r}, \tau) & \cdots & h_{2N_T}(\mathbf{r}, \tau) \\ \cdots & \cdots & \ddots & \cdots \\ h_{N_R1}(\mathbf{r}, \tau) & h_{N_R2}(\mathbf{r}, \tau) & \cdots & h_{N_RN_T}(\mathbf{r}, \tau) \end{bmatrix}$$

where each element of $\mathbf{H}$ denotes the $i-th$ Rx and $j-th$ Tx antenna link. The first line of $\mathbf{H}(\mathbf{r}, \tau)$ corresponds to links for the polarized element 1 at the BS, while the second line is the vector channel for

Figure 6.8: The BS dual-polarized array mounted on a mast: at BS1b site (left), at BS3 site (right)

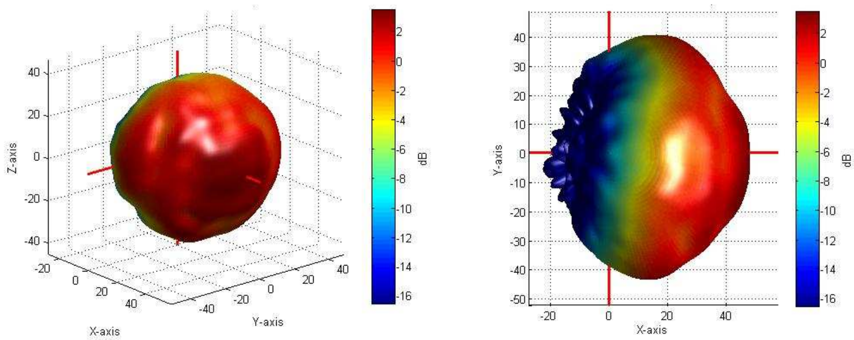

Figure 6.9: Radiation patterns of the BS dual-polarized array, element 1 only (measurement campaign II)

the polarized element 2 at the BS, and so on. For example, the first line of $\mathbf{H}(\mathbf{r}, \tau)$, corresponding to a cross-polar transmission (with the horizontally-polarized antenna at the BS) is denoted as $\mathbf{h}_{HV}(\mathbf{r}, \tau)$, while the second line is the co-polar vector channel denoted as $\mathbf{h}_{VV}(\mathbf{r}, \tau)$. As a first post-processing step, noise is removed from the data, using a threshold of 20 dB below the maximum peak power. The narrowband MIMO complex channel matrices are computed by integration in the delay domain,

$$\mathbf{G}(\mathbf{r}) = \int \mathbf{H}(\mathbf{r}, \tau)\, d\tau, \tag{6.1}$$

where elements of $\mathbf{G}(\mathbf{r})$ are denoted as $\mathbf{g}(\mathbf{r})$. Analogous to $\mathbf{H}$, the first line of $\mathbf{G}(\mathbf{r})$ is denoted as $\mathbf{g}_{HV}(\mathbf{r})$, while the second line is denoted as $\mathbf{g}_{VV}(\mathbf{r})$ when dual-polarized sectoral antenna is considered at BS. The instantaneous average received powers can be obtained by averaging over N channels.

In case of dual-polarized log-periodic antenna at the BS,

$$P_{HV}(\mathbf{r}) = \frac{1}{8} \left\|\mathbf{g}_{HV}(\mathbf{r})\right\|^2, \tag{6.2}$$

and

$$P_{VV}(\mathbf{r}) = \frac{1}{8} \left\|\mathbf{g}_{VV}(\mathbf{r})\right\|^2. \tag{6.3}$$

For dual-polarized planner array at the BS side,

$$P(\mathbf{r}) = \frac{1}{64} \left\|\mathbf{g}(\mathbf{r})\right\|^2. \tag{6.4}$$

6.3.2 Shadow Fading

Shadow fading, also known as shadowing, is defined as the large-scale power fluctuation around its overall mean (detailed in Section 2.2.2). The narrowband received power calculated in (6.4) is actually the combination of small-scale fading components, shadow fading and pathloss. To obtain SF, two operations are successively carried out. The small-scale fading part is first removed by applying a sliding window of length $W = 40\lambda$ over the whole measured area. This corresponds to a distance of approximately 3 m at the maximum trolley speed of 3 km/h. This provides an intermediate parameter given as,

$$\tilde{P}(\mathbf{r}) = \frac{1}{W} \sum_{\mathbf{r}'=\mathbf{r}-W/2}^{\mathbf{r}'=\mathbf{r}+W/2} P(\mathbf{r}'). \tag{6.5}$$

Replacing $P(\mathbf{r}')$ by $P_{HV}(\mathbf{r}')$ or $P_{VV}(\mathbf{r}')$ in (6.5) will give $\widetilde{P}_{HV}(\mathbf{r})$ or $\widetilde{P}_{VV}(\mathbf{r})$ respectively. The result of such process is illustrated in Fig. 6.10 as an example. Note the slight abuse of notation, as W is scalar while $\mathbf{r}$ is a vector designating the position. A careful selection of W is critical.

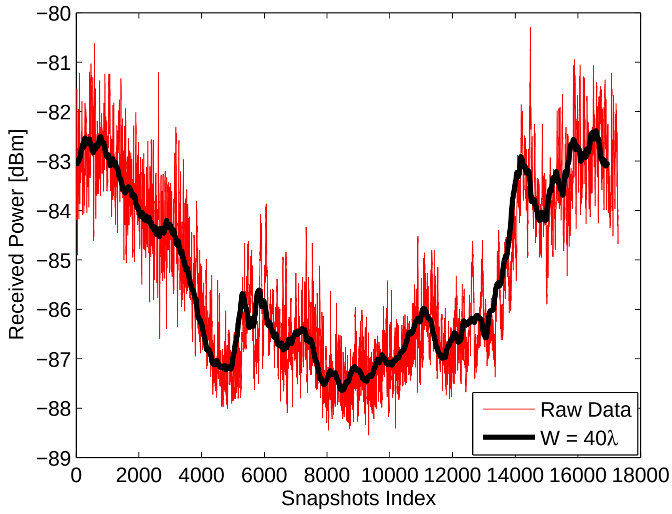

Figure 6.10: An example of smoothing out small-scale fading

If W is chosen too short, small-scale fading is not fully filtered out, while a too large value for W results in shadow fading being smoothed out. In the literature, W is mostly considered in the range of 20 λ - 40 λ [109, 114, 115].

In a second step, the pathloss effect is removed by applying a linear regression to the power expressed in dB as a function of the distance to the BS and removing the linear trend from $\tilde{P}(\mathbf{r})|_{dB}$. This eventually yields SF values denoted as $S(\mathbf{r})$ in dB scale. Since these values are non-uniformly spaced over distance (as the speed was not fully constant), they are resampled and uniformly interpolated so that all measurement points on each route are equidistant. Histograms of estimated SF are further analyzed to verify their Gaussian distribution (in dB scale).

6.3.3 Correlation Matrices

The complex spatial correlation matrices at the MS (transmit) side can be estimated, considering the co-polar link only (from the measurement campaign I), by [1] [6, 116],

$$\mathbf{R}_{MS,VV}(\mathbf{r}) = \frac{1}{W}\sum_{\mathbf{r}'=\mathbf{r}-W/2}^{\mathbf{r}'=\mathbf{r}+W/2} \mathbf{g}_{VV}(\mathbf{r}')^H \mathbf{g}_{VV}(\mathbf{r}'), \tag{6.6}$$

and similarly for $\mathbf{R}_{MS,HV}$, replacing $\mathbf{g}_{VV}$ by $\mathbf{g}_{HV}$.

On the BS (receive) side, the complex spatial correlation matrices can be extracted, considering all links in case of the measurement campaign II, by [6, 116],

$$\mathbf{R}_{BS}(\mathbf{r}) = \frac{1}{W}\sum_{\mathbf{r}'=\mathbf{r}-W/2}^{\mathbf{r}'=\mathbf{r}+W/2} \mathbf{g}(\mathbf{r}')\mathbf{g}(\mathbf{r}')^H, \tag{6.7}$$

where the choice for W is not trivial, as discussed in the previous section. Similar to SF extraction, correlation matrices are estimated using a window of length $W = 40\lambda$ (i.e., approximately a distance of 3 m) over which the channel statistics are assumed to remain constant.

6.3.4 Power Delay Profile

The Power Delay Profiles (PDPs) at each measurement location are computed by a double space-position power-average of the complex CIRs, i.e., over all channels and over a sliding window of size $W = 40\lambda$,

$$\mathcal{P}(\mathbf{r},\tau) = \frac{1}{NW}\sum_{\mathbf{r}'=\mathbf{r}-W/2}^{\mathbf{r}'=\mathbf{r}+W/2} \left\|\mathbf{h}(\mathbf{r}',\tau)\right\|^2. \tag{6.8}$$

similarly $\mathcal{P}_{HV}(\mathbf{r},\tau)$ and $\mathcal{P}_{VV}(\mathbf{r},\tau)$ can be computed by replacing $\mathbf{h}(\mathbf{r}',\tau)$ in (6.8) by $\mathbf{h}_{HV}(\mathbf{r}',\tau)$ and $\mathbf{h}_{VV}(\mathbf{r}',\tau)$ respectively. Note that $N = 8$ for co- and cross-polar links in the measurement campaign I, while $N = 64$ is taken for the measurement campaign II.

6.4 Multi-User Separation Metrics

6.4.1 Shadow Fading Correlation

The Shadow Fading Correlation (SFC) is defined as the correlation between multi-user shadow fading levels [32]. If the shadow fading of

[1] $(.)^H$ denotes hermitian transpose

multi-user links is highly correlated, the potential of inter-user interference is high and multi-antenna gains may not be obtainable. Let S_1 and S_2 represent the SF of two links (i.e., users) in the logarithm domain (dB). The SFC coefficient ($\rho_{S,12}$) of such pair of links can be defined as [32],

$$\rho_{S,12} = \frac{E\{S_1 S_2\}}{\sigma_{S_1}\sigma_{S_2}}, \tag{6.9}$$

where σ_{S_n} is the standard deviation of S_n.

6.4.2 Channel Matrix Collinearity

While SFC is an important parameter in resource management [6], it does not provide any information on the alignment between the subspaces of different links. Therefore, a second metric geared towards matrix subspace alignment is required: the CMC measures the amount of change in the spatial structure of two correlation matrices (as described previously in Section 2.3.1.3). It actually compares the subspaces of two complex valued matrices and assess their similarity. The distance between two matrices $\mathbf{R}_1$ and $\mathbf{R}_2$ of same dimensions can be quantified by the collinearity as [110, 111],

$$c_{\mathbf{R},12} = \frac{\mathrm{tr}\{\mathbf{R}_1\mathbf{R}_2\}}{\|\mathbf{R}_1\|_f\|\mathbf{R}_2\|_f}, \tag{6.10}$$

where $\mathrm{tr}\{.\}$ and $\|.\|_f$ are respectively the trace and the Frobenius norm of a matrix. The CMC ranges between zero (no collinearity, when the correlation matrices differ to a maximum extent) and one (full collinearity, when the correlation matrices are equal up to a scaling factor) [6]. In other words, the CMC measures the degree of orthogonality between correlation matrices of size $n \times n$ in the $n \times n$ dimensional space. When the signal spaces of correlation matrices overlap, the CMC increases due to the higher trace of the product. Note that this distance metric is invariant against fading and pathloss as long as the multipath structure remains the same [41, 110].

CMC is a meaningful measure to check the validity of stationarity assumptions. The changes in the spatial structure of wireless channels (correspond to small values of CMC) can reduce the performance of MIMO transmission schemes because of out-dated channel statistic [41, 104, 110]. Such changes can appear even in short distances which can be characterized by the CMC. On the other hand, when the spatial structure of correlation matrices is separable in a MU-MIMO system. The users can be scheduled jointly, thus minimizing the interference and the system performance tends to increase [41, 110].

6.4.3 Wideband Spectral Divergence

The separation metrics defined so far are essentially narrowband. To account for the delay domain and compare power spectral densities, a third correlation metric is introduced [117]. The wideband spectral divergence (WSD) measures the distance between strictly positive, non-normalized spectral densities such as power delay spectrum [112, 117, 118]. This metric enables better characterization of the correlation in wideband channels. The WSD between two links (1 and 2) can be written as [6],

$$\zeta = \log\left\{\frac{1}{L^2}\left[\sum_{\tau}\frac{\mathcal{P}_1(\tau)}{\mathcal{P}_2(\tau)}\right]\left[\sum_{\tau}\frac{\mathcal{P}_2(\tau)}{\mathcal{P}_1(\tau)}\right]\right\}, \tag{6.11}$$

where $\mathcal{P}_m(\tau)$ is the (discrete) power delay spectrum of link m, and L being the number of samples in the delay domain. In an MU-MIMO system, a different PDP is obtained for each link (user). Subsequently, they are compared through the WSD metric to assess the correlation. Intuitively, ζ characterizes the flatness of $\mathcal{P}_1/\mathcal{P}_2$. Mathematically, it can be shown that it is related to the logarithm of the ratio of the arithmetic mean over the harmonic mean of $\mathcal{P}_1/\mathcal{P}_2$. If both spectra are equal (up to a multiplicative constant), then $\zeta = 0$ [6, 112].

6.5 Non-Stationarity of Polarized MIMO Channels

For the uplink communication, the non-stationarity behaviour of the mobile terminal becomes crucial as assumption of having perfect knowledge of the channel statistics over time may not be valid. Similarly, for downlink communication, the stationarity of the spatial structure at the BS is crucial for the network performance. Note that in a typical fixed BS and moving user wireless network, advanced transmission schemes for the uplink will face more severe performance degradations due to non-stationarity of the channel than for the downlink [41, 110]. Therefore, in this section, only the non-stationarity of measured wireless channels on the transmit side (i.e., MS equipped with 8-element circular array) is characterized based on the measurement campaign I. For this purpose, the time-dependant behaviour of the spatial structure of MIMO channels is characterized to show significant changes due to movement of the Tx unit (and the surrounding scattering environment) along three measured areas. CMC-based analysis of multi-user separation at the BS side using the measurement campaign II will be presented in the next section.

6.5.1 Estimation of Stationarity

The time-variant stationarity regions can be identified by using the CMC metric which tells the amount of change in the spatial structure of adjacent spatial correlation matrices. If two spatial correlation matrices are strongly correlated, then the underlying fading process has similar statistical properties (thus MIMO channel can be considered as stationary). In other words, signals transmitted at two different locations (yet within same stationarity region) experience a correlated spatial structure of underlying MIMO propagation channels. In this context, the estimation of stationarity regions helps to assess the validity of the commonly used WSS assumption in signal processing algorithms.

To illustrate, Area 1 (Parking-11) is considered as an exemplary area to estimate CMC as a function of distance. This area can be characterized as under NLOS conditions from BS1a, while under LOS conditions from BS2 (except blockage through dense trees). The estimated CMC at the MS side as a function of distance shifts for VV and HV links is displayed in Fig. 6.11. Results suggest that CMC values for VV and HV links are similar for both BSs, i.e., the spatial structure of MIMO propagation channels is almost similar. The time-variant stationarity regions, where the spatial structure of the MIMO channel is relatively constant, can easily be identified. Beyond these stationarity regions, significant variations in the spatial structure of the MIMO channel can be observed which correspond either to non-stationarity regions or to other stationarity regions. Note that CMC values significantly changes for BS1a (both VV and HV) links which translate into relatively larger stationarity regions mainly due to NLOS conditions as well as the scattering environment. On the contrary, relatively less variations of CMCs is found for BS2 (both VV and HV) links due to a strong LOS component between the moving Tx and BS2. It is important to mention that the appearance and disappearance of stationarity regions is highly dependent on the scattering environment in the immediate proximity of

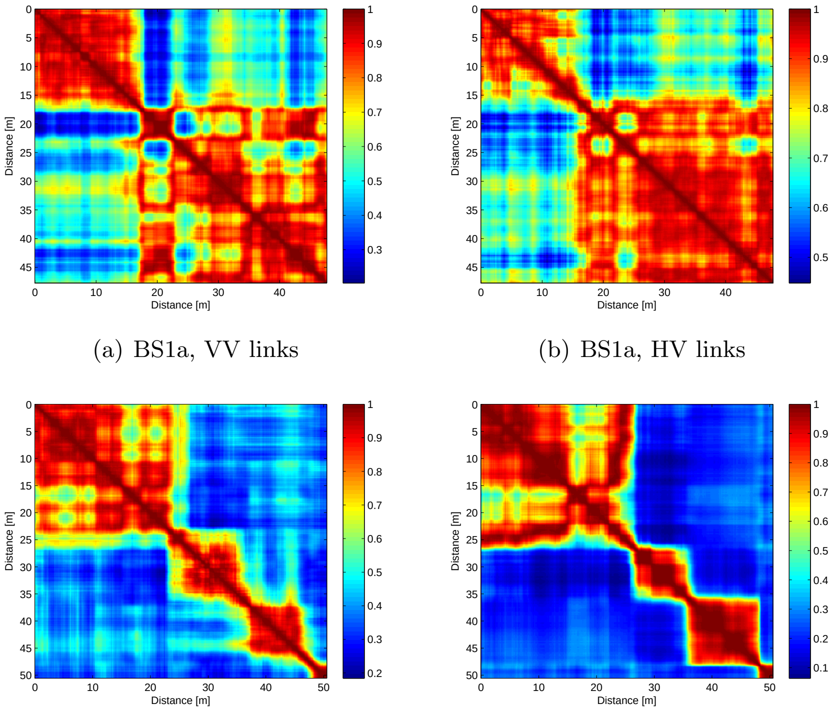

(a) BS1a, VV links

(b) BS1a, HV links

(c) BS2, VV links

(d) BS2, HV links

Figure 6.11: Estimation of CMC-based stationarity regions at the MS side (from BS1a and BS2) for VV (left) and HV (right) links in measured Area 1 (Parking-11)

the moving terminal.

6.5.2 Stationarity Distances

The time-variant stationarity distances are estimated using the experimental data obtained from the measurement campaign I. The stationarity distance (D_s) is defined as the maximum distance over which the CMC remains above a certain threshold. A typical threshold value $c_{thesh} = 0.8$ is considered to detect significant variations in the spatial structure of MIMO channels, as usually taken in the literature [111,116].

The CMC of all link pairs is computed and averaged over a bin length of 5 m to get smooth CMC curves. Fig. 6.12 depicts CMC variations as a function of distance for separate areas as well as all-areas

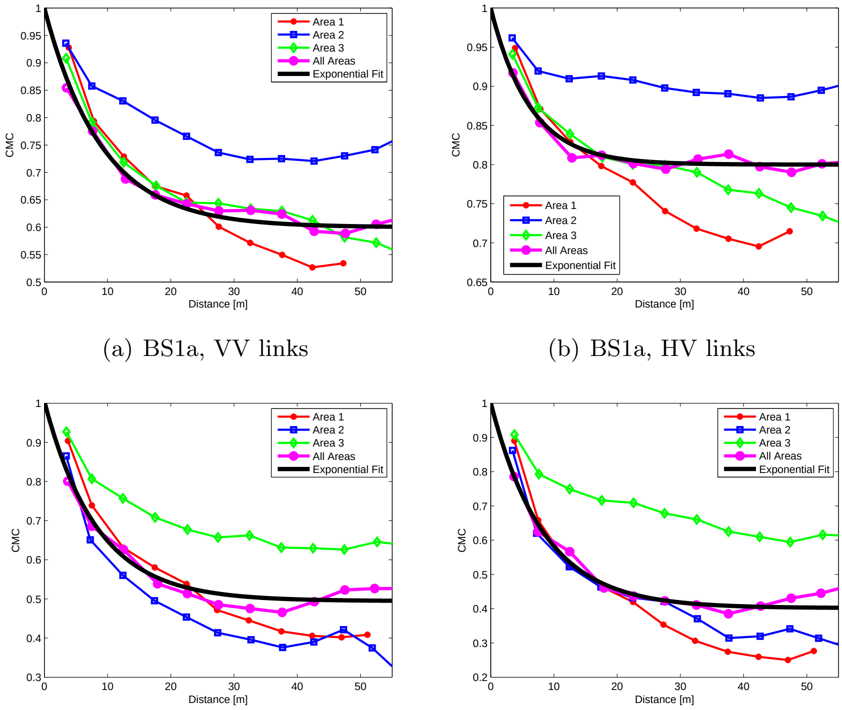

(a) BS1a, VV links

(b) BS1a, HV links

(c) BS2, VV links

(d) BS2, HV links

Figure 6.12: CMC variations as a function of distance and average fitted curve for VV (left) and HV (right) links

together. Results for both VV and HV links are separately plotted for BS1a and BS2. Note that propagation conditions in all measured areas are different with respect to location of BS1a and BS2. This is the reason that CMC variations are different in each area. For BS1a, Area 2 exhibits lower collinearity values than other two areas for both (VV and HV) links because of deep NLOS conditions. However, on the contrary, the same area shows higher CMC values for BS2 links due to mixture of LOS and NLOS conditions. Similarly, Area 3 is characterized differently with respect to BS1a and BS2, thus showing variations of the CMC differently.

By applying the defined threshold level to CMC variations, computed D_s values are summarized in Table 6.3 for both BS1a and BS2. The stationarity distances vary in a range of 5 to 23 m. Note that significant variations in the spatial structure of MIMO channels become

	BS1a		BS2	
	VV	HV	VV	HV
Area 1	8	17	6.5	5.5
Area 2	17	-	5.5	5
Area 3	7.5	22	8.5	6.5
All-areas	6.5	23	5	5

Table 6.3: Values of the sationarity distance (D_s) for VV and HV links from BS1a and BS2

fairly constant for distance larger than 20 to 25 m. For BS2 links, relatively shorter stationarity distances are found in all areas, mostly due to stronger LOS component. However, comparable stationarity distances are found for both VV and HV links. On the other hand, relatively longer stationarity distances are found for BS1a links (specially for HV links) due to a homogeneous scattering environment as nearly all measured areas come under NLOS conditions with respect to BS1a. Nevertheless, generally D_s values are comparable for both BSs on a magnitude scale, except large values of HV BS1a's links.

6.6 Multi-User Separation Results and Analysis

In this section, experimental results based on previously defined multi-user separation metrics are analysed and quantified. This analysis is performed for the data collected during the measurement campaign II (detailed in Section 6.2).

6.6.1 Shadow Fading Correlation

Based on the measured data, the SFC is characterized as a function of two important parameters, i.e., the multi-user distance and the angle difference. The respective definitions are illustrated in Section 2.3.1.3 (see Fig. 2.6).

6.6.1.1 Distance Difference Characterization

The SFC can be computed by (6.9) for all possible link pairs (i, j) and reported on a graph as a function of their distance difference $\Delta d_{ij} \triangleq$

$\|\mathbf{r}_i - \mathbf{r}_j\|$. The results cover link pairs in a single area as well as cross-area links. The average curves (obtained through averaging over all three runs M1 to M3 and all link pairs) are represented in Fig. 6.13, with respect to BS1b and BS3. As suggested by Fig. 6.13, the SFC curves as a function of the multi-user distance are fitted by a decaying exponential function,

$$\rho_S(\Delta d) = e^{-\Delta d/\Delta d_0}, \tag{6.12}$$

where Δd_0 is the multi-user separation distance defined as the distance for which the SFC coefficient decreases to e^{-1} [119, 120]. The estimated separation distances are summarized in Table 6.4. The difference between BS1b and BS3 results is only the decaying slope of exponential curves, with a steeper decrease for BS1b links, which corresponds to smaller Δd_0 values. The difference might be stemming from orientation of buildings with respect to BS1b and BS3 locations. Naturally, strength of link correlation varies depending upon the partial- or full-overlap of common shadowing objects observed by the user, which corresponds to smaller or higher Δd_0 values accordingly.

When investigating individual areas, parameter Δd_0 is lower for Area 1, which might be caused by the open area of Parking-11. Indeed, Δd_0 is intuitively related to the size of the shadowing obstacles. In Area 1, the shadowing obstacles are mostly local smaller objects (cars, trees) which represent homogeneous scattering environment, causing lower values of Δd_0 than in Area 2 where high buildings are responsible for shadow fading. Note that Area 3 contains mix of LOS and NLOS locations, resulting into smaller Δd_0 values compared with Area 2 which has only deep NLOS locations for both BS1b and BS3. This trend is similar to WINNER II results, where comparatively smaller values are reported for LOS scenarios than NLOS [52]. Moreover, experimental results also show that the SFC coefficients become negligible for distance differences around 25 to 30 m.

When investigating the correlation between multiple cross-area links, separation distances of 12.1 m and 11.4 m are estimated for BS1b and BS3 respectively. With this analysis, a slightly larger value is observed for BS1b compared with individual areas. This might be due to increased number of common shadowing obstacles (e.g., buildings) over all-areas. A large number of measurements showed that SFC-based distance separations range from about 10 to 50 m in urban networks [52, 109], with WINNER II channel model (B1) recommending a separation distance of 12 m for Manhattan-like scenarios in NLOS conditions [52].

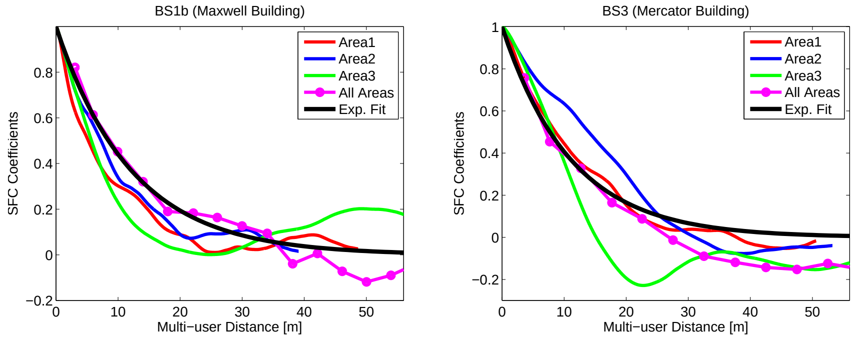

Figure 6.13: Distance characterization of SFC with respect to BS1b (left) and BS3 (right)

Areas	Δd_0 [m]		$\Delta\theta_0$ [°]				β	
			at e^{-1}		fit def.			
	BS1b	BS3	BS1b	BS3	BS1b	BS3	BS1b	BS3
Area1	7.7	12.2	2.4	2.0	3.1	3.8	15.7	26.7
Area2	9.4	18.0	1.9	3.4	3.8	6.3	29.8	15.7
Area3	7.5	9.9	2.0	4.0	2.2	9.5	12.5	14.1
All-areas	12.1	11.4	2.8	3.7	5.4	6.0	17.9	13.1

Table 6.4: SFC-based multi-user separation distances and angles

6.6.1.2 Angular Difference Characterization

The angle of arrival seen from the MS to the BS, denoted as θ, has also a significant impact on the SFC [106,108,109]. Strong correlation coefficients (0.6 to 0.8) being reported for small angular difference around 10° to 15° [106, 109], but dropping rapidly for larger separations. For each measured position of the moving MS, θ is computed with the help of GPS data points and SFC data are subsequently analyzed as a function of the angular difference $\Delta\theta_{ij} = |\theta_i - \theta_j|$. The average SFC coefficients calculated for each area are displayed as a function of $\Delta\theta$ in Fig. 6.14 for BS1b and BS3 links. To define multi-user separation angle, one may use the angle difference for which the SFC coefficients decrease to e^{-1}, or fit the various SFC curves as a function of angle difference with a damped sine function,

$$\rho_S(\Delta\theta) = e^{-\Delta\theta/\Delta\theta_0}.\cos(\beta\Delta\theta), \tag{6.13}$$

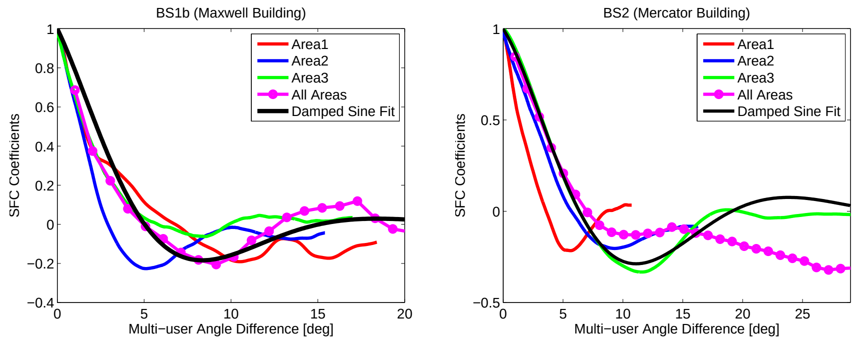

Figure 6.14: Angular characterization of SFC for BS1b (left) and BS3 (right) links

where $\Delta\theta_0$ is the multi-user separation angle and β is the angular frequency factor. The estimated $\Delta\theta_0$ values obtained from both definitions along with corresponding β values are summarized in Table 6.4 for BS1b and BS3 links. Note that the term "damped sine" includes all sine, cosine and intermediate functions, irrespective of their initial phase value.

It appears again that the decaying slope of SFC curves as a function of angle difference is slightly higher for BS3 than BS1b links, corresponding to relatively larger $\Delta\theta_0$ values. In fact the number of common propagation paths between multi-user links increases when the angle difference $\Delta\theta$ is small. Thus, links are affected in a similar way by the large obstacles, resulting in a strongly correlated SF. The similar structure of buildings and heights can also be a reason for high SFC coefficients. Both definitions provide comparable results (i.e., similar order of magnitude) for separate as well as all-areas together analysis. However, contrary to the distance characterization, Area 2 has no clear distinction compared with other areas in terms of angular separation, probably due to different investigated dimension (which may have different SF) than that of distance. Note that in measured areas, a small angular difference does not necessarily translate to a short distance difference, although a large angle difference always corresponds to a large distance difference.

Estimating all-areas together like distance characterization, global values of $\Delta\theta_0$ are found 2.8 and 3.7 (using the e^{-1} definition) and 5.4° and 6.0° (using the damped sine fit) for BS1b and BS3 links respectively. A number of studies [38, 103, 106, 108, 109] have reported strong correlation coefficients in the range of 0.6 to 0.8 for $\Delta\theta < 10°$ generally. However, accurate $\Delta\theta_0$ values are not found for multi-users having smaller angular difference $\Delta\theta$.

6.6.1.3 Heuristic Explanation

A heuristic explanation for sine damped fit in angular characterization of SFC is that measured areas can be virtually categorized in several sub-areas (or chunks) with similar characteristics (i.e., buildings and streets). It is mentioned earlier in Section 6.2 (see Fig. 6.7), there are several buildings and streets with different heights and widths, specially Area 1 is an open area (i.e., a car parking with smaller objects). The shadow fading within a certain area can be correlated, however the multi-user separation distance or angle is intuitively related to the size of the shadowing obstacles. Larger shadowing obstacles result in larger separations. The shadowing in the center of an obstacle can be quite different than at boundary of the adjacent obstacle, this could be the possible reason for the negative correlation values. In addition, there can also be some similarities between adjacent obstacles, in fact some measured parts of Area 2 and Area 3 are common.

Assuming a scenario that the moving Tx passes from one obstacle to another by crossing a virtual boundary, SFC decreases when it is moving out of an obstacle and entering the virtual boundary. However, SFC increases when moving Tx enters to the adjacent obstacle which is similar to the previous one. This entrance and leaving of moving Tx to different obstacles provides the damped sine function specially for angular characterization of SFC. Note that small angular difference between multi-users does not necessarily mean a short distance difference, although a large angle difference always corresponds to a distance difference. Indeed, multi-user distance and angular difference are two different dimensions to look at the measured area. This might explain the reason that we do not have clear damped sine functions in case of distance characterization of SFC except Area 3 with respect to BS3.

6.6.2 Channel Matrix Collinearity

Several antenna combinations at the BS side are investigated to characterize multi-user separation distances by following the nomenclature shown in Fig. 6.15. Where 4A-3S, for example, denotes four antennas with three unique sets like $\{1, 2, 3, 4\}$, $\{3, 4, 5, 6\}$ and $\{5, 6, 7, 8\}$, and so on. For each antenna set, CMC values are calculated through (6.10) for all possible link pairs in three areas together and followed by an average over distance with a bin length of 5 m. Subsequently, each CMC curve is fitted with an exponential function given as,

$$c_{\mathbf{R}} = \alpha(\beta + e^{-\Delta d/\Delta d_0}), \tag{6.14}$$

where α and β are constants used to adjust the floor level of the fitting curve.

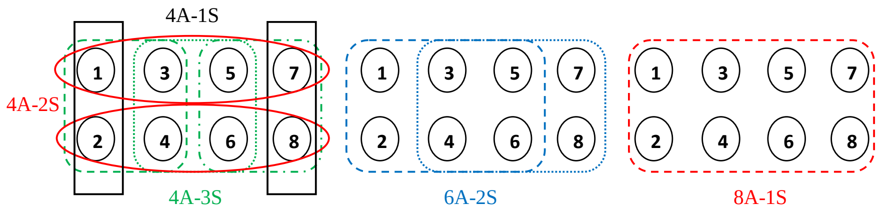

Figure 6.15: Multiple antenna sets with respect to antenna spacing

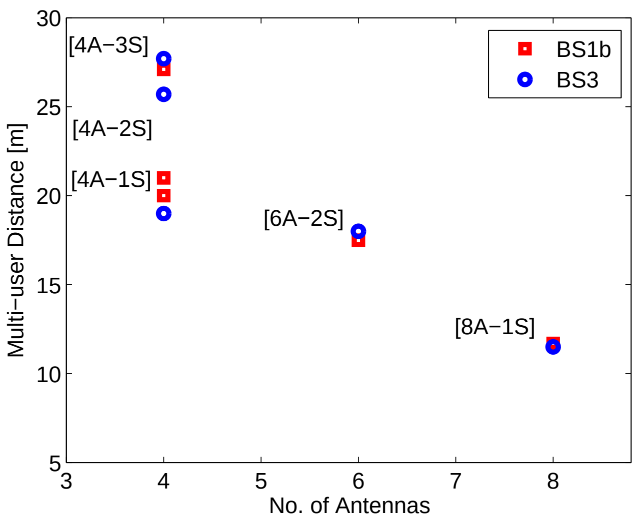

Figure 6.16: CMC-based multi-user separation distances as a function of the BS array size for BS1b and BS3 links

To define CMC-based separation distances, we have used a fixed threshold value 0.8, usually chosen in the literature [111, 116]. The Δd_0 values (averaged over all identical antenna sets to attain a distinct value

Antenna Sets	Avg. Δd_0 [m]	
	BS1b	BS3
4A-1S	20.0	19.0
4A-2S	21.0	25.7
4A-3S	27.1	27.7
6A-2S	17.5	18.0
8A-1S	11.7	11.5

Table 6.5: CMC-based multi-user separation distances

for each combination) as a function of number of antennas are depicted in Fig. 6.16 for both BS1b and BS3. In addition, averaged values of Δd_0 obtained from the above definition are listed in Table 6.5. A fairly good match of estimated values is found between both BSs, except 4A-S2 where values are slightly mismatched. In general, Δd_0 values decrease by increasing the array size, irrespective of the BS location.

Note that antenna sets with larger antenna spacing provide short separation distances. For instance, 4A-1S (a set with two elements from each corner) has smaller Δd_0 values than 4A-2S and 4A-3S for both BSs, implying that large antenna spacings render lesser correlation between channels. Similarly, 4A-2S (two sets of two separate horizontal lines) have slightly shorter distances than 4A-3S (three sets with least antenna spacings) for both BS1b and BS3. Moreover, CMC-based separation distances with 8A-1S (8 antenna set) are much closer to the SFC-based values for all-areas links. This might be an indication that the 0.8 threshold empirically recommended by [116] is actually relevant. It is also observed that significant variations in the spatial structure of MIMO channels become fairly constant for distance differences larger than 40 to 45 m.

6.6.3 Wideband Spectral Divergence

The WSD plots are shown in Fig. 6.17 for BS1b and BS3 links. Since the WSD measures the difference rather than the similarity, the curves exhibit an increasing trend with distance difference. Note that the WSD is a non-bounded metric, by contrast to SFC and CMC. Analogous to CMC, WSD values are extracted for all possible link pairs (user) in the measured scenarios by using (6.11). The WSD values are then averaged over a bin length of 5 m to obtain smooth WSD curves plotted in Fig. 6.17. The divergence for BS1b remains smaller than BS3 links. It corre-

Area	Δd_0 [m]	
	BS1b	BS3
All-areas	15.8	12.5

Table 6.6: WSD-based multi-user separation distances

sponds to higher WSD-based separation distances for BS1b associated links.

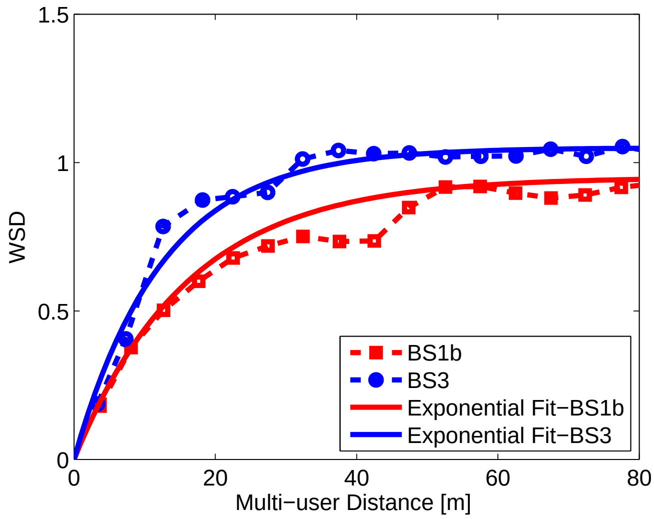

Figure 6.17: WSD and fitting curves for BS1b and BS3 links

To define a WSD-based multi-user separation distance, WSD plots as a function of distance are fitted with an exponential curve,

$$\zeta = \alpha(\beta - e^{-\Delta d/\Delta d_0}), \tag{6.15}$$

where α and β enable to adjust the floor level. Fitting based estimated values of Δd_0 are reported in Table 6.6.

In addition, when fitting the averaged curves, the following values are estimated: $\Delta d_0 = 15.8$ m and 12.5 m; $\alpha = 0.95$ and 1.05 for BS1b and BS3 links respectively, while $\beta = 1$ for both links.

Areas	**Meas.**	$\langle SFC, CMC\rangle$		$\langle SFC, WSD\rangle$		$\langle WSD, CMC\rangle$	
		BS1b	BS3	BS1b	BS3	BS1b	BS3
Area 1	M1	0.27	0.34	-0.70	-0.77	-0.29	-0.27
	M2	0.25	0.31	-0.75	-0.73	-0.25	-0.26
	M3	0.23	0.35	-0.54	-0.76	-0.37	-0.33
Area 2	M1	0.58	0.35	-0.68	-0.61	-0.43	-0.33
	M2	0.51	0.28	-0.63	-0.70	-0.32	-0.30
	M3	0.36	0.25	-0.52	-0.66	-0.46	-0.35
Area 3	M1	0.41	0.44	-0.49	-0.79	-0.38	-0.54
	M2	0.28	0.36	-0.58	-0.78	-0.28	-0.47
	M3	0.25	0.27	-0.54	-0.81	-0.23	-0.36

Table 6.7: Emprical cross-correlation of evaluated metrics for three areas separately

6.7 Metric-Correlation Analysis

In order to evaluate the joint behaviour of three metrics, the cross-correlations between SFC, CMC and WSD metrics are investigated. As an example in Fig. 6.18, the scatter plots of CMC (top) and WSD (middle) as a function of SFC and CMC (bottom) as function of WSD, are drawn. The linear regression fitted to the data is also plotted. In this analysis, all possible link pairs of each run (M1 to M3) in all areas are taken separately for both BS1b and BS3 links. Non-surprisingly, results show a positive correlation between CMC and SFC, and a negative correlation between SFC and WSD, and between CMC and WSD. The estimated cross-correlation coefficients are summarized in Table 6.7. This suggests that although all metrics concern a different signal processing aspect, if two users are not separated on one aspect, their respective links will likely not be well separated on all other aspects. It can also be observed that the cross-correlation of SFC and WSD is stronger than other metrics regardless of the area or the BS position.

6.8 Conclusions

In this chapter, first the non-stationarity behaviour of MIMO wireless propagation channels has been investigated in urban microcellular networks using experimental data obtained from the measurement campaign I. Experimental results have showed average stationarity distances

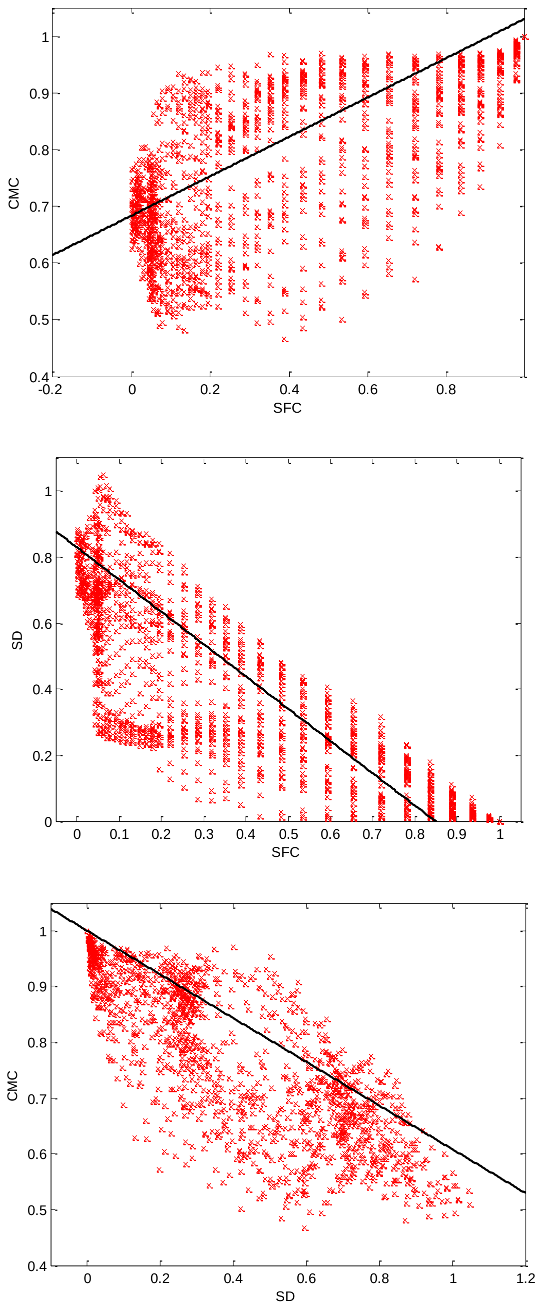

Figure 6.18: Scatter plots of CMC (top) and WSD (middle) as a function of SFC and CMC (bottom) as function of WSD

in a range of 5 to 23 m for different measured areas from two BS sites (BS1a and BS2).

Based on the measurement campaign II, the multi-user separation has been characterized for MU-MIMO links in urban microcellular networks by means of three metrics (SFC, CMC and WSD). Experimental results have been extracted to quantify the separation in the sense of MU-MIMO. SFC-based multi-user separation has been experimentally characterized as a function of distances as well as angles. The global values of multi-user separation were found approximately 10 to 12 m and 2 to 6 degree for distance and angular characterization respectively. CMC-based multi-user separation analysis has revealed approximate separation distance of 11 m with respect to 8-element planner array at BS. It is worth mentioning that CMC-based multi-user separation results were found consistent with SFC-based results. Lastly with the WSD metric, multi-user separation distances have been found in a range of 12 to 16 m, again close to results of earlier two metrics.

Novel models have been proposed to match empirical results for each metric separately. Moreover, heuristic explanation of each metric has been provided. While accounting results from three evaluated metrics together, the empirical evidence have shown that multiple users should physically be separated by an approximate distance of 8 to 12 meters or an angle of 2 to 6 degrees in order to reduce the multi-user interference to an acceptable level. This conclusion is roughly irrespective of the investigated metric (or, equivalently, the related signal processing aspect). In a multi-user environment, such quantified separation distances or angles would allow users coordination to minimize the potential interference, thus increasing the achievable capacity density in wireless networks.

CHAPTER 7

Conclusion

The wireless communication networks have been constantly evolving to meet the users' growing demands in term of capacity, throughput and coverage. While LTE-Advanced (4G) is being developed by 3GPP which aims to meet IMT-Advanced requirement, research for beyond 4G networks has already started to provide ubiquitous connectivity with sufficient bandwidth, robustness and latency. Several solutions have been proposed to provide ultra high capacity density, unprecedented throughput and extended coverage. Among these, a promising solution of the multi-beam BS antenna providing high capacity links to distributed RSs (which then serve multiple users) deployed in dense urban environment has been proposed by the BuNGee project to improve the overall network capacity density. Such relay-assisted architecture essentially involves multi-link propagation in various wireless links. Since the performance of all wireless networks is heavily dependent on the behaviour of underlying propagation channels, various multi-link propagation channel parameters have been characterized in this thesis. Channel parameters and models could be integrated in system-level simulations to provide the reliable estimation of the network performance.

With that perspective, two channel modeling approaches have been considered in this thesis to characterize and model wireless propagation channels in urban microcellular networks. First, an enhanced RT simulation tool has been utilized to characterize wireless channels in densely deployed environment (i.e., a square-cell topology). In particular, impact of the multi-beam BS antenna on channel characteristics and multi-link interference has been characterized. Second, extensive measurement campaigns with MIMO channel sounder have been carried out in a microcellular urban environment (with three BS sites and three geographical areas). Main contributions of this thesis can be summarized as follows:

Multi-Beam Base Station Architecture: Channel Models and Array Optimization

To reflect peculiarities of the innovative multi-beam BS antenna architecture, a number of channel parameters have been investigated and modeled. Subsequently, RT-based results have been compared with existing channel models to suggest that they require significant modifications, in particular with regard to transmit and receive antenna specifications considered in the novel architecture.

- Impact of narrow beams (i.e., a specificity of the multi-beam BS antenna) on pathloss model for the backhaul link has been characterized. It has been established that pathloss increases due to narrow-bandwidth of antennas. In this context, an RT-based GRF model has been derived to adequately compare pathloss results of the WINNER II channel model and RT simulations. In addition, several polarization-based MIMO channel characteristics have been investigated. Results have illustrated discrepancies mainly due to narrow-beamwidth antennas and dense deployment scenarios. Nevertheless, RT-based results have been shown in agreement with existing models (e.g., WINNER II and IEEE 802.16), when peculiarities of the innovative architecture are taken into account.

- The array optimization technique has been exploited to characterize and suppress not only CCI owing to excessive spectral reuse but also ICI due to same frequency beams from the neighbouring cell. RT-based results have shown a significant SIR improvement of 5 to 8 dB with optimized arrays. Importantly, this improvement has been achieved without any increase in pathloss as peak gains of optimized arrays remain almost identical. The array optimization technique has been shown as a promising solution to effectively suppress the CCI encountered by multi-beam antennas, thus guaranteed better performance in wireless networks.

- The performance of interference bound wireless links in high capacity wireless networks has been evaluated. By using optimized arrays, system level simulations have demonstrated a considerable less interruption in wireless links as well as a significant improvement in the throughput density. These observations have confirmed the influence of optimized arrays to the performance of wireless networks.

Relay Architecture Designs

The relay architecture has been considered in the BuNGee project to enhance the capacity and coverage of the wireless network. In order to design efficient relay-assisted wireless networks, relay-associated parameters have to be chosen carefully. For this purpose, two critical parameters have been characterized for backhaul links in a densely deployed urban environment.

- Impact of the RS antenna orientation on pathloss has been investigated to find the optimal position. A clear dependence of pathloss on the antenna orientation has been shown through RT simulations. To allow maximum antenna contributions at the RS, it has been suggested to direct the RS antenna in the largest power ray direction, although it is quite complicated from a practical deployment perspective.

- Impact of the relay antenna height on pathloss has been characterized. The numerical analysis has shown improvement in pathloss with increase in the RS antenna height. This improvement has been found less evident for RS locations under NLOS conditions. Nevertheless, increasing the relay height beyond a certain limit would carry additional interference from adjacent cells. Therefore, a trade-off between achievable pathloss and level of interference from adjacent cell has been proposed such that the RS is enabled with high SINR.

Multi-User Channel Models

In classical wireless networks, a stationarity assumption has been often used saying that the statistics of wireless propagation channels do not change over time. Most of the signal processing algorithms have been designed under this assumption. However, such assumption may not hold valid for time-varying (non-stationary) environments, thus requiring characterization of valid stationarity distances. With that perspective, experimental measurement campaigns were conducted with a mobile unit in a typical urban microcellular environment to probe the non-stationarity behaviour of MIMO wireless propagation channels. Using an appropriate threshold value, stationarity regions have been identified over which the WSS assumption locally hold. Typical estimated statioarity distances have been found in a range of 5 to 23 m depending upon the environment under investigation.

In practical MU-MIMO channels, users can only be considered separated when the wireless propagation channel's characteristics permit. If user channels are not spatially separated sufficiently, it results in multi-user interference which in turn degrades the performance. Therefore, multi-user separation has been experimentally characterized for MU-MIMO links in urban microcellular networks by means of three metrics (each with distinct signal processing aspect in mind). The empirical evidence have shown that multiple users should physically be separated by an approximate distance of 8 to 12 meters or an angle of 2 to 6 degrees in order to reduce the multi-user interference. Furthermore, multi-user separation results have been shown roughly irrespective of the investigated metric (or, equivalently, the related signal processing aspect). For each evaluated metric, empirical multi-user separation models have been proposed. These crucial findings of spatially separated channels influence the future space-time algorithms, e.g., when multi-users have spatially separable channels, they can be scheduled jointly to increase the overall network capacity.

Perspective and Future Work

Considering fast progress in the development of next generation wireless networks and achieved results in this thesis, several possibilities for the future work can be suggested.

The pathloss increase and other discrepancies in various channel modeling parameters observed for the fixed relay link due to narrow-beamwidth could be validated through a measurement campaign dedicated for highly directional antennas deployed at both sides of the link. Moreover, interference is an open issue at multiple levels in hierarchical wireless networks. More work could be performed to characterize and reduce potential interference in multi-link scenarios.

At the relay side, the pathloss reduction observed by increasing the antenna height may bring interference from neighbouring cells. A measurement campaign dedicated to characterize the angular spectrum at the RS can be conducted. It could be interesting to show improvement in the SINR at the RS with the help of a directional antenna deployed in a dense urban environment.

While research paradigms have recently shifted from single link to multi-links with emergence of distributed MIMO, MU-MIMO and co-operative communication networks, existing channel models are mostly not fully compatible as originally they have been developed for single-link systems. The necessary extension of reliable channel models from single-link to multi-link is not trivial in order to develop multi-user communication techniques. In this regard, multi-link channel modeling work could be enhanced on multiple levels such as estimating and modeling joint statistics of channel parameters (specially focusing on small scale statistics) and validating through measurements in multi-link scenarios (i.e., multi-cell and multi-user communication).

Publications

Journals:

- N. Khan, T. Jiang, D. Grace, A.G. Burr, and C. Oestges, "Performance Evaluation of Interference Bound High Capacity Self-Backhaul Links in Wireless Networks," *Wireless Personal Communications:* Volume 74, Issue 4 (2014), Page 1129-1145.
- N. Khan, C. Oestges, "Experimental Evaluation of Multi-User Separation in Urban Microcellular Networks," *under review in IEEE Transactions on Vehicular Technology*, 2014.

Conference proceedings:

- N. Khan, C. Oestges, "Impact of Transmit Antenna Beamwidth for Fixed Relay Links Using Ray-Tracing and Winner II Channel Models," *5th European Conference on Antennas and Propagation, EuCAP11*, Rome Italy, April 2011.
- O. Marinchenco, N. Chayat, M. Goldhamer, A. Burr, A. Papadogiannis, M. Dohler, M. Payaro, C. Oestges, N. Khan, M. Ware, "BuNGee project overview," *Microwaves, Communications, Antennas and Electronics Systems (COMCAS), 2011 IEEE International Conference on* , vol., no., pp.1-9, 7-9 Nov. 2011.
- N. Khan, C. Oestges, "Small Scale Statistics of Fixed Relay Polarimetric Links Using Narrow Beamwidth Antennas at 3.5 GHz," *15th Symposium on Wireless Personal Multimedia Communications, WPMC12*, Taipei, Taiwan.
- N. Khan, T. Jiang, D. Grace, A. G. Burr, and C. Oestges, "Impact of Multi-beam Antenna Amplitude Tapering on Co-Channel Interference and Backhaul Throughput Density," *15th Symposium on Wireless Personal Multimedia Communications, WPMC12*, Taipei, Taiwan.
- C. Oestges, N. Khan, F. Mani, and R. P. Cerdeira, "A Geometry-Based Physical-Statistical Model of Land Mobile Satellite Channels in Urban Environments", accepted in *8th European Conference on Antennas and Propagation, EuCAP'14*, The Hague Netherlands, April 2014.

COST TDs:

- N. Khan, C. Oestges, "Small Scale Statistics of Fixed Relay Polarimetric Links at 3.5 GHz," *COST IC1004 TD (11) 02025*, Lisbon Portugal, October 2011.
- N. Khan, T. Jiang, D. Grace, A. G. Burr, and C. Oestges, "Impact of Multi-beam Antenna Amplitude Tapering on Co-Channel Interference and Backhaul Throughput Density," *COST IC1004 TD (12) 04019*, Lyon France, May 2012.
- N. Khan, C. Oestges, "Experimental Characterization of Inter-User Distance in Urban Micro-cellular Networks", *COST IC1004 TD (13) 08058*, Gent Belgium, 25-27 September 2013.

Bibliography

[1] J. Korhonen, *Introduction to 3G Mobile Communication.* Artech House Publishers, 2003.

[2] E. Dahlman, S. Parkvall, and J. Skold, *4G LTE/LTE-Advanced for Mobile Broadband.* Oxford, UK: Academic Press Elsevier, 2011.

[3] F. Khan, *LTE for 4G Mobile Broadband Air Interface Technologies and Performance.* New York, US: Cambridge University Press, 2009.

[4] 3rd Generation Partnership Project. [Online] Available: http://www/3gpp.org.

[5] White Paper, *2020: Beyond 4G Radio Evolution for the Gigabit Experience.* ESPOO, Finland: Nokia Siemens Networks, 2013.

[6] B. Clerckx and C. Oestges, "MIMO wireless networks: channels, techniques and standards for multi-antenna, multi-user and multi-cell systems," *Academic Press: Oxford*, Jan. 2013.

[7] O. Marinchenco, N. Chayat, M. Goldhamer, A. Burr, A. Papadogiannis, M. Dohler, M. Payaro, C. Oestges, N. Khan, and M. Ware, "BuNGee project overview," *IEEE International Conference on Microwaves, Communications, Antennas and Electronics Systems (COMCAS)*, Nov. 2011.

[8] F. Mani, "Improved ray-tracing for advanced radio propagation channel modeling," *PhD Thesis, ICTEAM, UCL Belgium*, June 2012.

[9] N. Khan and C. Oestges, "Impact of transmit antenna beamwidth for fixed relay links using ray-tracing and WINNER II channel models," in *Proceedings of the 5th European Conference on Antennas and Propagation (EuCAP '11)*, (Rome, Italy), pp. 2938 –2941, April 2011.

[10] N. Khan and C. Oestges, "Small scale statistics of fixed relay polarimetric links using narrow-beamwidth antennas at 3.5 GHz," in *The 15th Wireless Personal Multimedia Communications Symposium (WPMC'12)*, (Taipei, Taiwan), Sep. 2012.

[11] N. Khan, T. Jiang, D. Grace, A. G. Burr, and C. Oestges, "Impact of multi-beam antenna amplitude tapering on co-channel interference and backhaul throughput density," in *The 15th Wireless Personal Multimedia Communications Symposium (WPMC'12)*, (Taipei, Taiwan), September 2012.

[12] N. Khan, T. Jiang, D. Grace, A. G. Burr, and C. Oestges, "Performance evaluation of interference bound high capacity self-backhaul links in wireless networks," *Wireless Personal Communications*, vol. 74, pp. 1129–1145, Jan. 2014.

[13] N. Khan and C. Oestges, "Experimental evaluation of multi-user separation in urban microcellular networks," *IEEE Transactions on Vehicular Technology*, 2014.

[14] B. Clerckx and C. Oestges, *MIMO wireless communications: from real-world propagation to space-time code design.* Elsevier: Academic Press, 2007.

[15] A. F. Molisch, "Wireless communications," *IEEE Press*, 2005.

[16] J. D. Parsons, "The mobile radio propagation channel," *2nd ed. John Wiley and Sons*, 2001.

[17] J. Andersen, T. Rappaport, and S. Yoshida, "Propagation measurements and models for wireless communications channels," *IEEE Communications Magazine*, vol. 33, no. 1, pp. 42–49, 1995.

[18] T. S. Rappaport, "Wireless communications: Principles and practice," *2nd ed. Prentice Hall PTR*, 2002.

[19] H. Suzuki, "A statistical model for urban radio propogation," *IEEE Transactions on Communications*, vol. 25, no. 7, pp. 673–680, 1977.

[20] A. Molisch, M. Steinbauer, M. Toeltsch, E. Bonek, and R. Thoma, "Capacity of MIMO systems based on measured wireless channels," *IEEE Journal on Selected Areas in Communications*, vol. 20, no. 3, pp. 561–569, 2002.

[21] S. Alamouti, "A simple transmit diversity technique for wireless communications," *IEEE Journal on Selected Areas in Communications*, vol. 16, no. 8, pp. 1451–1458, 1998.

[22] V. Tarokh, N. Seshadri, and A. Calderbank, "Space-time codes for high data rate wireless communication: performance criterion and code construction," *IEEE Transactions on Information Theory*, vol. 44, no. 2, pp. 744–765, 1998.

[23] D. Love and R. Heath, "Equal gain transmission in multiple-input multiple-output wireless systems," *IEEE Transactions on Communications*, vol. 51, no. 7, pp. 1102–1110, 2003.

[24] L. M. Correia, "Mobile broadband multimedia networds: techniques, models and tools for 4G," *Academic Press, Elsevier*, 2006.

[25] F. P. Fontan and P. M. Espineira, "Modeling the wireless propagation channel: a simulation approach with MATLAB," *Wiley*, 2008.

[26] J. Kermoal, L. Schumacher, K. Pedersen, P. Mogensen, and F. Frederiksen, "A stochastic MIMO radio channel model with experimental validation," *IEEE Journal on Selected Areas in Communications*, vol. 20, no. 6, pp. 1211–1226, 2002.

[27] W. Weichselberger, M. Herdin, H. Ozcelik, and E. Bonek, "A stochastic MIMO channel model with joint correlation of both link ends," *IEEE Transactions on Wireless Communications*, vol. 5, no. 1, pp. 90–100, 2006.

[28] S. R. Saunders and A. A. Zavala, "Antennas and propagation for wireless communication systems," *John Wiley and Sons*, 2007.

[29] C. Oestges, "Multi-link propagation modeling for beyond next generation wireless," in *Antennas and Propagation Conference (LAPC), Loughborough*, pp. 1–8, 2011.

[30] M. Gudmundson, "Correlation model for shadow fading in mobile radio systems," *Electronics Letters*, vol. 27, no. 23, pp. 2145–2146, 1991.

[31] F. Graziosi and F. Santucci, "A general correlation model for shadow fading in mobile radio systems," *IEEE Communications Letters*, vol. 6, no. 3, pp. 102–104, 2002.

[32] F. Graziosi, M. Pratesi, M. Ruggieri, and F. Santucci, "Modeling of handover initiation algorithms with correlated co-channel

interferers," in *IEEE 6th International Conference on Universal Personal Communications Record*, pp. 244–248 vol.1, 1997.

[33] M. Pratesi, M. Ruggieri, F. Graziosi, and F. Santucci, "Performance of signal strength handover algorithms with interference and correlated shadowings," in *IEEE 47th Vehicular Technology Conference*, vol. 2, pp. 530–534, 1997.

[34] D. Avidor, N. Hegde, and S. Mukherjee, "On the impact of the soft handoff threshold and the maximum size of the active group on resource allocation and outage probability in the UMTS system," *IEEE Transactions on Wireless Communications*, vol. 3, no. 2, pp. 565–577, 2004.

[35] S. Mukherjee and D. Avidor, "Effect of microdiversity and correlated macrodiversity on outages in a cellular system," *IEEE Transactions on Wireless Communications*, vol. 2, no. 1, pp. 50–58, 2003.

[36] N. Gogate, D. Avidor, and S. Panwar, "Simulation study of a fixed wireless access system," in *IEEE 1998 International Conference on Universal Personal Communications, ICUPC'98*, vol. 1, pp. 209–215, 1998.

[37] M. Haleem, D. Avidor, and R. Valenzuela, "Fixed wireless access system with autonomous resource assignment," in *The Ninth IEEE International Symposium on Personal, Indoor and Mobile Radio Communications*, vol. 3, pp. 1438–1442, 1998.

[38] V. Graziano, "Propagation correlations at 900 MHz," *IEEE Transactions on Vehicular Technology*, vol. 27, no. 4, pp. 182–189, 1978.

[39] D. Kaltakis, M. Imran, and R. Hoshyar, "Uplink capacity with correlated lognormal shadow fading," in *IEEE 69th Vehicular Technology Conference, VTC Spring 2009*, pp. 1–5, 2009.

[40] N. Czink, B. Bandemer, C. Oestges, T. Zemen, and A. Paulraj, "Subspace modeling of multi-user MIMO channels," in *IEEE Vehicular Technology Conference (VTC Fall)*, pp. 1–5, 2011.

[41] N. Czink, B. Bandemer, G. Vazquez-Vilar, L. Jalloul, C. Oestges, and A. Paulraj, "Spatial separation of multi-user MIMO channels," in *IEEE 20th International Symposium on Personal, Indoor*

and Mobile Radio Communications, PIMRC '09, pp. 1059–1063, 2009.

[42] F. Kaltenberger, L. Bernado, and T. Zemen, "On the characterization of MU-MIMO channels," in *International ITG Workshop on Smart Antennas (WSA)*, (Berlin, Germany), Feb. 2009.

[43] R. Valenzuela, "A ray tracing approach to predicting indoor wireless transmission," in *43rd IEEE Vehicular Technology Conference*, pp. 214–218, 1993.

[44] C. Oestges, B. Clerckx, L. Raynaud, and D. Vanhoenacker-Janvier, "Deterministic channel modeling and performance simulation of microcellular wide-band communication systems," *IEEE Transactions on Vehicular Technology*, vol. 51, pp. 1422–1430, Nov 2002.

[45] S. Seidel and T. Rappaport, "Site-specific propagation prediction for wireless in-building personal communication system design," *IEEE Transactions on Vehicular Technology*, vol. 43, p. 879891, Nov 1994.

[46] V. Degli-Esposti, D. Guiducci, A. de'Marsi, P. Azzi, and F. Fuschini, "An advanced field prediction model including diffuse scattering," *IEEE Transactions on Antennas and Propagation*, vol. 52, no. 7, pp. 1717–1728, 2004.

[47] V. Erceg and et al., "Channel models for fixed wireless applications," *IEEE 802.16 Broadband Wireless Access Working Group*, July 2007.

[48] C.-X. Wang, X. Hong, X. Ge, X. Cheng, G. Zhang, and J. Thompson, "Cooperative MIMO channel models: A survey," *IEEE Communications Magazine*, vol. 48, no. 2, pp. 80–87, 2010.

[49] G. Calcev, D. Chizhik, B. Goransson, S. Howard, H. Huang, A. Kogiantis, A. Molisch, A. Moustakas, D. Reed, and H. Xu, "A wideband spatial channel model for system-wide simulations," *IEEE Transactions on Vehicular Technology*, vol. 56, no. 2, pp. 389–403, 2007.

[50] G. T. 25.996, "Spatial channel model for multiple input multiple output (MIMO) simulations," *IEEE Transactions on*

Vehicular Technology, vol. V6.1.0, pp. [Online]. Available: http://www.3gpp.org/ftp/Specs/html–info/25996.htm, Sep. 2003.

[51] D. Baum, J. Hansen, and J. Salo, "An interim channel model for beyond-3G systems: extending the 3GPP spatial channel model (SCM)," in *IEEE 61st Vehicular Technology Conference, VTC 2005-Spring*, vol. 5, pp. 3132–3136, 2005.

[52] P. Kyosti and et al., "WINNER II channel models," *European Commission, Deliverable IST-WINNER D1.1.2 ver 1.1*, Sep. 2007 (Online: http://projects.celticinitiative.org/winner+/WINNER2-Deliverables/).

[53] R. Verdone, "COST 2100 - pervasive mobile and ambient wireless communications," *Berlin, Germany: Springer*, 2011.

[54] L. Liu, C. Oestges, J. Poutanen, K. Haneda, P. Vainikainen, F. Quitin, F. Tufvesson, and P. Doncker, "The COST 2100 MIMO channel model," *IEEE Wireless Communications*, vol. 19, no. 6, pp. 92–99, 2012.

[55] L. M. Correia, "COST 259 wireless flexible personalized communications," *Wiley, London, UK*, 2001.

[56] L. M. Correia, "COST 273 towards mobile broadband multimedia networks," *Academic Press, London, UK*, 2006.

[57] N. Czink and C. Oestges, "The COST 273 MIMO channel model: Three kinds of clusters," in *IEEE 10th International Symposium on Spread Spectrum Techniques and Applications, ISSSTA '08.*, pp. 282–286, 2008.

[58] L. Liu, N. Czink, and C. Oestges, "implementing the COST 273 MIMO channel model," in *NEWCOM++ - ACoRN Joint Workshop, Barcelona, Spain*, March 2009.

[59] J. Poutanen, F. Tufvesson, K. Haneda, V. Kolmonen, and P. Vainikainen, "Multi-link MIMO channel modeling using geometry-based approach," *IEEE Transactions on Antennas and Propagation*, vol. 60, no. 2, pp. 587–596, 2012.

[60] K. Haneda, J. Poutanen, F. Tuvfesson, L. Liu, V. Kolmonen, P. Vainikainen, and C. Oestges, "Development of multi-link geometry-based stochastic channel models," in *Antennas and Propagation Conference (LAPC), Loughborough*, pp. 1–7, 2011.

[61] M. Lawton and J. McGeehan, "The application of a deterministic ray launching algorithm for the prediction of radio channel characteristics in small-cell environments," *IEEE Transactions on Vehicular Technology*, vol. 43, no. 4, pp. 955–969, 1994.

[62] B. E. Gschwendtner, G. Wlfle, B. Burk, and F. Landstorfer, "Ray tracing vs. ray launching in 3-D microcell modelling," in *1st European Personal and Mobile Communications (EPMCC)*, (Bologna, Italy), 1995.

[63] P. Beckmann and A. Spizzichino, "The scattering of electromagnetic waves from rough surfaces," *Artech House*, 1987.

[64] S. R. Saunders, "Antennas and propagation for wireless communication systems," *Wiley*, 1999.

[65] G. Athanasiadou, A. Nix, and J. McGeehan, "A microcellular ray-tracing propagation model and evaluation of its narrow-band and wide-band predictions," *IEEE Journal on Selected Areas in Communications*, vol. 18, no. 3, pp. 322–335, 2000.

[66] G. Athanasiadou and A. Nix, "Investigation into the sensitivity of the power predictions of a microcellular ray tracing propagation model," *IEEE Transactions on Vehicular Technology*, vol. 49, pp. 1140–1151, July 2000.

[67] M. Landmann, K. Sivasondhivat, J.-I. Takada, I. Ida, and R. Thoma, "Polarization behavior of discrete multipath and diffuse scattering in urban environments at 4.5 GHz," *EURASIP Journal on Wireless Communications and Networking*, no. 1, p. 057980, 2007.

[68] J. Salmi, J. Poutanen, K. Haneda, A. Richter, V.-M. Kolmonen, P. Vainikainen, and A. F. Molisch, "Incorporating diffuse scattering in geometry-based stochastic MIMO channel models," in *Proceedings of the Fourth European Conference on Antennas and Propagation (EuCAP'10)*, pp. 1 –5, Apr. 2010.

[69] V. Degli-Esposti, F. Fuschini, E. M. Vitucci, and G. Falciasecca, "Measurement and modelling of scattering from buildings," *IEEE Transactions on Antennas and Propagation*, vol. 55, pp. 143 –153, January 2007.

[70] F. Mani and C. Oestges, "Ray-tracing evaluation of diffuse scattering in an outdoor scenario," in *5th European Conference on Antennas and Propagation, EuCAP 11*, (Rome, Italy), April 2011.

[71] E. M. Vitucci and et al., "Analysis and modeling of the polarimetric properties of scattering from building walls," *IEEE Transactions on Antennas and Propagation*, June 2012.

[72] V. Degli-Esposti, F. Fuschini, E. Vitucci, and G. Falciasecca, "Speed-up techniques for ray tracing field prediction models," *IEEE Transactions on Antennas and Propagation*, vol. 57, pp. 1469 –1480, May 2009.

[73] A. Burr, "Evaluation of capacity of indoor wireless MIMO channel using ray tracing," in *International Zurich Seminar on Broadband Communications, Access, Transmission, Networking*, pp. 28–1–28–6, 2002.

[74] Y. L. C. De Jong and M. H. A. J. Herben, "A tree-scattering model for improved propagation prediction in urban microcells," *IEEE Transactions on Vehicular Technology*, vol. 53, no. 2, pp. 503–513, 2004.

[75] R. Fritzsche, J. Voigt, C. Jandura, and G. Fettweis, "Verifying ray tracing based CoMP-MIMO predictions with channel sounding measurements," in *International ITG Workshop on Smart Antennas (WSA)*, pp. 161–168, 2010.

[76] T. Fugen, J. Maurer, T. Kayser, and W. Wiesbeck, "Capability of 3-D ray tracing for defining parameter sets for the specification of future mobile communications systems," *IEEE Transactions on Antennas and Propagation*, vol. 54, no. 11, pp. 3125–3137, 2006.

[77] F. Fuschini, H. El-Sallabi, V. Degli-Esposti, L. Vuokko, D. Guiducci, and P. Vainikainen, "Analysis of multipath propagation in urban environment through multidimensional measurements and advanced ray tracing simulation," *IEEE Transactions on Antennas and Propagation*, vol. 56, no. 3, pp. 848–857, 2008.

[78] Y. Corre and Y. Lostanlen, "Three-dimensional urban EM wave propagation model for radio network planning and optimization over large areas," *IEEE Transactions on Vehicular Technology*, vol. 58, no. 7, pp. 3112–3123, 2009.

[79] G. Athanasiadou and A. Nix, "A novel 3-D indoor ray-tracing propagation model: the path generator and evaluation of narrow-band and wide-band predictions," *IEEE Transactions on Vehicular Technology*, vol. 49, no. 4, pp. 1152–1168, 2000.

[80] F. de Adana, O. Gutierrez Blanco, I. Diego, J. Perez Arriaga, and M. Catedra, "Propagation model based on ray tracing for the design of personal communication systems in indoor environments," *IEEE Transactions on Vehicular Technology*, vol. 49, no. 6, pp. 2105–2112, 2000.

[81] E. Haddad, N. Malhouroux, P. Pajusco, and M. Ney, "Optimization of 3D ray tracing for MIMO indoor channel," in *XXXth URSI General Assembly and Scientific Symposium*, pp. 1–4, 2011.

[82] M. Janson, J. Pontes, C. Sturm, and T. Zwick, "BER simulations of a UWB spatial multiplexing system using an extended ray-tracing approach," *IEEE Antennas and Wireless Propagation Letters*, vol. 9, pp. 1096–1098, 2010.

[83] A. Magleby, C. Furse, and Z. Yun, "3D ray-tracing for intra-vehicle environments," in *IEEE Antennas and Propagation Society International Symposium, APSURSI '09.*, pp. 1–4, 2009.

[84] C. Sturm and W. Wiesbeck, "Ray-tracing in a virtual drive for mobile communications," in *3rd European Conference on Antennas and Propagation, EuCAP 2009*, pp. 1937–1939, 2009.

[85] V. Degli-Esposti, V. Kolmonen, E. Vitucci, and P. Vainikainen, "Analysis and modeling on co- and cross-polarized urban radio propagation for dual-polarized MIMO wireless systems," *IEEE Transactions on Antennas and Propagation*, vol. 59, no. 11, pp. 4247–4256, 2011.

[86] C. Jandura and J. Voigt, "Analysis of measured and simulated delay and angular propagation channel parameters for MIMO network planning," in *IEEE Vehicular Technology Conference (VTC Fall)*, pp. 1–5, 2011.

[87] R. Thoma, D. Hampicke, A. Richter, G. Sommerkorn, A. Schneider, U. Trautwein, and W. Wirnitzer, "Identification of time-variant directional mobile radio channels," *IEEE Transactions on*

Instrumentation and Measurement, vol. 49, no. 2, pp. 357–364, 2000.

[88] V. Jungnickel, S. Jaeckel, L. Thiele, L. Jiang, U. Kruger, A. Brylka, and C. Von Helmolt, "Capacity measurements in a cooperative MIMO network," *IEEE Transactions on Vehicular Technology*, vol. 58, no. 5, pp. 2392–2405, 2009.

[89] R. Irmer, H. P. Mayer, A. Weber, V. Braun, M. Schmidt, M. Ohm, N. Ahr, A. Zoch, C. Jandura, P. Marsch, and G. Fettweis, "Multisite field trial for LTE and advanced concepts," *IEEE Communications Magazine*, vol. 47, no. 2, pp. 92–98, 2009.

[90] C. Oestges, P. Castiglione, and N. Czink, "Empirical modeling of nomadic peer-to-peer networks in office environment," in *IEEE 73rd Vehicular Technology Conference (VTC Spring)*, pp. 1–5, 2011.

[91] V. Kolmonen, P. Almers, J. Salmi, J. Koivunen, K. Haneda, A. Richter, F. Tufvesson, A. Molisch, and P. Vainikainen, "A dynamic dual-link wideband MIMO channel sounder for 5.3 GHz," *IEEE Transactions on Instrumentation and Measurement*, vol. 59, no. 4, pp. 873–883, 2010.

[92] Elektrobit, *Channel sounder user manual.* Technical report, 2006.

[93] D. Martin-Sacristan, J. F. Monserrat, J. Cabrejas-Peuelas, D. Calabuig, S. Garrigas, and N. Cardona, "On the way towards fourth-generation mobile: 3GPP LTE and LTE-advanced," *EURASIP Journal on Wireless Communication and Networking*, vol. 2009, p. 10, Sept. 2009.

[94] A. Papadogiannis and A. Burr, "Multi-beam assisted MIMO – a novel approach to fixed beamforming," in *Future Network Mobile Summit (FutureNetw), 2011*, pp. 1–8, June 2011.

[95] M. Goldhamer and et al., "Baseline BuNGee architecture," *FP7 BuNGee project D1.2*, Nov. 2010 (Online:.http://www.ict-bungee.eu/2012).

[96] A. Grau, J. Romeu, S. Blanch, L. Jofre, and F. De Flaviis, "Optimization of linear multielement antennas for selection combining by means of a butler matrix in different MIMO environ-

ments," *IEEE Transactions on Antennas and Propagation*, vol. 54, pp. 3251–3264, Nov. 2006.

[97] C. Antennas, "Beyond next generation mobile broadband: BuNGee," *Microwave Journal*, Jan. 2012 (Online: http://www.microwavejournal.com/articles/456-beyond-next-generation-mobile-broadband-bungee).

[98] C. Oestges, V. Erceg, and A. Paulraj, "A physical scattering model for MIMO macrocellular broadband wireless channels," *IEEE Journal on Selected Areas in Communications*, vol. 21, pp. 721–729, June 2003.

[99] P. Soma, D. Baum, V. Erceg, R. Krishnamoorthy, and A. Paulraj, "Analysis and modeling of multiple-input multiple-output (mimo) radio channel based on outdoor measurements conducted at 2.5 GHz for fixed BWA applications," in *IEEE International Conference on Communications, ICC*, vol. 1, pp. 272–276, 2002.

[100] J. Zhang, D. Dong, X. Nie, Y. Liang, C. Huang, G. Liu, and W. Dong, "Propagation characteristics of wideband relay channels in urban environment," in *Fourth International Conference on Communications and Networking, ChinaCOM, China*, pp. 1–6, Aug 2009.

[101] L. Greenstein, V. Erceg, Y. Yeh, and M. Clark, "A new path-gain/delay-spread propagation model for digital cellular channels," *IEEE Transactions on Vehicular Technology*, vol. 46, pp. 477–485, May 1997.

[102] T. Jiang and et al., "Simulation tool(s) and simulation results," *FP7 BuNGee project D4.1.2*, Jan. 2012 (available online: http://www.ict-bungee.eu/2012).

[103] Q. H. Chu, "A contribution to multi-link propagation channel modeling for 4G radio mobile relaying systems," *PhD Dissertation, Ecole Nationale Superieure des Telecommunications (Telecom ParisTech)*, Dec. 2011.

[104] F. Kaltenberger, D. Gesbert, R. Knopp, and M. Kountouris, "Correlation and capacity of measured multi-user MIMO channels," in *IEEE 19th International Symposium on Personal, Indoor and Mobile Radio Communications, PIMRC '08*, pp. 1–5, 2008.

[105] M. Rahman, E. De Carvalho, and R. Prasad, "Mitigation of MIMO co-channel interference using robust interference cancellation receiver," in *IEEE 66th Vehicular Technology Conference, VTC-2007 Fall*, pp. 531–535, 2007.

[106] S. Szyszkowicz, H. Yanikomeroglu, and J. Thompson, "On the feasibility of wireless shadowing correlation models," *IEEE Transactions on Vehicular Technology*, vol. 59, no. 9, pp. 4222–4236, 2010.

[107] Z. Li, R. Wang, and A. Molisch, "Shadowing in urban environments with microcellular or peer-to-peer links," in *6th European Conference on Antennas and Propagation (EUCAP'12)*, pp. 44–48, 2012.

[108] K. Zayana and B. Guisnet, "Measurements and modelisation of shadowing cross-correlations between two base-stations," in *IEEE 1998 International Conference on Universal Personal Communications, ICUPC'98*, vol. 1, pp. 101–105, 1998.

[109] J. Weitzen and T. Lowe, "Measurement of angular and distance correlation properties of log-normal shadowing at 1900 MHz and its application to design of PCS systems," *IEEE Transactions on Vehicular Technology*, vol. 51, no. 2, pp. 265–273, 2002.

[110] M. Herdin, N. Czink, H. Ozcelik, and E. Bonek, "Correlation matrix distance, a meaningful measure for evaluation of non-stationary MIMO channels," in *IEEE 61st Vehicular Technology Conference. VTC 2005-Spring*, vol. 1, pp. 136–140, 2005.

[111] O. Renaudin, V. Kolmonen, P. Vainikainen, and C. Oestges, "Non-stationary narrowband MIMO inter-vehicle channel characterization in the 5-GHz band," *IEEE Transactions on Vehicular Technology*, vol. 59, no. 4, pp. 2007–2015, 2010.

[112] T. T. Georgiou, "Distances between power spectral densities," *Tech. Rep. arXiv:math/0607026v2*, Jul. 2006.

[113] N. Czink, B. Bandemer, G. Vazquez-vilar, L. Jalloul, and A. Paulraj, "Can multi-user MIMO measurements be done using a single channel sounder?," Oct. 2008.

[114] W.-Y. Lee and Y.-S. Yeh, “On the estimation of the second-order statistics of log normal fading in mobile radio environment,” *IEEE Transactions on Communications*, vol. 22, no. 6, pp. 869–873, 1974.

[115] D. De la Vega, S. Lopez, J. Matias, U. Gil, I. Pena, M. Ma Velez, J. Ordiales, and P. Angueira, “Generalization of the Lee method for the analysis of the signal variability,” *IEEE Transactions on Vehicular Technology*, vol. 58, no. 2, pp. 506–516, 2009.

[116] M. Herdin and E. Bonek, “A MIMO correlation matrix based metric for characterizing non-stationarity,” in *Proceedings IST Mobile and Wireless Communications Summit*, (Lyon, France), Jun. 2004.

[117] L. Bernad, T. Zemen, E. Paier, G. Matz, J. Karedal, N. Czink, F. Tufvesson, M. Hagenauer, A. F. Molisch, and C. F. Mecklenbruker, “Non-WSSUS vehicular channel characterization in highway and urban scenarios at 5.2 GHz using the local scattering function,” in *Workshop on Smart Antennas (WSA)*, pp. 9–15, 2008.

[118] G. Matz, “Characterization and analysis of doubly dispersive MIMO channels,” in *Fortieth Asilomar Conference on Signals, Systems and Computers, ACSSC ’06*, pp. 946–950, 2006.

[119] M. Zhu, F. Tufvesson, and J. Medbo, “Correlation properties of large scale parameters from 2.66 GHz multi-site macro cell measurements,” in *IEEE 73rd Vehicular Technology Conference (VTC 2011 Spring)*, pp. 1–5, 2011.

[120] N. Jalden, P. Zetterberg, B. Ottersten, A. Hong, and R. Thoma, “Correlation properties of large scale fading based on indoor measurements,” in *IEEE Wireless Communications and Networking Conference, WCNC’07*, pp. 1894–1899, 2007.